Title
Roles Played by Heater Size, Contact Angle, Surrounding Vessel Size, and Surface Structure during Pool Boiling on Horizontal Surfaces

Author
She, Zhenyu

Publication Date
2021

Peer reviewed|Thesis/dissertation

UNIVERSITY OF CALIFORNIA

Los Angeles

Roles Played by Heater Size, Contact Angle, Surrounding Vessel Size, and Surface Structure during Pool Boiling on Horizontal Surfaces

A dissertation submitted in partial satisfaction
of the requirements for the degree
Doctor of Philosophy in Mechanical Engineering

by

Zhenyu She

2021

ABSTRACT OF THE DISSERTATION

Roles Played by Heater Size, Contact Angle, Surrounding Vessel Size, and Surface Structure during Pool Boiling on Horizontal Surfaces

by

Zhenyu She
Doctor of Philosophy in Mechanical Engineering
University of California, Los Angeles, 2021
Professor Vijay K. Dhir, Chair

Nucleate boiling is ubiquitous from daily lives to engineering applications, and the increasing demand for efficient heat transfer in the industry requires further understanding of it, especially on small scales where the knowledge on conventional scales may no longer apply. This study investigated the effects of heater size, contact angle, surrounding vessel size, and surface structure on nucleate boiling heat transfer occurring on horizontal flat surfaces where the heater size is comparable to the two-dimensional "most dangerous" Taylor wavelength, aiming to comprehend the parametric effects on nucleate boiling heat flux and critical heat flux (CHF) and revisit the hydrodynamic theory near critical condition.

Saturated water at one-atmosphere pressure was boiled on horizontal flat copper discs of diameters 1.0, 1.5, and 2.0 cm, respectively. The contact angle was varied from about 10 to 80° by controlling thermal oxidation of the discs, while the surrounding vessel size was changed by placing glass tubes of different inner diameters around the discs. The surface structure in the form of microgrooves

was fabricated by sanding the disc top surface. Boiling heat transfer data were obtained up to CHF. Boiling curves and CHFs measured under different experimental configurations were compared in terms of each parameter. Rohsenow's correlation was employed to assess the parametric effects on nucleate boiling heat flux quantitatively. Vapor removal patterns were photographed in nucleate boiling regime and near CHF. Vapor jet diameter and the dominant wavelength at water-steam interface were measured from the photographs for the well wetted discs and used to predict the corresponding CHF based on the hydrodynamic theory.

For well wetted surfaces, the boiling curve was insensitive to the heater size, but the CHF increased when the heater size was reduced from 2.0 to 1.0 cm. Improving the wettability delayed the onset of nucleate boiling and shifted the boiling curve to the right while enhancing the CHF substantially. Enlarging the liquid-holding vessel hardly affected the boiling curve at low heat fluxes but improved the CHF slightly. The structured surface featured higher nucleate boiling heat flux resulting from more active nucleation sites but showed no advantage in CHF over the plain surface of similar size and contact angle. In this study, the highest measured CHFs for plain and structured surfaces are close and both about 2.1 times Zuber's CHF prediction for infinite horizontal flat plates. They were obtained on well wetted 1.0-cm-diameter discs surrounded by large vessels.

The dissertation of Zhenyu She is approved.

Xiaochun Li

Chang-Jin Kim

Yongjie Hu

Vijay K. Dhir, Committee Chair

University of California, Los Angeles

2021

Wish an early end to the epidemic. May peace and love forever prevail.

TABLE OF CONTENTS

LIST OF FIGURES

LIST OF TABLES

ACKNOWLEDGMENTS

I would like to express my sincere gratitude to my advisor, Prof. Vijay K. Dhir, for his guidance, patience, encouragement, and support during my graduate study. His conscientious comments and insightful advice in our weekly discussions had made my continuous improvement. I also want to extend my gratitude to my committee members, Prof. Yongjie Hu, Prof. Chang-Jin Kim, and Prof. Xiaochun Li, for their valuable advice and thorough review of my dissertation.

I want to express my appreciation to Ning Yu for his help with machining and Dr. Shuaihang Pan for his help with surface characterization. I am thankful to all my labmates, Vasudevan Chandramouli, Jin Jen, Atindra Krishnan, Julia Reed, Luca Valdarno, and Kieran Wolk, who composed a lively and dedicated group. I will never forget the days we shared thoughts and made progress together. Special thanks go to Vasudevan and Julia for their constructive suggestions on my experimental study.

I am also grateful to all my friends nearby for their company and assistance that made my study enjoyable. A shout-out to my undergraduate dormmates, Di Huang, Haoqing Jing, Junxi Liao, and Tianshu Wan: we are always brothers no matter how far we are from each other or what we are doing. My heartfelt debts are owed to Di and my cousin, Yuyang Lu, for my absences from their weddings due to the COVID-19 flight cutoff.

Finally, I want to profoundly thank my girlfriend, Xuan Zhou, and our family for their unconditional love and support, without which I cannot accomplish my study favorably.

This dissertation is based on a part of the work I performed in the Boiling and Phase Change Heat Transfer Laboratory at the University of California, Los Angeles.

VITA

2016–2021	Graduate Student Researcher, Teaching Fellow University of California, Los Angeles
2018	M.S. in Mechanical Engineering University of California, Los Angeles
2015	B.E. in Energy, Power System and Automation Xi'an Jiaotong University

PUBLICATIONS

Z. She and V.K. Dhir. Pool boiling heat transfer on horizontal surfaces of different sizes and wettability. In preparation, 2022.

Z. She and V.K. Dhir. Parametric effects of heater size, contact angle, and surrounding vessel size on pool boiling critical heat flux from horizontal surfaces. *Journal of Electronic Packaging*, 143(4):041113, 2021.

S. Pan, J. Yuan, T. Zheng, Z. She, and X. Li. Interfacial thermal conductance of in situ aluminum-matrix nanocomposites. *Journal of Materials Science*, 56:13646–13658, 2021.

Z. She and V.K. Dhir. Interacting effects of heater size, container size, and wettability on pool boiling critical heat flux. *International Mechanical Engineering Congress and Exposition*, IMECE2019-13196, 2019.

Z. She, Z. Wei, B.A. Young, G. Falzone, N. Neithalath, G. Sant, and L. Pilon. Examining the effects of microencapsulated phase change materials on early-age temperature evolutions in realistic pavement geometries. *Cement and Concrete Composites*, 103:149–159, 2019.

Z. Wei, B. Wang, G. Falzone, E.C. La Plante, M.U. Okoronkwo, Z. She, T. Oey, M. Balonis, N. Neithalath, L. Pilon, and G. Sant. Clinkering-free cementation by fly ash carbonation. *Journal of CO_2 Utilization*, 23:117–127, 2018.

B.A. Young, G. Falzone, Z. She, A.M. Thiele, Z. Wei, N. Neithalath, G. Sant, and L. Pilon. Early-age temperature evolutions in concrete pavements containing microencapsulated phase change materials. *Construction and Building Materials*, 147:466–477, 2017.

NOMENCLATURE

A	surface area, cm^2 or m^2
A_o	lateral surface area of heating base, cm^2 or m^2
A_v	cross-sectional area of vapor jet, cm^2 or m^2
c_p	specific heat capacity, J/kg K
C_{sf}	correlating constant of Rohsenow's correlation
d	thickness of disc, mm or m
d_g	thickness of graphite adhesive, mm or m
d_i	interplanar distance, nm or m
d_t	distance between thermocouples T_1 and T_3, mm or m
D	diameter of disc, cm or m
D_c	mouth diameter of cavity, μm or m
D_T	inner diameter of vessel, cm or m
D_v	diameter of vapor jet, cm or m
f_s	fraction of surface area wetted by liquid
f_v	fraction of surface area occupied by vapor jet
g	gravitational acceleration, m/s^2
h	heat transfer coefficient, W/m^2 K or kW/m^2 K
h_{fg}	latent heat of vaporization, J/kg
I	current, A
k_c	thermal conductivity of 110 Cu, W/K m
k_f	thermal conductivity of ceramic fiber, W/K m
k_g	thermal conductivity of graphite adhesive, W/K m
K	dimensionless modified curvature
l	capillary length, cm or m
L_c	characteristic length, cm or m

N_a	number density of active nucleation sites, cm^{-2}
N_c	number density of cavities, cm^{-2}
N_j	number of vapor jets on surface
N_s	number density of all cavities, cm^{-2}
p	pressure, Pa, kPa, mmHg, or bar
Pr	Prandtl number
q	heat flux, W/m^2 or W/cm^2
q_h	heat input, W/m^2
$\dot{Q}$	heat generation rate of cartridge heaters, W
r	roughness factor
R	radius, m
R'	dimensionless radius
R_b	radius of bubble or bubble embryo, m
R_c	mouth radius of cavity, m
R_h	electrical resistance of cartridge heater, Ω
R_i	thermal insulance, m^2 K/W
ΔRa	arithmetic average roughness, μm or m
t_h	heating time of thermal oxidation, min
T	temperature, °C
T_1, T_2, and T_3	temperatures measured by thermocouples, °C
T_h	heating temperature of thermal oxidation, °C
T_o	outer surface temperature of heating base, °C
T_s	surface temperature, °C
T_{sat}	saturation temperature, °C
ΔT_s	surface superheat, °C
U	voltage, Volts
V	velocity, m/s

V'	dimensionless volume of vapor
z_b	height of bubble embryo, m

Greek symbols

δ	thickness of superheated liquid layer, m
θ	contact angle, °
Θ	incident angle, °
λ_c	critical Taylor wavelength, cm or m
λ_d	"most dangerous" Taylor wavelength, cm or m
λ_H	Helmholtz unstable wavelength, cm or m
λ_X	wavelength of X-ray, nm or m
μ	dynamic viscosity, kg/m s
ρ	density, kg/m^3
σ	surface tension, N/m
ϕ	inclination angle from horizontal, °
ϕ_r	roll-off angle, °
φ	cone angle of cavity or wedge angle of groove, °
ψ_m	mouth angle of cavity, °
ψ_{min}	minimum side angle of cavity, °

Subscripts

adv	refers to dynamic advancing contact angle
air	refers to air
app	refers to apparent contact angle
b	refers to bubble or bubble embryo
c	refers to 110 Cu
cal	refers to calculated value
crit	refers to critical condition
CB	refers to Cassie-Baxter state

CHF	refers to critical heat flux
g	refers to gas
int	refers to intrinsic contact angle
l	refers to liquid
$local$	refers to local value
lv	refers to liquid-vapor interface
rec	refers to dynamic receding contact angle
sl	refers to solid-liquid interface
sv	refers to solid-vapor interface
v	refers to vapor
W	refers to Wenzel state
Z	refers to Zuber's critical heat flux prediction

CHAPTER 1

Introduction

Owing to its efficient heat transfer resulting from a large latent heat of vaporization, pool boiling, generally nucleate boiling, is ubiquitous in daily lives as well as engineering applications, e.g., from simple cooking to complex heat transfer systems, such as but not limited to power plants, nuclear reactors, heat exchangers, systems of air conditioning, refrigeration, and electronic cooling, etc. More than eighty years of extensive studies by numerous researchers, it still remains an active field of research and even attracts more attention with the development of advanced electronic devices and miniatured energy systems as well as for addressing new challenges of safety management. The ongoing breakthroughs achieved in semiconductor fabrication, e.g., shrinking transistor dimensions [5, 6] and three-dimensional packaging [7], enhance electronic performance. However, at the same time, the associated high power densities of those small electronics create a great challenge to thermal management. For example, the power dissipation from a microprocessor chip has been predicted to exceed 800 W by 2026 from 270 W in 2015 [8]. Supposing the die to be 2 cm $\times$ 2 cm in size, the average heat flux would increase to 200 W/cm^2. Besides, local hot spots with heat fluxes several times the average, sometimes exceeding 1 kW/cm^2, are very common and can potentially degrade the chip performance [9,10]. In other small electronic devices like insulated-gate bipolar transistors used in hybrid electric vehicles, heat fluxes up to 500 W/cm^2 are expected in the next generation as the operating voltage, current, and frequency increase [11]. Furthermore, in high-energy applications

like nucleate reactors that normally operate below critical, abnormal situations like hot spots in the core and cladding where critical condition may be exceeded are inevitable and should be prevented [12]. Besides, extreme cases like the core meltdown accident in Fukushima Daiichi nuclear power plant also rely on nucleate boiling heat transfer process to efficiently cool down the core. Therefore, improving nucleate boiling heat transfer is also of great importance in such applications.

Numerous studies have been performed in applying and improving boiling for heat dissipation in various configurations [13–16], such as microchannel flow boiling, flash evaporation, two-phase jet impingement, and spray cooling to meet different expectations of electronic cooling [17–20]. However, some fundamentals, such as the characteristics of boiling on small surfaces, still lack understanding. Since the bubble dynamics and vapor removal pattern can be quite different from those on large scales, the pool boiling heat transfer on chip-scale surfaces is worth a systematic study for the scientific design of electronic cooling systems. The study will benefit more applications by revealing ways of enhancing nucleate boiling heat transfer.

1.1 Fundamentals

1.1.1 Boiling curve

Potential, typically in the form of excess temperature or pressure drop, is required to drive phase change from liquid to vapor, namely, vaporization. There are two different types of vaporization: boiling and evaporation. Unlike evaporation, a passive and slow vaporization process only occurring at predetermined liquid-vapor/gas interfaces, boiling is a rapid and violent type of vaporization and takes place within liquids or at solid-liquid interfaces by generating a large number of bubbles. In most heat transfer systems involving boiling, the driving

potential is excess temperature over the saturation temperature corresponding to the system pressure. Boiling is initiated when the liquid is heated up beyond its saturation temperature. As a result, bubbles form on the heater surface and/or in the adjacent superheated liquid layer, thus creating liquid-vapor interfaces at discrete sites on the surface [21]. At these sites, the liquid undergoes a vaporization process and becomes vapor, during which a large amount of heat is removed from the surface and stored as the latent heat of vaporization. Besides, the development and departure of these bubbles lead to rapid mixing of the liquid near the surface, which enhances the heat transfer. Thus, boiling is an efficient heat transfer mode with a high heat transfer rate. Pool boiling refers to boiling under natural convection, whereas in flow boiling, liquids are imposed by external means to flow over heater surfaces [21]. Thus, the only difference lies in the influence of flow motion. The buoyancy effect is significant in pool boiling where the liquid is quiescent with only a part near the surface driven by natural convection and mixing, while forced convection dominates in flow boiling. This study focuses on pool boiling.

Nukiyama [22] firstly identified different regimes of pool boiling by immersing power-controlled wires in saturated water. Immediately after that, Drew and Mueller [23] solidified a complete boiling curve by contributing additional data. Figure 1.1 shows a typical boiling curve of saturated water at normal earth gravity and one-atmosphere pressure. The boiling curve plots boiling heat flux q as a function of surface superheat ΔT_s on a logarithmic scale. Surface superheat ΔT_s is the excess of surface temperature T_s over saturation temperature T_{sat}, i.e.,

$$\Delta T_s = T_s - T_{sat}. \tag{1.1}$$

The liquid remains near its saturation temperature except that a portion adjacent to the heater surface is superheated and features a sharp temperature gradient to drive heat transfer. Therefore, the heat flux q and surface superheat T_s can be

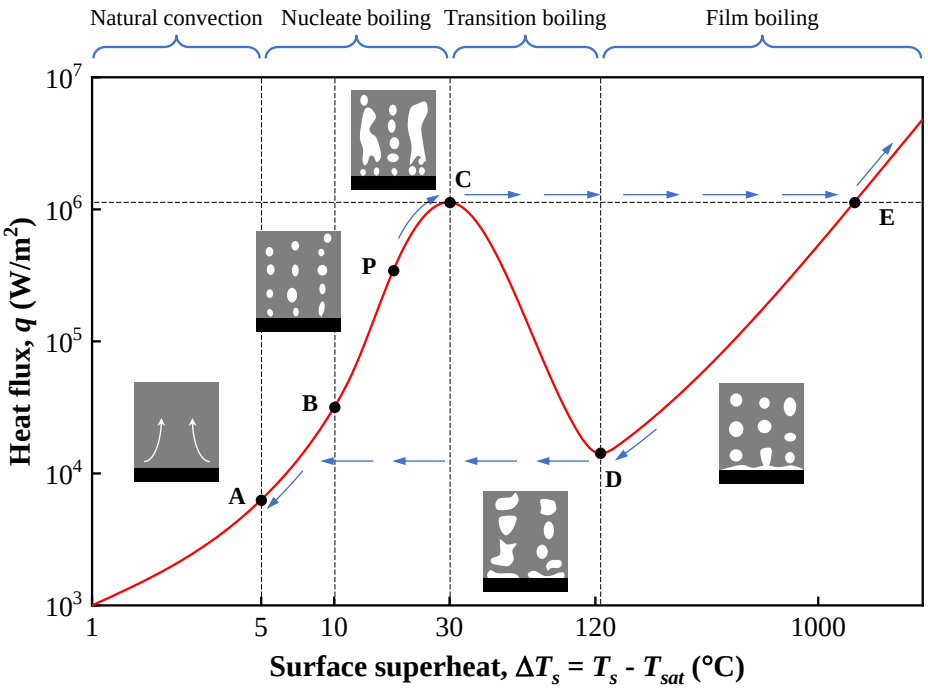

Figure 1.1: Typical boiling curve of saturated water at normal earth gravity and one-atmosphere pressure

correlated in the form of Newton's law of cooling as

$$q = h\Delta T_s, \tag{1.2}$$

where h is the heat transfer coefficient. Vapor removal patterns in different boiling regimes are also illustrated in Figure 1.1.

Natural convection

As shown in Figure 1.1, heat transfer occurs once the surface temperature exceeds the saturation temperature, i.e., $T_s > T_{sat} = 100°\text{C}$ or $\Delta T_s > 0°\text{C}$. When the surface superheat ΔT_s is relatively small, more specifically, less than about 5°C, no vaporization exists in this range as the heat transferred into the adjacent liquid layer is inadequate to drive bubble formation at nucleation sites. The heat transfer

within this regime can be described by natural convection.

Nucleate boiling

When the surface superheat ΔT_s exceeds 5°C, vaporization occurs, and bubbles start to form at discrete nucleation sites and depart from the surface, which denotes the onset of nucleate boiling (ONB), as marked by point **A** in Figure 1.1. Since only a few scattered nucleation sites exist, bubbles form, grow, and depart individually without interference. This range is the so-called isolated bubbles region. Aside from the large latent heat of vaporization, the movement of bubbles induces considerable mixing of the liquid near the surface, thus significantly increasing the heat flux q and heat transfer coefficient h.

The nucleate boiling becomes fully developed when the surface superheat ΔT_s is increased over 10°C, as marked by point **B** in Figure 1.1. More bubbles are produced with more nucleation sites activated, thus increasing the heat flux q and heat transfer coefficient h. At the same time, the bubbles easily interfere and coalesce with each other due to a high density, consequently causing the vapor to escape from the surface in the form of jets. These vapor jets subsequently break down and/or merge into slugs as getting farther away. With increasing surface superheat ΔT_s, the significant amount of generated vapor starts to inhibit the fluid motion near the surface. The heat flux q is still high but increases slower, as denoted by point **P** at the corresponding segment of the boiling curve in Figure 1.1.

The heat flux q reaches its local maximum of about 110 W/cm^2 when the surface superheat ΔT_s is further increased to about 30°C. This maximum heat flux of nucleate boiling is termed critical heat flux (CHF), as marked by point **C** in Figure 1.1. At CHF, a large amount of vapor is generated. The stability of the vapor jets or the ability of the liquid to rewet the surface determines the

maximum nucleate boiling heat flux [24].

In nucleate boiling regime, due to the violent vaporization and intense disturbance by bubbles, the heat flux q and heat transfer coefficient h increase much more sharply as the surface superheat ΔT_s is increased, compared to that in natural convection regime. Since high heat fluxes and heat transfer coefficients are associated with relatively low surface superheats in nucleate boiling regime, many engineering systems involving boiling are generally designed to operate within this regime [24, 25].

Transition boiling

With a further increase in the surface superheat ΔT_s from point **C**, the trend of the boiling curve changes extraordinarily, as shown in Figure 1.1. In this so-called transition boiling regime, a vapor film begins to develop and covers parts of the surface with bubbles produced rapidly and densely. This film impedes the removal of the generated vapor, resulting in a significant reduction in the local heat flux. At any position on the surface, the local condition is unstable and may oscillate between nucleate and film boilings [24]. Since more area becomes covered with the vapor film as the surface superheat ΔT_s is increased, the overall heat flux q decreases, and so does the heat transfer coefficient h. This trend lasts until the heat flux q reaches its local minimum, where the vapor film covers the surface completely, as marked by the Leidenfrost point **D** in Figure 1.1.

Film boiling

Starting from the Leidenfrost point, the boiling develops into the so-called film boiling. A stable vapor film persists on the surface, and the generated vapor is released from the film regularly. In this regime, heat transfer occurs by conduction

and radiation through the vapor film from the surface to the liquid, thus making film boiling much less efficient than nucleate boiling. With increasing surface superheat ΔT_s, radiation becomes more significant and dominant. As a result, the heat flux q and heat transfer coefficient h increase as the surface superheat ΔT_s is increased, as shown in Figure 1.1. It should be pointed out that the development of a boiling curve described above is obtained by increasing the surface temperature T_s. However, in many applications and experimental studies [26], the heat flux q rather than the surface temperature T_s is controlled. In such cases, as the heat flux q is increased by raising the supplied power, a boiling state initially in nucleate boiling regime jumps into film boiling regime directly without going through transition boiling regime when the CHF is exceeded, as the positive arrows in Figure 1.1 show. Similarly, by decreasing the heat flux q, a boiling state initially in film boiling regime develops following the boiling curve and jumps into nucleate boiling regime directly when the vapor film becomes unstable, as shown by the negative arrows in Figure 1.1. In engineering systems operating within nucleate boiling regime, once the applied heat flux q exceeds the CHF, the working condition will immediately worsen and jump into film boiling regime. The surface temperature T_s then soars and becomes extremely high, e.g., $T_s > 1000°\text{C}$ for water, as shown in Figure 1.1, subsequently causing surface burnout. Enhancing nucleate boiling heat transfer and CHF is of great significance in engineering applications, improving not only heat transfer efficiency but also safety and reliability, thus being stressed in the present study.

1.1.2 Nucleation

With increasing surface superheat, the heat transfer gradually develops into nucleate boiling regime from natural convection regime. The ONB is characterized by the appearance of bubbles at discrete locations on the surface. These bubbles form

on cavities in which the trapped gas serves as nuclei for bubble generation [21]. Not only does the trapped gas promote nucleation by providing pre-existing liquid-gas interfaces, but it also reduces the superheat required for nucleation. Based on the Clausius-Clapeyron relation, the liquid temperature T_l needed for a bubble of radius R_b to be in equilibrium within the liquid is given by

$$T_l - T_{sat} = \frac{2\sigma T_{sat}}{\rho_v h_{fg} R_b}, \tag{1.3}$$

where ρ_v, σ, and h_{fg} are the density of vapor, surface tension, and latent heat of vaporization at the saturation temperature T_{sat}, respectively. Dalton's law indicates that the pressure in the bubble nucleus p_b should be equal to the sum of the vapor pressure p_v and gas pressure p_g, i.e.,

$$p_b = p_v + p_g. \tag{1.4}$$

As the pressure difference across the liquid-vapor interface decreases by p_g, the required liquid temperature T_l decreases accordingly, i.e.,

$$T_l - T_{sat} = \left(\frac{2\sigma}{R_b} - p_g \right) \frac{T_{sat}}{\rho_v h_{fg}}. \tag{1.5}$$

Unflooded cavities

Not all cavities on the surface can trap gas for nucleation. Bankoff [27], in an early work, envisioned a criterion of gas entrapment in conical cavities, i.e.,

$$\varphi < \theta < 180^\circ - \varphi, \tag{1.6}$$

where φ is the cone angle of a cavity or the wedge angle of a groove, and θ is the contact angle of a liquid on the surface. With contact angle θ in this range, the liquid fills the upper portion of the corresponding cavity while trapping gas underneath. Thus, such cavities serve as potential nucleation sites and trigger bubble formation once being activated. Subsequently, Ward and Forest [28] analyzed the

relation between platelet adhesion and roughness of a synthetic biomaterial and showed that the gas trapped in a long narrow fissure would be in equilibrium if

$$\theta > 90^\circ + \varphi/2, \tag{1.7}$$

according to which wetted surfaces cannot trap gas in the conical cavities. Later, Wang and Dhir [29] developed another criterion of gas entrapment by minimizing the Helmholtz free energy of a system involving the liquid-gas interface in a cavity. Based on their criterion, a cavity will trap gas if

$$\theta > \psi_{\min}, \tag{1.8}$$

where ψ_{min} is the minimum cavity side angle of a spherical, conical, or sinusoidal cavity. For spherical and conical cavities, ψ_{min} is at the cavity mouth, whereas for a sinusoidal cavity, ψ_{min} is located where the cavity radius is half the cavity mouth radius. It is worth pointing out that for conical cavities, the criterion developed by Wang and Dhir is equivalent to that provided by Ward and Forest because of $\psi_{\min} = 90^\circ + \varphi/2$ in these cases.

All the criteria mentioned above, namely, Equations (1.6) to (1.8), indicate that hardly any cavities are unflooded on the surface when a well wetting liquid is placed. Thus, theoretically, when no potential nucleation site exists, the surface superheat should increase and approach that required for homogeneous nucleation. However, the observed inception superheats for well wetting liquids, though higher than those for partially wetting and dewetting liquids, are much smaller than those required for homogeneous nucleation [30]. It is hypothesized that gases dissolved in these liquids advance nucleation [21]. After inception, bubbles generated on activated cavities can momentarily displace the liquid from nearby flooded cavities, and some flooded cavities may dry out during the bubble growth period. As a result, these cavities are activated and serve as nucleation sites as long as the surface superheat is maintained. This activation improves the

heat transfer, thus reducing the surface superheat at a fixed heat flux. Graphically, the corresponding boiling curve shows hysteresis near the ONB.

Inception superheat

As for the inception superheat for boiling to occur on potential nucleation sites, Griffith and Wallis [31] proposed that it should correspond to the minimum radius of curvature of the liquid-vapor/gas interface, which was assumed to be equal to the cavity mouth radius R_c. Through the use of the Clausius-Clapeyron relation, they obtained an expression as

$$\Delta T_{s,GW} = T_s - T_{sat} = \frac{2\sigma T_{sat}}{\rho_v h_{fg} R_c}. \tag{1.9}$$

However, neither the contact angle effect nor the fact that a temperature gradient exists within the superheated liquid layer on the surface is considered in this equation.

Hsu [32] considered the effect of the temperature profile adjacent to the surface on the minimum surface superheat required for nucleation. Figure 1.2 (a) illustrates the postulated scene of a bubble embryo growing on an unflooded cavity in equilibrium within the superheated liquid layer of thickness δ on the surface. In Hsu's model, the bubble embryo will be in equilibrium if the temperature of the liquid at the bubble tip is equal to the saturation temperature corresponding to the pressure in the bubble. The temperature profile of the superheated liquid layer is assumed to be linear along the normal direction of the surface, i.e.,

$$T_l(z) - T_{sat} = (T_s - T_{sat})\left(1 - \frac{z}{\delta}\right) = \Delta T_s \left(1 - \frac{z}{\delta}\right), \tag{1.10}$$

as plotted in Figure 1.2 (b). The equation of a bubble in equilibrium, i.e., Equation (1.3), can be applied at the bubble tip and becomes

$$T_l(z_b) - T_{sat} = \frac{2\sigma T_{sat}}{\rho_v h_{fg} R_b}, \tag{1.11}$$

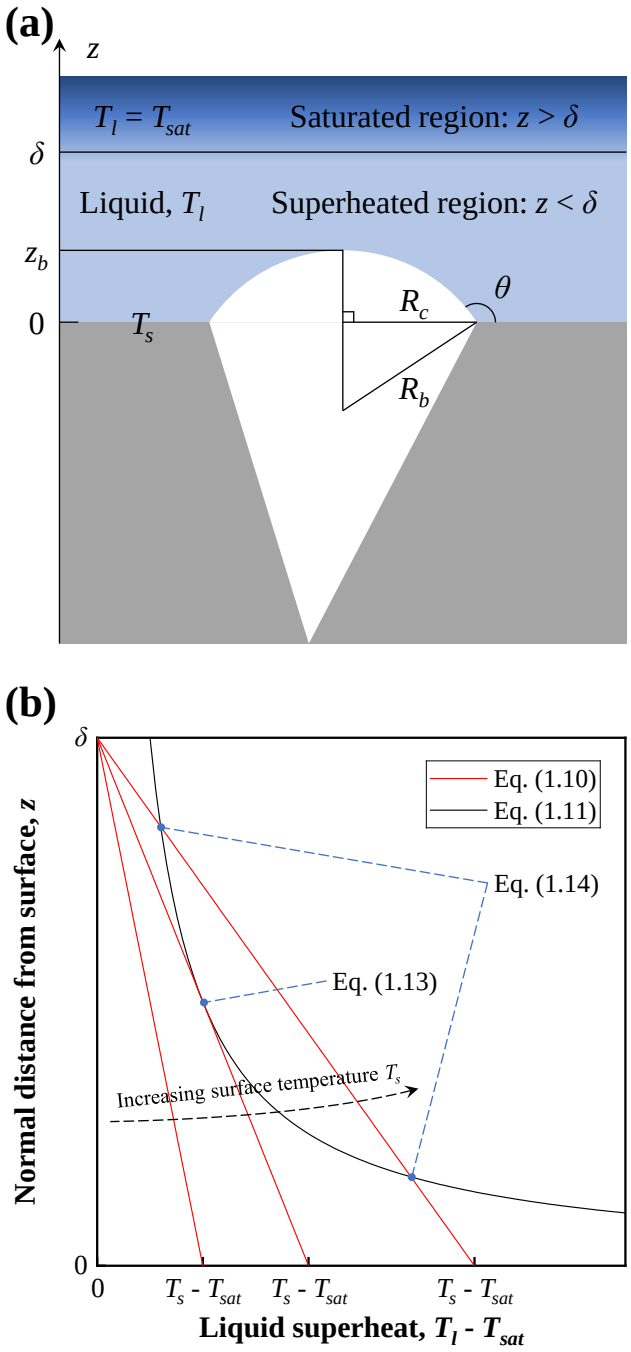

Figure 1.2: (a) Bubble embryo growing on an unflooded cavity in equilibrium within the superheated liquid layer on the surface. (b) Temperature profile of the superheated liquid layer along the normal direction of the surface.

where z_b and R_b are the height and radius of a bubble embryo growing on a cavity of mouth radius R_c, respectively. They are mathematically correlated as

$$z_b = R_b\,(1+\cos\theta) \text{ and } R_c = R_b \sin\theta. \tag{1.12}$$

Therefore, when Equation (1.10) is tangent to Equation (1.11), as shown in Figure 1.2 (b), the tangent point corresponds to the minimum surface superheat required for nucleation, i.e.,

$$\Delta T_{s,\min} = \frac{8\,(1+\cos\theta)\,\sigma T_{sat}}{\rho_v h_{fg} \delta}. \tag{1.13}$$

When the surface superheat exceeds it, more cavities will be activated. Then, solving Equations (1.10) to (1.12) gives the size range of activated cavities, i.e.,

$$\frac{\delta\sin\theta}{2(1+\cos\theta)}\left(1-\sqrt{1-\frac{8(1+\cos\theta)\sigma T_{sat}}{\rho_v h_{fg}\Delta T_s \delta}}\right) \le R_c \le \frac{\delta\sin\theta}{2(1+\cos\theta)}\left(1+\sqrt{1-\frac{8(1+\cos\theta)\sigma T_{sat}}{\rho_v h_{fg}\Delta T_s \delta}}\right), \tag{1.14}$$

as indicated by the intersections of Equations (1.10) and (1.11) in Figure 1.2 (b). For a cavity of mouth radius R_c to nucleate, the inception superheat is obtained as

$$\Delta T_{s,H} = \frac{2\sigma T_{sat}\sin\theta}{\rho_v h_{fg} R_c} \Bigg/ \left(1-\frac{(1+\cos\theta)\,R_c}{\delta\sin\theta}\right). \tag{1.15}$$

According to this equation, the size of an activated cavity varies inversely as surface superheat when $R_c \ll \delta$.

In addition to Hsu's criterion, Mizukami [33], Nishio [34], and more recently, Wang and Dhir [29] proposed that the instability of vapor nuclei in cavities determines the inception superheat. The vapor nucleus is stable if the curvature of the liquid-vapor interface increases with increasing vapor volume. If K is the dimensionless modified curvature of the interface, and V' is the dimensionless vapor volume, the stability criterion is expressed as

$$\frac{dK}{dV'} > 0. \tag{1.16}$$

The inception superheat is written as

$$\Delta T_{s,WD} = \frac{2\sigma T_{sat}}{\rho_v h_{fg} R_c} K_{\max}, \tag{1.17}$$

where the maximum value of K corresponds to the condition when the interface turns unstable. For geometric considerations, Wang and Dhir found

$$K_{\max} = \begin{cases} 1 & \theta \leq 90^\circ \\ \sin\theta & \theta > 90^\circ \end{cases} . \tag{1.18}$$

Equation (1.17) assumes that the cavity size is much smaller than the thermal layer thickness. As it suggests, the inception superheat is the same as that given by Griffith and Wallis, i.e., Equation (1.9), for wetted surfaces and decreases for dewetted surfaces. Wang and Dhir had validated Equation (1.18) through experiments on surfaces of different contact angles. Besides, it is worth pointing out that Equation (1.18) is in the absence of any gas trapped in cavities. K_{max} decreases with increasing mole fraction of gas, thus reducing the inception superheat for cavities to nucleate [29].

Nucleation sites

On a given surface, more cavities are activated to work as nucleation sites with increasing surface superheat, thus improving the heat transfer efficiency. In earlier studies summarized by Hsu and Graham [35], it was noted that the number density of active nucleation sites varies approximately as the square of heat flux or as surface superheat to a power of 4 to 6. However, at that time, no attempt was made to correlate either the proportionality constant or exponent with the surface characteristics.

Mikic and Rohsenow [36] proposed that on commercial surfaces, the number density of active nucleation sites N_a can be assumed to change in nucleate boiling regime following

$$N_a \sim \left(\frac{R_{c,\max}}{R_c}\right)^n, \tag{1.19}$$

where $R_{c,\max}$ is the mouth radius of the largest activated cavity present on the surface. The mouth radius R_c of the cavity that nucleates at surface superheat

ΔT_s is given by Equation (1.9). Later, Bier *et al.* [37] deduced another expression for the site density N_a as

$$\ln N_a = \ln N_{a,\max} \left[1 - \left(\frac{R_c}{R_{c,\max}} \right)^n \right], \tag{1.20}$$

where $N_{a,\max}$, the maximum value of the site density N_a, occurs at $R_c = 0$. The exponent n was found to depend on how a surface was prepared, and it was also noted that Equation (1.20) needs modification for correlating data within a wide pressure range. Cornwell and Brown [38] investigated the number density of active nucleation sites N_a on copper surfaces during boiling of water at one-atmosphere pressure. They focused on cases of low heat fluxes on smooth and rough surfaces and concluded that the site density N_a varies as surface superheat ΔT_s in the form of

$$N_a \sim {\Delta T_s}^{4.5}, \tag{1.21}$$

where the proportionality constant was found to increase with increasing surface roughness, but the exponent 4.5 was independent of surface roughness. This trend of site density against surface roughness is consistent with that proposed by Mikic and Rohsenow while opposite to that deduced by Bier *et al.*, and the exponent 4.5 falls within the range of 4 to 6 estimated by Hsu and Graham. The correlation between the number density of active nucleation sites and system pressure was further studied by Kocamustafaogullari and Ishii [39] who correlated the site densities reported by previous researchers for water boiled on different surfaces at pressures ranging from 1 to 198 bar.

To quantitatively predict the number density of active nucleation sites with the knowledge of the size and cone or mouth angle distribution of cavities that exist on the surface, Yang and Kim [40] and later Wang and Dhir [41] analyzed statistically following the Poisson distribution that was noted by Gaertner [42], Sultan and Judd [43], and Del Valle and Kenning [44]. Wang and Dhir studied the effect of surface wettability during boiling of water at one-atmosphere pressure on

mirror-finish copper surfaces and correlated the number density of cavities N_c (in cm^{-2}) with cavity mouth diameter D_c (in μm) as

$$N_c\left(D_c\right) = \begin{cases} 9.0 \times 10^3 {D_c}^{-2.0} & D_c \geq 5.8\mu\mathrm{m} \\ 10.3 + 2.4 \times 10^6 {D_c}^{-5.2} & 3.5\mu\mathrm{m} \leq D_c < 5.8\mu\mathrm{m} \\ 2213.5 + 1.0 \times 10^6 {D_c}^{-5.4} & D_c < 3.5\mu\mathrm{m} \end{cases} . \tag{1.22}$$

The number density of cavities of mouth angles less than ψ_m ($0° < \psi_m < 180°$) can be approximately written as

$$N_c\left(\psi_\mathrm{m}\right) = \frac{1 - \cos\psi_\mathrm{m}}{2} N_s, \tag{1.23}$$

where N_s is the number density of all cavities on the surface. Given the criterion that a cavity can nucleate when it satisfies Equations (1.8) and (1.17), the number density of active nucleation sites N_a can be regarded as a function of contact angle θ and surface superheat ΔT_s, i.e.,

$$N_a\left(\theta, \Delta T_s\right) = \frac{1 - \cos\theta}{2} N_c\left(D_c\right), \tag{1.24}$$

where D_c is a function of ΔT_s as described by Equation (1.17). Subsequently, Basu *et al.* [45] directly correlated the number density of active nucleation site N_a (in cm^{-2}) in nucleate boiling regime as

$$N_a\left(\theta, \Delta T_s\right) = \begin{cases} 0.34\left(1 - \cos\theta\right) {\Delta T_s}^2 & \Delta T_s < 15° \\ 3.4 \times 10^{-5}\left(1 - \cos\theta\right) {\Delta T_s}^{5.3} & \Delta T_s \geq 15° \end{cases} . \tag{1.25}$$

The exponent of ΔT_s 5.3 is equivalent to that of D_c - 5.2 or - 5.4 in Equation (1.22) considering that ΔT_s is inversely proportional to D_c as given by Equation (1.17).

To mathematically describe nucleate boiling process and predict the heat flux, additional parameters regarding bubble dynamics, such as bubble departure diameter and release frequency [46–50], are needed. Many related studies have been performed to investigate bubble growth and departure during boiling [51–54].

However, since experimental results in this study are mainly analyzed qualitatively, these parameters are not discussed.

1.1.3 Wetting

As mentioned in the above section, surface wettability plays an important role in nucleate boiling. A comprehensive understanding of it is necessary before carrying out this study.

Wetting is a common phenomenon occurring when a liquid-vapor interface contacts a solid surface. Wettability refers to the ability of a liquid to wet or spread on a surface and depends on force balance between the molecules. When the adhesive intermolecular force between the liquid and surface is greater than the cohesive intermolecular force within the liquid, the liquid behaves wetting. Otherwise, it is dewetting, e.g., droplets ball more on the surface.

Contact angle θ is defined as the angle through the liquid between the solid-liquid and liquid-vapor interfaces at a three-phase contact line, as illustrated in Figures 1.3 (a) and (b), which show the contact angles θ of a droplet and a liquid containing a rooted bubble on surfaces. The latter reflects the scene during boiling: bubbles generated on the heater surface create three-phase contact lines where contact angles manifest themselves. In practice, the contact angle θ is usually employed to represent the wettability of a liquid on a surface and offers an inverse measurement as it decreases with surface wettability improved.

Young's equation

For a droplet on an ideal surface that is perfectly smooth, rigid, and chemically homogeneous, in thermodynamical equilibrium, the contact angle θ is determined by the balance of interfacial tensions at the three-phase contact line and can be

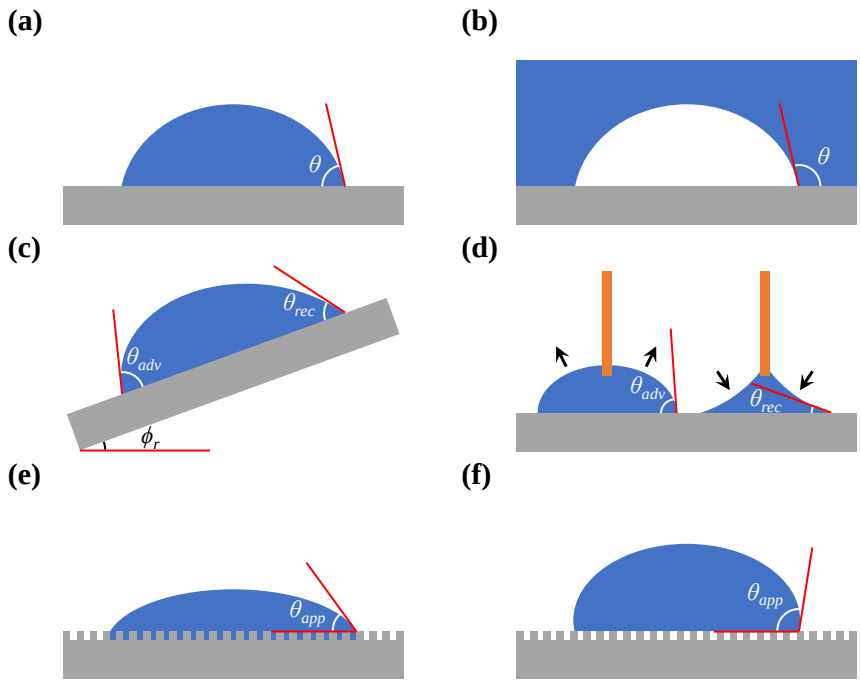

Figure 1.3: Schematics of the contact angles θ of (a) a droplet and (b) a liquid containing a rooted bubble on surfaces. Schematics of advancing contact angles θ_{adv} and receding contact angles θ_{rec} (c) on a tilted surface of roll-off angle ϕ_r and (b) by dispensing and drawing liquid using a fine needle. Schematics of apparent contact angles θ_{app} at (e) Wenzel and (f) Cassie-Baxter states on rough surfaces.

mathematically described by Young's equation [55]

$$\sigma_{sv} = \sigma_{sl} + \sigma_{lv} \cos\theta, \tag{1.26}$$

where σ_{sl}, σ_{sv}, and σ_{lv} (or σ) are the solid-liquid, solid-vapor, and liquid-vapor interfacial tensions, respectively. As can be seen from Equation (1.26), a liquid of smaller surface tension σ features a lower contact angle θ, namely, better wettability. Generally, a surface is called hydrophilic or wetted if it features a contact angle $\theta < 90°$ and is called hydrophobic or dewetted when $\theta \geq 90°$.

Hysteresis

However, on a practical surface, a droplet features a spectrum of contact angles θ [56]. The maximum and minimum values can be measured when the surface is tilted enough that the droplet is about to slide off [57], as illustrated in Figure 1.3 (c). The tilting angle at this moment is defined as the roll-off angle ϕ_r. The sliding front and tail of the droplet feature the so-called advancing contact angle θ_{adv} and receding contact angle θ_{rec}, respectively, which usually correspond to the maximum and minimum contact angles of a droplet on a practical surface. Figure 1.3 (d) illustrates another method. By placing a droplet on a surface using a fine-needle syringe, the advancing contact angle θ_{adv} can be measured when the needle incrementally dispenses liquid into the droplet, and the receding contact angle θ_{rec} can be measured when liquid is gradually drawn back to the syringe [58]. Regardless of the method of measurement, the difference between advancing and receding contact angles ($\theta_{adv} - \theta_{rec}$) is defined as contact angle hysteresis.

On rough surfaces

The contact angle θ of a droplet on an ideal surface can be regarded as an intrinsic contact angle θ_{int} as the apparent contact angle θ_{app} is affected by surface roughness. Unlike intrinsic contact angles θ_{int}, apparent contact angles θ_{app} cannot be calculated from Equation (1.26) directly. However, Equation (1.26) still applies at three-phase contact lines where intrinsic contact angles θ_{int} manifest. Depending on the degree of liquid penetration, wetting on rough surfaces can be categorized into two modes: Wenzel [59] and Cassie-Baxter [60] modes.

For wetting at Wenzel state, the droplet completely infiltrates into the surface structure, as illustrated in Figure 1.3 (e). In equilibrium, the apparent contact

angle θ_{app} is calculated by [59]

$$\cos\theta_{app,W} = r\cos\theta_{int}, \tag{1.27}$$

where r is the surface roughness factor that is defined as the ratio of actual surface area to projected surface area. Equation (1.27) informs that surface roughness amplifies the wetting and dewetting at Wenzel state by making wetted surfaces more wetted and dewetted surfaces more dewetted. When the droplet does not infiltrate at all, i.e., the surface structure is filled up with vapor/gas, as illustrated in Figure 1.3 (f), wetting is at Cassie-Baxter state. The apparent contact angle θ_{app} in equilibrium is calculated by [60]

$$\cos\theta_{app,CB} = f_s\cos\theta_{int} + f_s - 1, \tag{1.28}$$

where f_s is the fraction of surface area in contact with liquid. Equation (1.28) indicates that at Cassie-Baxter state, the apparent contact angle θ_{app} monotonically decreases with increasing fraction of surface area wetted by liquid f_s regardless of the intrinsic contact angle θ_{int}.

Either Wenzel or Cassie-Baxter state can be reached on a rough surface. The tendency depends on the critical contact angle given by [61]

$$\cos\theta_{crit} = \frac{1 - f_s}{r - f_s}. \tag{1.29}$$

Wenzel state is thermodynamically more favorable when the intrinsic contact angle θ_{int} is less than the critical contact angle θ_{crit}. Otherwise, Cassie-Baxter state is more favored. As an energy threshold exists between these two states, either is locally stable even with another more favorable as long as the threshold is not overcome [62]. Transitions between Wenzel and Cassie-Baxter states are usually caused by external factors. For example, a pressure exceeding the critical pressure of Cassie-Baxter state can result in a transition to Wenzel state [63], while a reverse transition needs other motivations, such as vibration, heating, or a current pulse

for detachment [64, 65]. In brief, work should be done to overcome the threshold for the transitions. In engineering applications and experimental studies involving boiling, heater surfaces are usually submerged in liquids for long times. Thus, Wenzel state is more common regardless of surface wettability and topography due to hydraulic pressure and the diffusion of trapped gas into boiled liquids [66].

1.2 Objectives of this study

The present study aims to experimentally investigate the roles played by heater size, contact angle, surrounding vessel size, and surface structure during nucleate boiling heat transfer occurring on horizontal flat surfaces of sizes comparable to vapor jet size. Boiling heat transfer data were obtained up to CHF. Boiling curves and CHFs measured under different experimental configurations were compared in terms of each parameter. Rohsenow's correlation was employed to assess the parametric effects on nucleate boiling heat flux quantitatively. Vapor removal patterns were photographed in nucleate boiling regime and near CHF. Vapor jet diameter and the dominant wavelength at water-steam interface were measured from the photographs for the well wetted surfaces and used to revisit the hydrodynamic theory.

1.3 Organization of this dissertation

This dissertation is composed of 7 chapters. The current chapter introduces the fundamentals of boiling and wetting and the objectives of the present study. Chapter 2 elaborates on the preparation of test surfaces and the design of experimental apparatus and procedure. Chapter 3 provides data reduction and uncertainty analysis. Chapters 4 and 5 present the boiling heat transfer data obtained on plain surfaces, compare them in terms of heater size, contact angle, and surround-

ing vessel size and discuss the parametric effects on nucleate boiling heat flux and CHF, respectively. Chapter 6 presents and compares the boiling heat transfer data obtained on plain and structured surfaces and discusses the surface structure effect on nucleate boiling heat flux and CHF. Chapter 7, finally, concludes the findings of this study.

CHAPTER 2

Experiments

This chapter presents the apparatus and procedure of experiments designed to measure boiling heat transfer data of saturated water for horizontal flat heaters. Each boiling experiment was configured based on its (i) heater size, (ii) contact angle, (iii) surface type (plain or structured), and (iv) surrounding vessel size. Prior to that, the methods of preparing plain and structured surfaces of different contact angles are elaborated.

2.1 Preparation of test surfaces

Copper discs (110 Cu) of thickness $d = 3$ mm and diameters $D = 1.0$, 1.5, and 2.0 cm were used as horizontal flat heaters in the boiling experiments. Wetting characteristic of the surface was identified through the use of static contact angle. Advancing or receding contact angle was not used. These dynamic angles change during the boiling process and depend on the liquid-vapor interface velocity which in turn would be affected by the surface superheat [67,68]. Before conducting any treatment on the disc, a polishing routine was performed to ensure the disc top surface was smooth without any bumps or scratches. For each disc, the top surface was first rubbed with a 1200-grit sanding cloth (400 MX, Micro-Mesh) in a certain direction 200 times and rubbed another 200 times after being rotated 90°. This step was then repeated using a 1500-grit sanding cloth (4000 AO, Micro-Mesh). The final polishing was performed using a 3000-grit sanding cloth (12000 AO,

Figure 2.1: Uniform mirror finish reached on the disc top surface after being processed following the polishing routine

Micro-Mesh) until a uniform mirror finish was reached, as shown in Figure 2.1. Finally, the prepared surface was cleaned with a disposable ethyl alcohol cotton swab and dried spontaneously in air. With all the steps above completed, the disc was ready for subsequent use.

2.1.1 Plain surfaces

Surface wettability

The method of changing copper surface wettability by thermal oxidation in air has been proposed and established for ages [69–72]. Regardless of the details, the basic ideas were the same in the references, i.e., changing heating temperature and heating time to vary the composition and thickness of the oxide layer forming

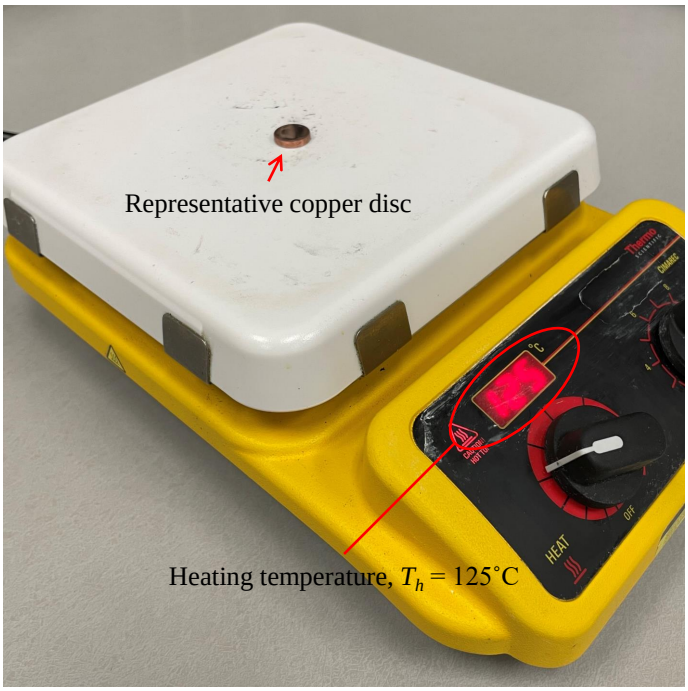

Figure 2.2: Representative copper disc being heated by the digital hotplate in air at 125°C

on a copper surface. In this study, to get different contact angles of the copper disc without altering its surface topography, the disc was oxidized in air following a predeveloped method [69, 71].

For this purpose, an experiment was performed on a representative copper disc of thickness $d = 3$ mm and diameter $D = 1.5$ cm to determine the dependence of contact angle on oxidation parameters, namely, heating temperature T_h and heating time t_h. In this experiment, after being processed following the polishing routine, the disc was placed on a digital hotplate (SP131635Q, Thermo Scientific) to be heated in air at temperature T_h, as shown in Figure 2.2. The heating temperature T_h was precisely controlled by rotating the knob of the hotplate and was directly displayed on its digital screen. In Figure 2.2, the representative disc was being heated by the hotplate in air at 125°C. After heating time t_h, the power

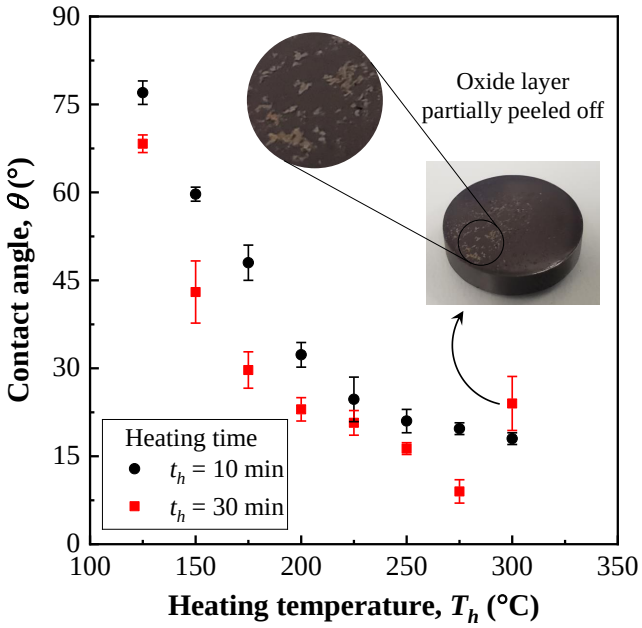

Figure 2.3: Contact angle θ as a function of heating temperature T_h and heating time t_h for the representative copper disc

was turned off. The disc subsequently cooled down along with the hotplate to room temperature. Thereafter, a local contact angle was measured from a photograph of a 0.01 mL deionized water droplet placed on the disc top surface. This measurement was repeated three times by placing droplets at different locations on the surface, and the average of these three values was used to represent the contact angle θ of the disc.

All the oxidized discs used in the boiling experiments were prepared following the same polishing routine and oxidation procedure except that the heating temperature T_h and heating time t_h were varied to obtain different contact angles θ. The unoxidized disc was processed following the polishing routine as well, only with no oxidation. Its contact angle θ was measured to be 90°. Figure 2.3 shows the contact angle θ as a function of heating temperature T_h and heating time t_h

for the representative disc. It illustrates that the contact angle θ can be continuously decreased by heating the disc in air at a higher temperature and/or for a longer time. Contact angles ranging from 77 to 9° were obtained following this method. The smallest contact angle 9° was obtained on the disc when it had been heated at 275°C for 30 min. When the disc had been heated to 300°C for 30 min, the oxide layer forming on its top surface was found to be unstable and peeled off during its cooldown period, as the photographs in Figure 2.3 show. Thus, it was not feasible to obtain reliable contact angles below 9° using this approach. Other than that, at lower temperatures, the oxide layer was chemically stable and physically robust on the disc top surface, as has also been noted in Reference [69].

Surface chemistry

In the earlier section, the dependence of contact angle θ on heating temperature T_h and heating time t_h was studied quantitatively. To explain the result qualitatively, the oxide formation should be understood.

Both Cu_2O and CuO can form on a copper surface during its thermal oxidation in air, as described by the chemical reactions,

$$4Cu+O_2 \rightarrow 2Cu_2O \quad \text{and} \quad 2Cu_2O+O_2 \rightarrow 4CuO.$$

In the early stage, only Cu_2O forms on the surface. As the thickness of the Cu_2O layer increases with the development of the first reaction, the generation rate of Cu_2O becomes slower as the number of Cu ions available for the first reaction at the Cu-O_2 interface decreases. When the Cu_2O layer reaches critical thickness, and the heating temperature is above 270°C [73], CuO will start to form at the Cu_2O-O_2 interface following the second reaction. However, CuO is not expected to exist below critical thickness where excessive Cu ions are available.

Following the thermal oxidation method with increasing heating temperature

T_h and/or heating time t_h, five different contact angles, i.e., θ = 77, 60, 48, 30, and 9°, were obtained on the representative disc, as shown in Figure 2.4. The unoxidized representative disc of contact angle 90° is shown as well. The surface color changes from originally dark gold to orange, to red, to grey, to green, and then to brown with the development of thermal oxidation. These unoxidized and oxidized surfaces were characterized by X-ray diffraction (XRD) analysis to further understand the essence of the improved wettability.

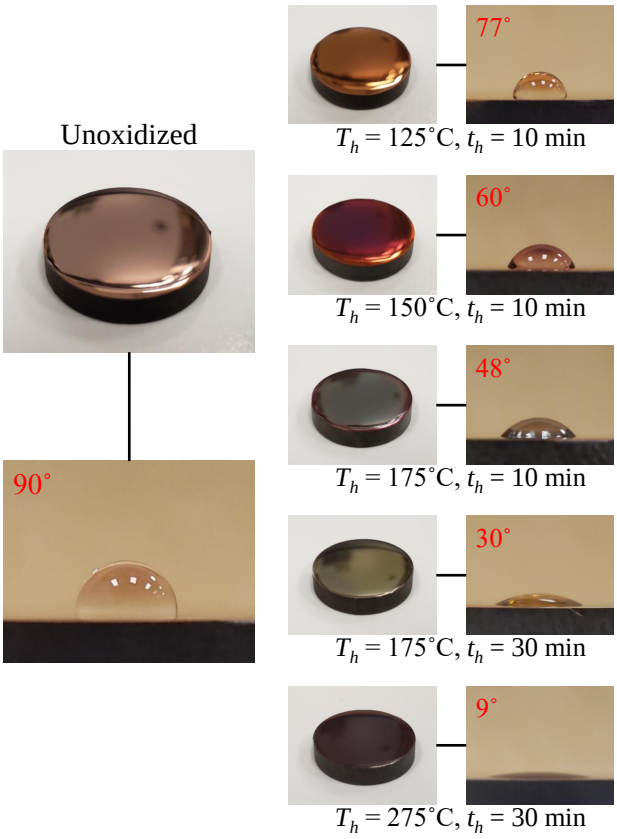

Figure 2.4: Photographs of the unoxidized and oxidized representative copper discs after being heated at different temperatures T_h for different times t_h and then cooling down to room temperature and corresponding photographs of droplets on the surface

Figure 2.5 (a) shows the diffraction intensity as a function of diffraction angle 2Θ for the unoxidized and oxidized surfaces presented in Figure 2.4. The diffraction peaks at $2\Theta = 73°$ indicate that mainly Cu_2O formed and persisted on the oxidized surfaces. Only minimal CuO formed on the surface when the disc had been heated at 275°C for 30 min, as shown by the tiny peak at $2\Theta = 36°$. It agrees well with the finding by Tylecote [73] that the minimum temperature at which CuO started to form in air was 270°C. According to the study by Lawless and Gwathmey [74], here, CuO only existed at the very top of the oxide layer with a quite low level of content. In their study, the oxide layers forming on copper surfaces at temperatures between 170 and 450°C under pressures ranging from 0.8 mmHg to one-atmosphere pressure were found to mainly contain Cu_2O with CuO only forming above certain thickness.

Figure 2.5 (b) shows an enlarged view of the diffraction peaks of Cu to better differentiate the levels of oxygen content within the different surfaces. These peaks monotonically shift to the right with the development of thermal oxidation. It should be attributed to that the doped oxygen atoms decreased the distances between the lattice planes within the oxide layer. The correlation between interplanar distance d_i and its incident angle Θ is described by Bragg's law,

$$n\lambda_X = 2d_i \sin\Theta, \tag{2.1}$$

where n is a positive integer, and λ_X represents the wavelength of the X-ray used for XRD analysis. In Figure 2.5, $\lambda_X = 0.154$ nm as the incident X-ray was of Cu K-α energy. According to Bragg's law, the incident angle Θ increases with decreasing interplanar distance d_i for a given diffraction peak. Therefore, the peaks in Figure 2.5 (b) gradually shift to the right. Meanwhile, due to phase transformation caused by the lattice strain, the peaks tend to split. Since the surface free energy increases with more oxygen atoms doped into the copper surface [75], the corresponding contact angle θ decreases.

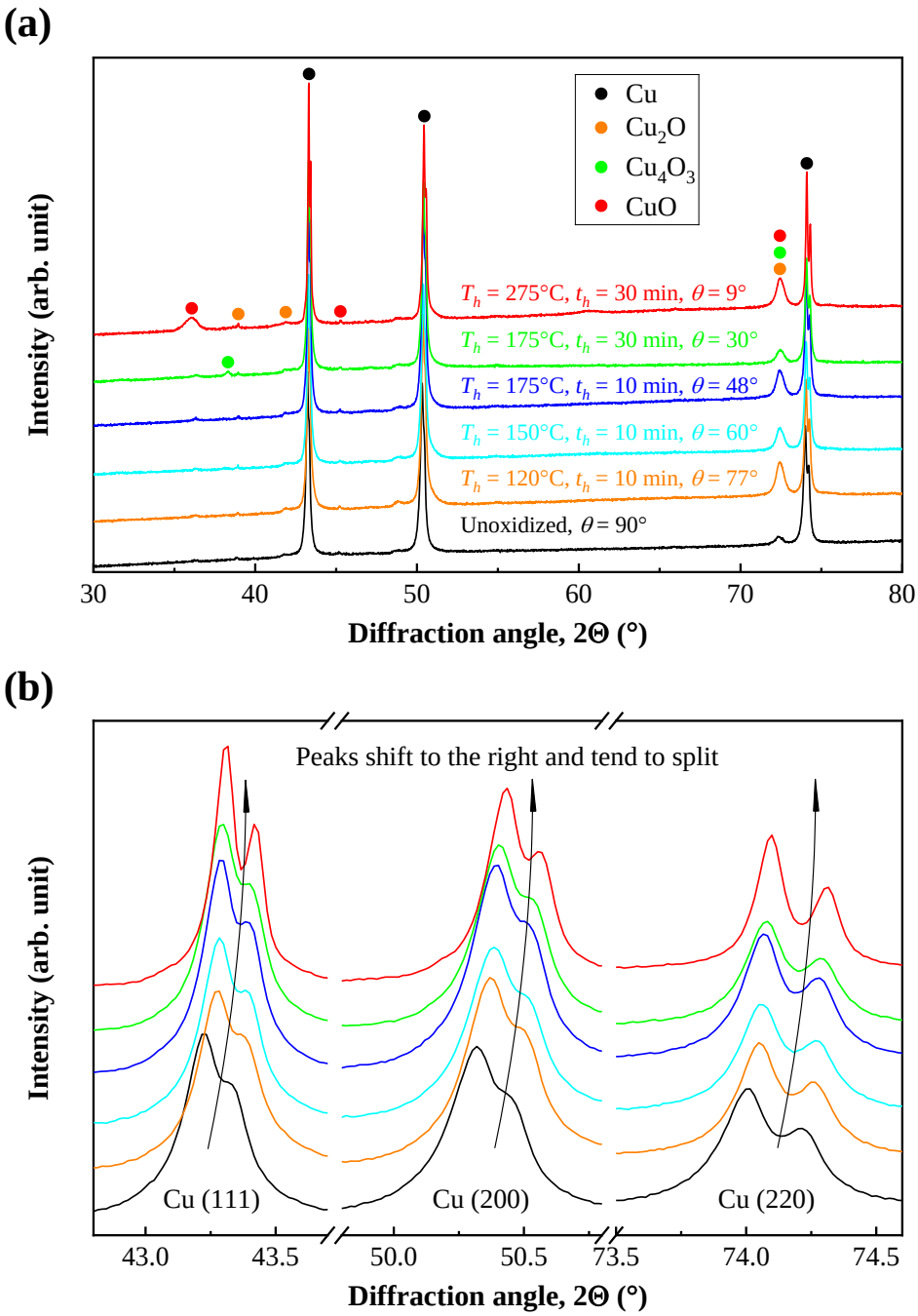

Figure 2.5: (a) Regular and (b) enlarged views of XRD patterns of the unoxidized and oxidized surfaces presented in Figure 2.4

It is worth noting that Takemura *et al.* [76], in their study, found the surface roughness nearly unchanged, namely, $\Delta Ra < 0.05$ μm, when a copper sheet had been heated at a temperature lower than 300°C for a time less than 60 min. Since all the oxidized discs in this study were prepared within this range, even including their cooldown periods, the improved wettability should be attributed to the intrinsic contact angle change caused by the oxide layer rather than the surface topography change. The plain discs of different contact angles θ used in the boiling experiments were obtained following the method described above.

2.1.2 Structured surfaces

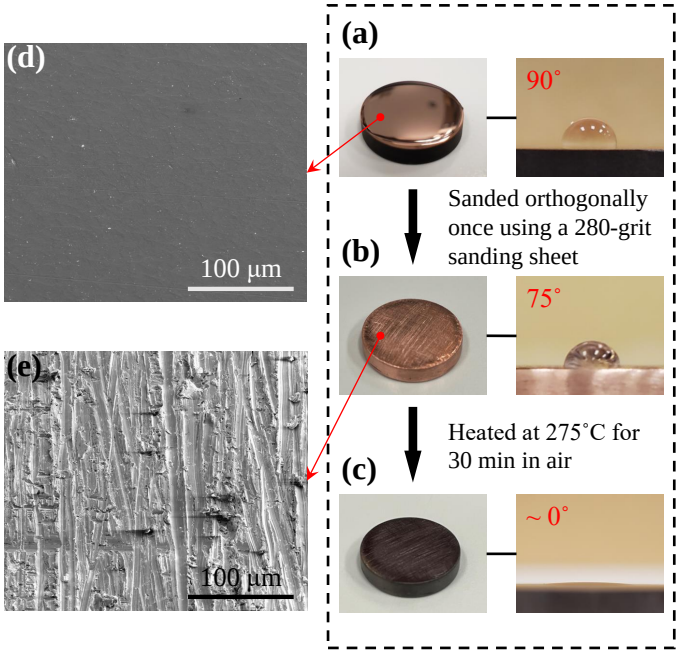

Figure 2.6: Photographs illustrating how (a) an unoxidized plain copper disc was made into (b) a partially wetted structured copper disc and then made into (c) a fully wetted structured copper disc. SEM images of the (d) plain and (e) structured surfaces in top view.

To fabricate a structured surface in a simple way, a plain disc, prepared following the polishing routine with no oxidation, was sanded orthogonally once using a 280-grit sanding sheet. Then, the contact angle decreased from 90 to 75° because of greater surface roughness, as shown in Figures 2.6 (a) and (b). A fully wetted structured surface can be prepared with one more step following the oxidation method proposed in the earlier section: heating the sanded disc at 275°C for 30 min in air. The contact angle then decreased to 0°, as shown in Figure 2.6 (c). Scanning electron microscope (SEM) images are shown in Figures 2.6 (d) and (e) for visualizing the surface topography difference between the plain and structured surfaces. In contrast to the plain surface, the structured surface features microgrooves, whose width and depth were both around 10 μm. In these ways, the partially and fully wetted structured discs were obtained and featured contact angles $\theta = 75$ and 0°, respectively.

2.2 Experimental apparatus

Figure 2.7 (a) shows a schematic of the experimental apparatus assembled to measure boiling heat transfer data of saturated water at normal earth gravity and one-atmosphere pressure for horizontal flat heaters. The whole experimental apparatus mainly consisted of two major sections: a heating base and a container of boiling water.

2.2.1 Heating base

Aside from a sample disc serving as the heater, the heating base was made up of a copper block (110 Cu), inner four cartridge heaters (CIR-30224, Omega Engineering), and an outer ceramic fiber pedestal, as shown in Figure 2.7 (a). Figure 2.8 shows photographs of the (a) copper block and (b) cartridge heaters with

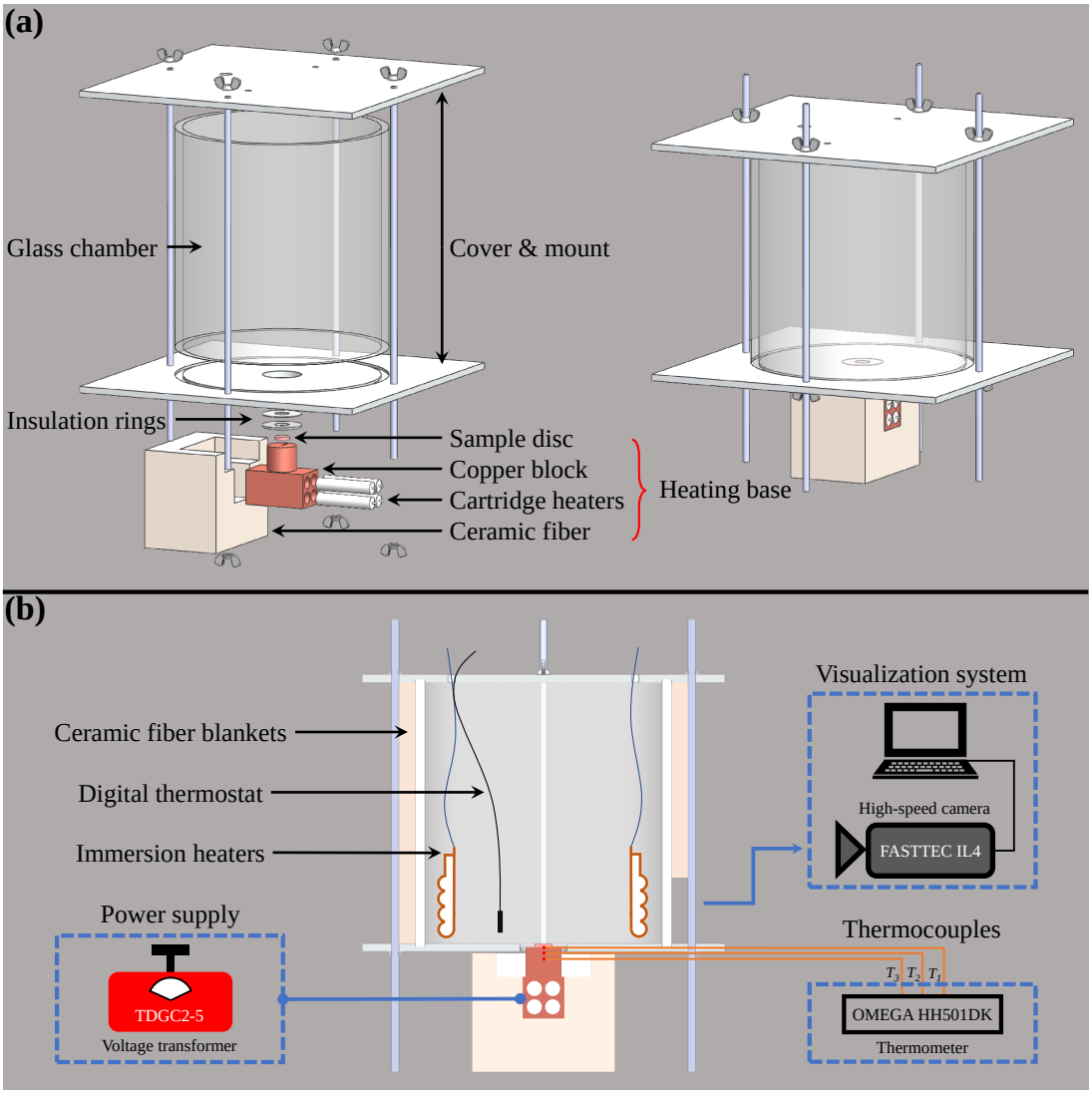

Figure 2.7: (a) Schematic of the experimental apparatus before (left) and after (right) assembly. (b) Sectional view of the assembled experimental apparatus and sketches of the associated instruments.

their dimensions labeled. The upper cylindrical part (3.0 cm diameter, 2.5 cm height) of the copper block was used for conducting heat to the disc, whereas the four cartridge heaters (1.3 cm diameter, 5.7 cm length) with a maximum heating power of 500 W each were embedded in the lower cuboidal part (3.5 cm $\times$ 6.4 cm $\times$ 3.5 cm) of the copper block. The clearances between the copper block and cartridge heaters were filled with thermal cement (OB-600, Omega Engineering) to ensure they were completely contacted. To minimize heat loss, ceramic fiber boards (2732F, BXI) featuring low thermal conductivity were fabricated into the pedestal to insulate the copper block from its surroundings. In practice, for better thermal insulation, additional ceramic fiber blankets of thickness 2 cm were wrapped around the heating base, and their fragments were used to fill up the remaining space between the copper block and pedestal.

2.2.2 Container

Look back at Figure 2.7 (a), a glass chamber (20.0 cm inner diameter, 30.0 cm height), set over the heating base, was mounted on an aluminum plate and covered by another aluminum plate on its top for storing boiling water. An opening of diameter 4.0 cm was machined at the center of the bottom plate to match the sample disc. Three openings were machined at the cover plate: two of diameter 1.0 cm for passing wires and one of diameter 2.0 cm for connecting a hose. Vapor generated during boiling was led via this hose to a bucket filled with cool water. It was condensed in such a way and poured back to the container regularly.

2.2.3 Instruments

Figure 2.7 (b) shows a sectional view of the assembled experimental apparatus and sketches the associated instruments. Two immersion heaters rated at 300W each were submerged in the water to maintain it near its saturation temperature.

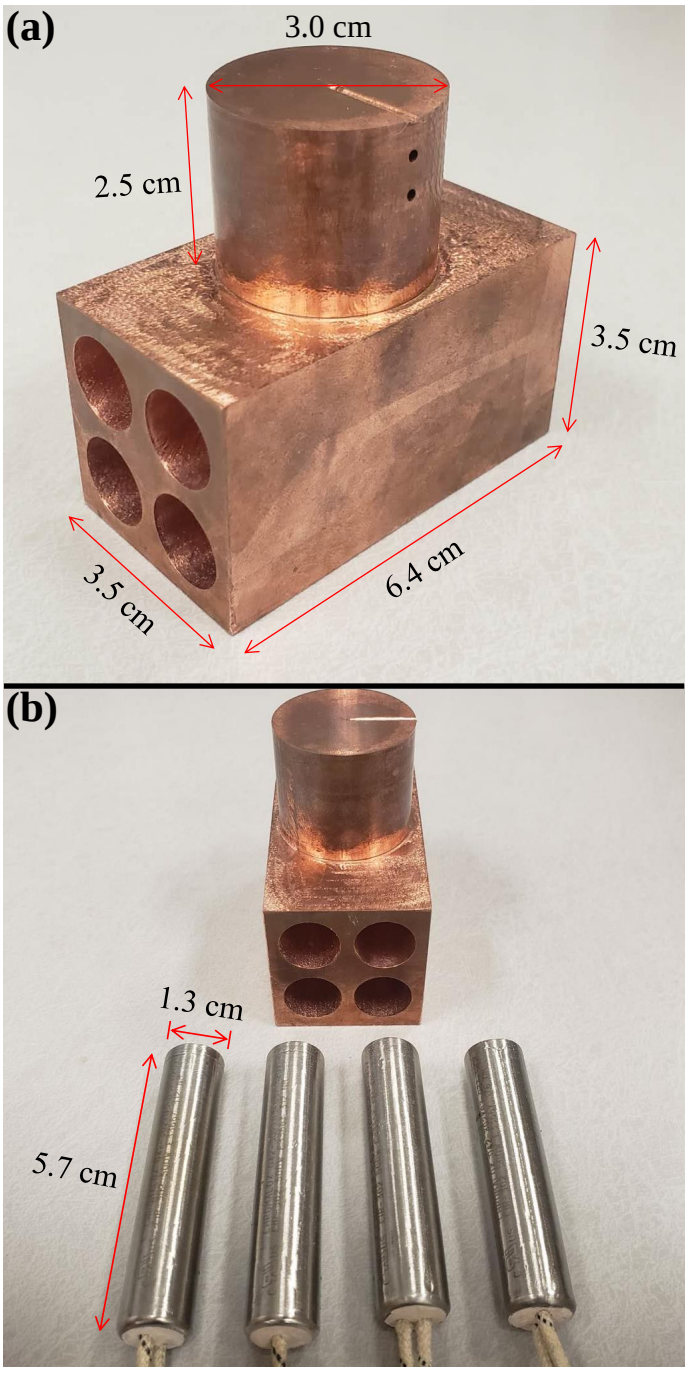

Figure 2.8: Photographs of the (a) copper block and (b) cartridge heaters with their dimensions labeled

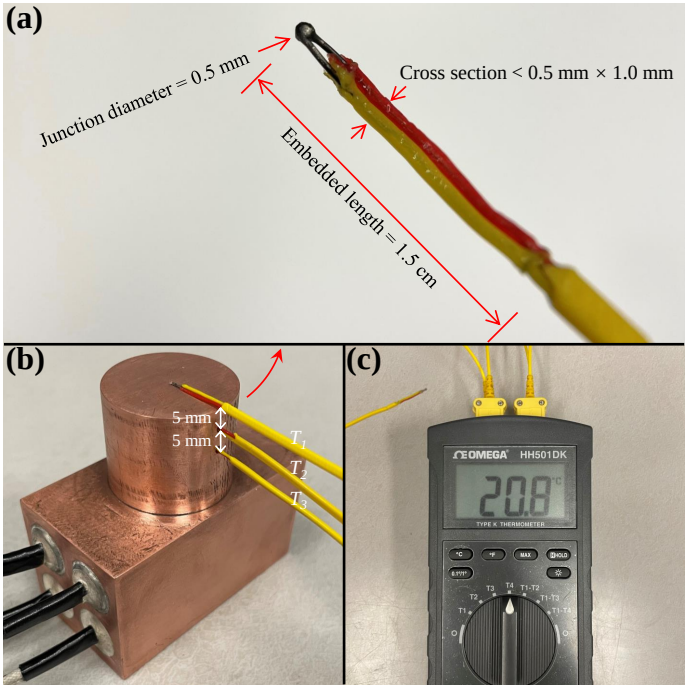

Figure 2.9: Photographs of the thermocouples T_1, T_2, and T_3 with their (a) dimensions and (b) locations labeled. (c) Photograph of the thermometer. 20.8°C shown on the digital screen indicated room temperature in the laboratory.

Their on/off switch was controlled by a digital thermostat (DTC101, Digiten), which monitored the water temperature and formed a feedback loop with the immersion heaters to ensure the water was saturated. Besides, ceramic fiber blankets of thickness 2 cm were wrapped around the glass chamber for reducing heat dissipation while leaving an uncovered window for simultaneous observation using a high-speed camera (IL4, Fastec Imaging). The four cartridge heaters embedded in the copper block were connected to an adjustable voltage transformer (TDGC2-5, YaeCCC) on the other end. By increasing the supplied voltage from 0 to 120 Volts, the heating base could provide heating power from 0 to 2000 W.

Temperatures at the centerline of the cylindrical part of the copper block were measured with three type-K thermocouples of the same dimensions, as shown in

Figure 2.9 (a). Their measuring junctions were of diameter 0.5 mm, and their lengths embedded in the cylinder were 1.5 cm. The thermocouples, denoted by T_1, T_2, and T_3, were placed along the vertical axis downward in order with a spacing of 5 mm between each, as shown in Figure 2.9 (b). The holes of diameter 1 mm, through which the thermocouples were inserted, were filled with thermal cement (OB-600, Omega Engineering) to minimize their effect on the temperature distribution within the cylinder and maintain the thermocouples in their desired positions. This cement is thermally conductive but electrically insulated, thus insulating the thermocouple wires from the surroundings in addition to their PFA insulation skin until their junctions. To monitor and record the temperatures in real time, as shown in Figure 2.9 (c), all the thermocouples were connected to a digital thermometer (HH501DK, Omega Engineering) with a certificate of NIST traceable calibration. Before use, they were calibrated again using a high-precision platinum RTD thermometer (6412, Control Company) of uncertainty $\pm$ 0.05°C for temperatures ranging from 100 to 300°C in a sand bath. The uncertainty in measuring temperatures with the thermocouples was less than $\pm$ 0.2°C for temperatures ranging from 100 to 250°C and less than $\pm$ 0.4°C for temperatures ranging from 250 to 300°C.

2.2.4 Installation

Figure 2.10 illustrates the installation of a sample disc. The disc of a given diameter, D = 1.5 cm in Figure 2.10, was bonded on the top of the cylindrical part of the copper block by graphite adhesive (931C, Resbond). Since boiling was only desired on the disc top surface, the remaining area of the cylinder top and the outer edge of the disc should be thermally insulated. Thus, the disc was surrounded by a PTFE ring (upper, 1 mm thickness) and a fiberglass ring (lower, 2 mm thickness) for thermal insulation. Both rings featured inner diameters that

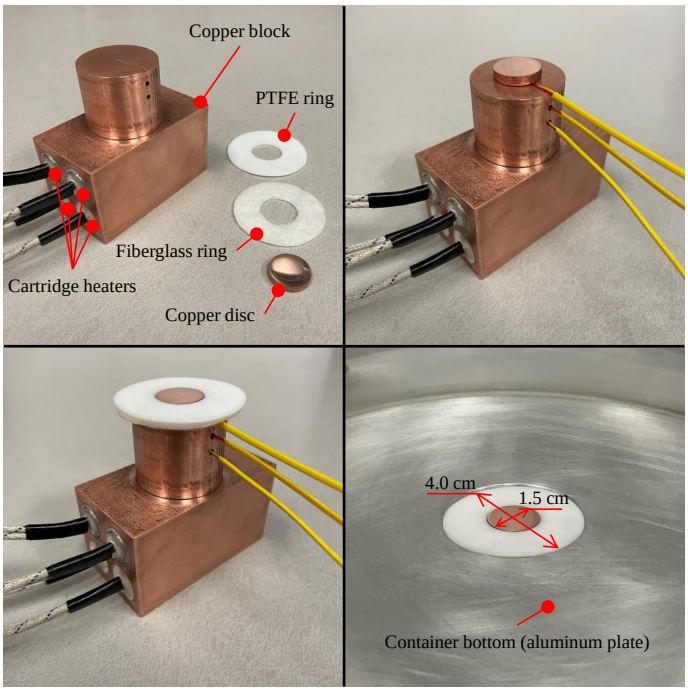

Figure 2.10: Demonstration of installing a 1.5-cm-diameter disc on the copper block and matching it with the insulation rings and container bottom

were equal to the disc diameter. Their outer diameters were 4.0 cm and consistent with the diameter of the opening at the bottom plate. The clearances were sealed using silicone sealant (08663, 3M) to avoid leakage. With the insulation rings blocking the heat transfer from the undesired area, boiling heat transfer only occurred on the sample disc top surface.

To change the surrounding vessel size for the disc, glass tubes of different inner diameters D_T were vertically placed around it, respectively. The ratio of heater size to surrounding vessel size D/D_T was made adjustable from 1 ($D = D_T$, a glass tube of inner diameter equal to the disc diameter) to about 0 ($D \ll D_T$, no glass tube). In such a way, the effect of surrounding vessel size can be individually studied in a full range. Figure 2.11 illustrates changing the surrounding vessel size for a 1.5-cm-diameter disc. Glass tubes of inner diameters (a) $D_T = 1.5$ cm,

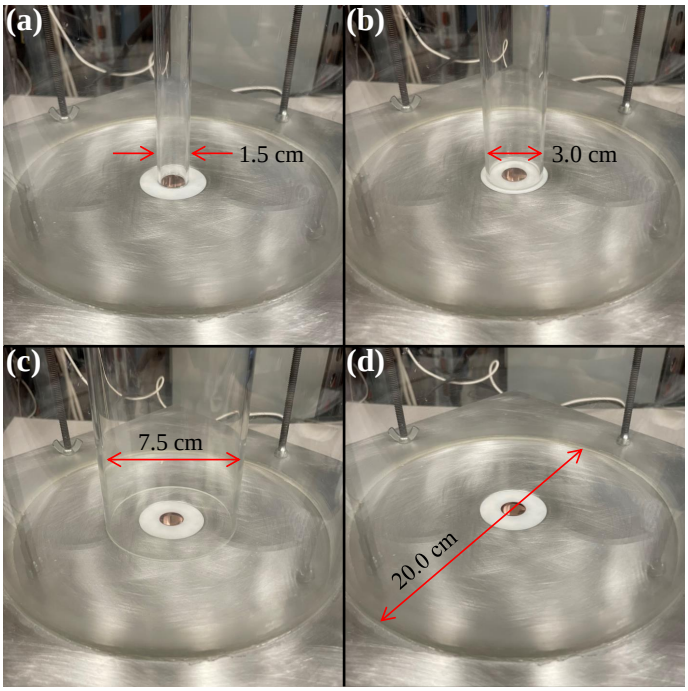

Figure 2.11: Demonstration of placing glass tubes of inner diameters (a) D_T = 1.5 cm, (b) D_T = 3.0 cm, and (c) D_T = 7.5 cm around a 1.5-cm-diameter disc. (d) D_T = 20.0 cm when no glass tube was placed.

(b) D_T = 3.0 cm, and (c) D_T = 7.5 cm were placed around the disc, respectively. When no glass tube was placed, the surrounding vessel size was the inner diameter of the glass chamber, namely, (d) D_T = 20.0 cm. Correspondingly, the ratios of heater size to surrounding vessel size were (a) $D/D_T = 1$, (b) $D/D_T = 0.5$, (c) $D/D_T = 0.2$, and (d) $D/D_T = 0.075 \approx 0$. The same strategy was employed for all the test discs in this study.

2.3 Experimental procedure

After assembling the experimental apparatus as described in the earlier section, several steps were rigorously taken before starting a boiling experiment. Deion-

ized water was deaerated by boiling in an electric kettle and then poured into the container. Once completed, the immersion heaters started to work and kept the water near its saturation temperature. The atmospheric pressure in the laboratory was measured to be 101.3 kPa using a barometric pressure sensor built in a smartphone, and the water saturation temperature was about 100°C. In practice, however, the water temperature cannot be perfectly uniform: the water near the immersion heaters was at its saturation temperature while the remaining was at lower temperatures. As monitored by the digital thermostat, the pool water was maintained at 99 ± 1°C.

A boiling experiment began with turning on the adjustable voltage transformer. It was adjusted by about 2 Volts each time to change the heating power of the cartridge heaters. The heat generated was conducted along the cylindrical part of the copper block to the disc and then transferred to the water by boiling. When a steady state was reached, the supplied voltage U and temperatures T_1, T_2, and T_3 were recorded. The steady-state condition was determined based on a criterion that the temperatures measured with the thermocouples changed less than 0.2°C in 1 min. It typically took 15 to 20 min after changing the supplied voltage to obtain steady-state temperatures. Meanwhile, the high-speed camera recorded the corresponding vapor removal pattern on the disc. With the input power increased in steps, the heat transfer started within natural convection regime and gradually developed into nucleate boiling regime. The power was immediately cut off when a sudden increase in T_1 appeared on the thermometer, which indicated a shift to transition boiling. Thus, the boiling heat transfer data were recorded up to CHF. In each boiling experiment, the liquid height was maintained at about 20 cm by regularly adding deaerated water.

Note that the contact angle changed after each boiling experiment. It should be attributed to that the residual oxygen in water can further oxidize the disc surface

Table 2.1: Pre-, post-boiling, and mean contact angles of the boiling cases on 1.5-cm-diameter discs

Case no.	Pre-boiling contact angle (°)	Post-boiling contact angle (°)	Mean contact angle, θ (°)
1 (plain)	90 ± 2	69 ± 4	80
2 (plain)	74 ± 2	51 ± 6	63
3 (plain)	59 ± 3	46 ± 5	53
4 (plain)	45 ± 3	29 ± 4	37
5 (plain)	28 ± 4	25 ± 4	27
6 (plain)	8 ± 3	15 ± 5	12
7 (structured)	75 ± 4	56 ± 6	66
8 (structured)	~ 0	~ 0	0

even the water had been deaerated [77–79]. Besides, slight fouling was found on the post-boiling discs, which might also change the contact angle. Therefore, the contact angle was measured before and after each boiling experiment, and a mean value of the pre- and post-boiling contact angles was used to correlate the CHF data. Table 2.1 lists the pre-, post-boiling, and mean contact angles of the boiling cases on 1.5-cm-diameter discs. Generally, on a copper surface with water as the test liquid, the contact angle decreases with time due to surface oxidation. In this work, no attempt was made to correlate the decrease in contact angle with boiling time. It should also be noted that with the oxidation of an initially highly oxidized copper surface, the oxide layer may become thick enough to peel off. This, in turn, can lead to an increase in the post-boiling contact angle, as given in Table 2.1.

2.4 Summary

Throughout this study, copper discs of thickness d = 3 mm and diameters D = 1.0, 1.5, and 2.0 cm were used as horizontal flat heaters, on which saturated

Table 2.2: Experimental parameters: heater size D, contact angle θ, surface type, and surrounding vessel size D_T

Heater size, D (cm)	Contact angle[1], θ (°)	Surface type	Surrounding vessel size, D_T (cm)			
1.0	10 27 43 54 65 80	Plain	1.0	2.0	5.0	
	0 66	Structured				
1.5	12 27 37 53 63 80	Plain	1.5	3.0	7.5	20.0
	0 66	Structured				
2.0	12 24 39 51 60 80	Plain	2.0	4.0	10.0	
	0 62	Structured				

[1] Mean contact angle: average of the pre- and post-boiling contact angles of each boiling experiment.

deionized water was boiled. Plain sample discs of contact angles θ ranging from 90 to 9° were obtained by thermal oxidation. Structured sample discs of contact angles $\theta = 75$ and 0° were obtained by sole sanding and sanding coupled with thermal oxidation, respectively. Furthermore, the surrounding vessel size was changed by placing glass tubes of different inner diameters D_T around the discs. Table 2.2 summarizes the parameters of all the experiments employed to study the individual and interacting effects of heater size, contact angle, surface structure, and surrounding vessel size on nucleate boiling heat transfer of saturated water.

CHAPTER 3

Data reduction

This chapter presents the methods of calculating the boiling heat flux and corresponding surface temperature using the temperatures measured by thermocouples at each steady state. Uncertainty analysis is also performed for the calculated heat flux and surface temperature.

3.1 Energy balance method

Figure 3.1 shows a sectional view of the copper block with a 1.5-cm-diameter disc bonded on top with the graphite adhesive. The heat generated from the four cartridge heaters embedded in the lower cuboidal part of the copper block was conducted along the upper cylindrical part of the copper block to the disc and then transferred to the water in the form of boiling on the disc top surface. The ceramic fiber thermally insulated the remaining area. The heat generation rate $\dot{Q}$ of the cartridge heaters was expressed as

$$\dot{Q} = \frac{4U^2}{R_h}, \tag{3.1}$$

where $R_h = 29.0\ \Omega$ is the average electrical resistance of the cartridge heaters (See Appendix A). If there was no heat loss, the boiling heat flux q should be

$$q = \frac{4U^2}{AR_h}, \tag{3.2}$$

where A is the top surface area of the disc. Equation (3.2) calculates the upper limit of the heat flux q by considering no heat loss.

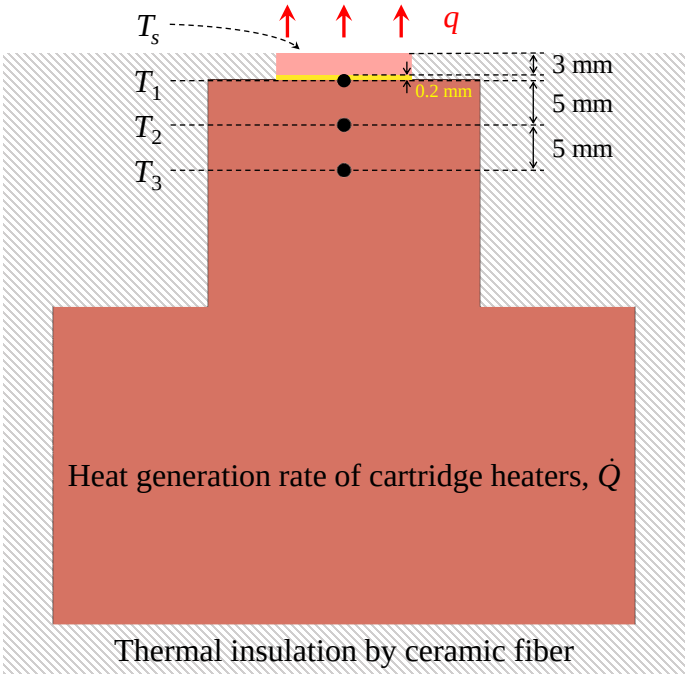

Figure 3.1: Sectional view of the copper block with a 1.5-cm-diameter disc bonded on top with the graphite adhesive

However, heat loss was inevitable during the experiment because of (i) a non-zero thermal conductivity of the ceramic fiber and (ii) natural convection of air surrounding the heating base. Radiation was ignored considering that aluminum tapes pasted on the ceramic fiber featured low emissivity. Accordingly, the heat loss was modeled as natural convective heat transfer between air and the outer surface of the heating base. Assuming that the heating base was cubic of side length 10 cm and natural convection of air occurred on its four sides with heat transfer coefficient $h_{air} = 10$ W/m^2 K, the heat loss $\Delta\dot{Q}$ was given by

$$\Delta\dot{Q} = h_{air}\,(T_o - T_{air})\,A_o, \tag{3.3}$$

where T_o is the outer surface temperature of the heating base, T_{air} is the air temperature, and $A_o = 0.04$ m^2 is the lateral surface area of the heating base. Based on energy balance, subtracting Equation (3.3) from Equation (3.1) gave

the boiling heat flux q as

$$q = \frac{4U^2}{AR_h} - \frac{h_{air}\left(T_o - T_{air}\right)A_o}{A}. \tag{3.4}$$

As Equation (3.3) overestimates the heat loss by ignoring the heat transfer from the container bottom and introducing an exaggerated heat transfer coefficient h_{air}, Equation (3.4) calculates the lower limit of the heat flux q. Thus, the heat flux q should be within a range set by Equations (3.2) and (3.4), i.e.,

$$\frac{4U^2}{AR_h} - \frac{h_{air}\left(T_o - T_{air}\right)A_o}{A} < q < \frac{4U^2}{AR_h}. \tag{3.5}$$

From the aspect of energy balance, Equation (3.5) estimates the boiling heat flux q using the measured voltage U and outer surface temperature of the heating base T_o at each steady state. However, its accuracy is limited because of the rough estimation made on heat loss. Moreover, the corresponding surface temperature T_s cannot be obtained following this method. Therefore, another method using spatial temperature distribution was developed. It gives more accurate heat flux q and simultaneously calculates the corresponding surface temperature T_s.

3.2 Spatial temperature distribution method

Assuming that no heat was dissipated through the ceramic fiber, the heat conduction domain can be regarded as a collection of the cylindrical part of the copper block, graphite adhesive, and disc. To the best of the author's knowledge, due to the irregular geometry, the boiling heat flux q and surface temperature T_s cannot be calculated analytically. However, they can be determined numerically using the spatial temperature distribution at each steady state, namely, the measured temperatures T_1, T_2, and T_3.

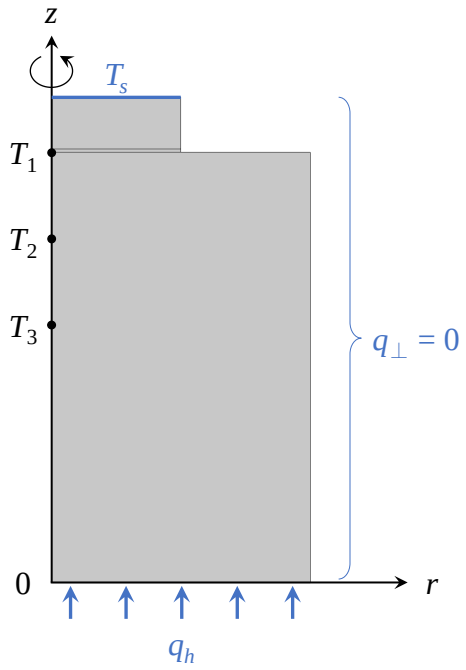

Figure 3.2: Two-dimensional axisymmetric view of the computational domain consisting of the copper cylinder, graphite adhesive, and disc with boundary conditions labeled

3.2.1 Computational domain and assumptions

Figure 3.2 shows a two-dimensional axisymmetric view of the computational domain built in COMSOL. To make the problem mathematically tractable, the following assumptions were made: (i) heat conduction within the domain was steady-state, (ii) all materials were isotropic with constant thermal conductivities, and (iii) interfacial thermal resistances were neglected.

3.2.2 Governing equation and boundary conditions

Under the above assumptions, the local temperature T within each subdomain was governed by a two-dimensional steady-state heat diffusion equation in r-z

coordinates, i.e.,

$$\frac{\partial}{r\partial r}\left(r\frac{\partial T_i}{\partial r}\right)+\frac{\partial^2 T_i}{\partial z^2}=0, \tag{3.6}$$

where the subscript i denotes the subdomains, namely, the copper cylinder, graphite adhesive, and disc.

Coupling the temperature fields of the subdomains i and j in contact was achieved by setting the temperature and heat flux continuous across their interface, i.e.,

$$T_i|_{i\text{-}j}=T_j|_{i\text{-}j} \quad \text{and} \quad -k_i\frac{\partial T_i}{\partial \mathbf{n}}\bigg|_{i\text{-}j}=-k_j\frac{\partial T_j}{\partial \mathbf{n}}\bigg|_{i\text{-}j}, \tag{3.7}$$

where k is the thermal conductivity, and $\mathbf{n}$ is the unit normal vector at any given point on the interface denoted by the subscript i-j.

The heat flux through the z-axis vanished due to the axial symmetry of the domain, i.e.,

$$-k_i\frac{\partial T_i}{\partial r}\bigg|_{z\text{-}axis}=0. \tag{3.8}$$

Besides, there was no heat flux through the thermally insulated surfaces, i.e.,

$$-k_i\frac{\partial T_i}{\partial \mathbf{m}}=0, \tag{3.9}$$

where $\mathbf{m}$ is the unit normal vector at any given point on the thermally insulated surfaces. Heat input q_h was imposed on the bottom to model the heating of the cartridge heaters, i.e.,

$$-k_i\frac{\partial T_i}{\partial z}\bigg|_{bottom}=q_h. \tag{3.10}$$

Given the fact that the disc was made of 110 Cu featuring high thermal conductivity, a boundary condition of constant temperature T_s was applied on the disc top surface, i.e.,

$$T_i|_{top}=T_s. \tag{3.11}$$

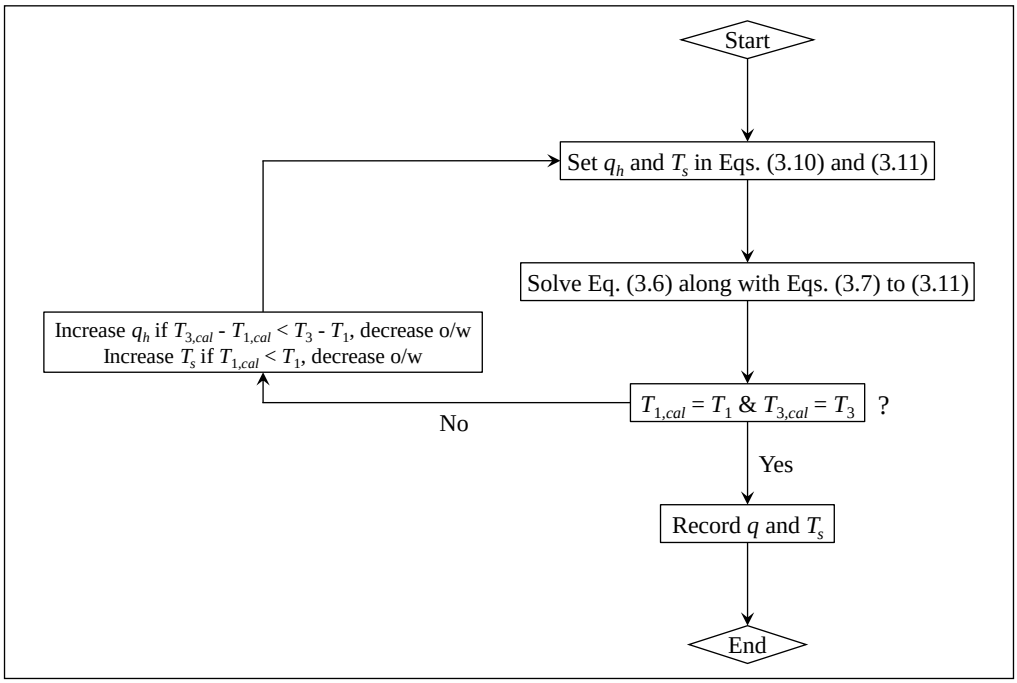

Figure 3.3: Algorithm of calculating the boiling heat flux q and surface temperature T_s using the measured temperatures T_1 and T_3 at each steady state

3.2.3 Method of solution

As this heat transfer problem was steady-state with no heat source, only the thermal conductivities of the subdomains were needed for its solution. The copper block and disc were both made of 110 Cu featuring thermal conductivity $k_c = 386$ W/m K. The thermal conductivity of the graphite adhesive is $k_g = 5.77$ W/m K. Unlike a classic heat transfer problem, namely, solving spatial temperature distribution using the governing equation along with the specified boundary conditions, the temperatures T_1, T_2, and T_3 were known here, while the heat input at the bottom q_h and the temperature at the disc top surface T_s were the unknowns to be solved.

Figure 3.3 depicts a trial-and-error algorithm of calculating the boiling heat

flux q and surface temperature T_s using the measured temperatures T_1 and T_3 at each steady state. Once the heat input q_h in Equation (3.10) and the surface temperature T_s in Equation (3.11) are set, the spatial temperature distribution of the computational domain can be obtained by solving the governing Equation (3.6) along with the boundary Equations (3.7) to (3.11) in COMSOL. Only when the calculated temperatures $T_{1,cal}$ and $T_{3,cal}$ match the measured temperatures T_1 and T_3, the heat input q_h and surface temperature T_s are the correct boundary conditions, and the boiling heat flux q is obtained accordingly. If not, the heat input q_h and surface temperature T_s should be adjusted until the temperatures match. Specifically, q_h should be increased if $T_{3,cal} - T_{1,cal} < T_3 - T_1$ otherwise should be decreased, and T_s should be increased if $T_{1,cal} < T_1$ otherwise should be decreased. The measured temperature T_2 is not involved in the algorithm but compared with the calculated temperature $T_{2,cal}$ for further validation.

3.2.4 Results for example cases

Table 3.1 tabulates the measured voltages U, outer surface temperatures of the heating base T_o, and temperatures T_1, T_2, and T_3 for six example cases. Cases 1 and 2 are on a 1.0-cm-diameter disc and feature low and high heat fluxes, respectively; Cases 3 and 4 are on a 1.5-cm-diameter disc and feature low and high heat fluxes, respectively; Cases 5 and 6 are on a 2.0 cm-diameter disc and feature low and high heat fluxes, respectively. The boiling heat fluxes q and surface temperatures T_s for these cases were calculated using the spatial temperature distribution following the above algorithm.

Figure 3.4 shows the distribution of the local heat flux q_{local} through the disc top surface along the radial direction for Cases (a) 1, (b) 2, (c) 3, (d) 4, (e) 5, and (f) 6. It indicates that the local heat flux was almost uniform regardless of the disc diameter and heat flux magnitude. As shown in Figure 3.4, on each surface,

Table 3.1: Measured voltages U, outer surface temperatures of the heating base T_o, and temperatures T_1, T_2, and T_3 for six example cases

Case no.	Disc diameter, D (cm)	Heat flux, q	Voltage, U (Volts)	Outer surface temperature, T_o (°C)	Temperature, T_1 (°C)	Temperature, T_2 (°C)	Temperature, T_3 (°C)
1	1.0	Low	14	41.8	123.8	125.9	126.7
2		High	22	43.0	148.2	153.9	156.1
3	1.5	Low	20	46.2	122.2	124.6	126.0
4		High	32	48.8	147.0	153.8	157.6
5	2.0	Low	24	47.5	120.3	122.7	124.4
6		High	43	51.3	147.9	155.8	161.5

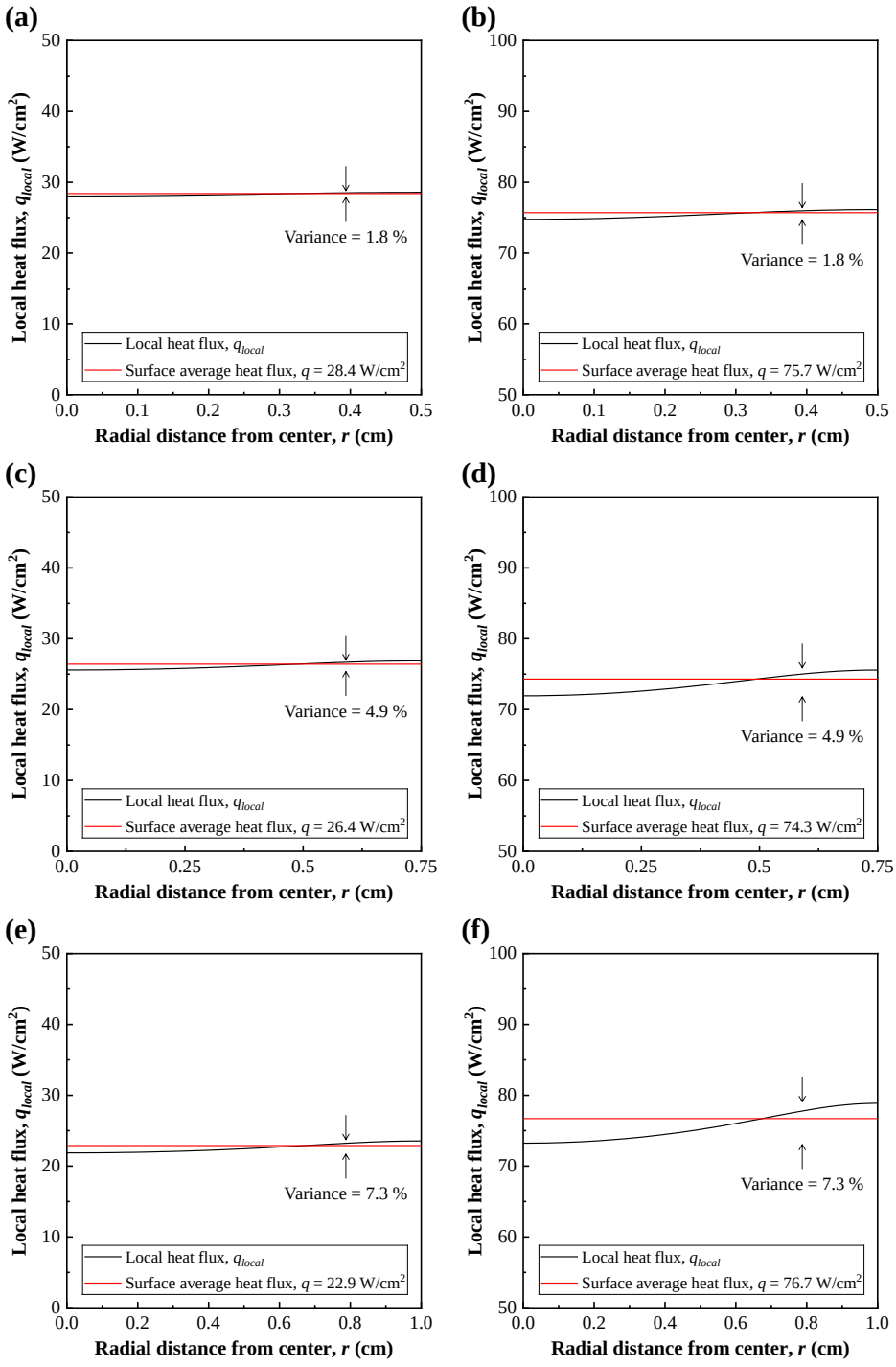

Figure 3.4: Distribution of the local heat flux q_{local} through the disc top surface along the radial direction for Cases (a) 1, (b) 2, (c) 3, (d) 4, (e) 5, and (f) 6

Table 3.2: Heat fluxes q and surface temperatures T_s for Cases 1 to 6 calculated using the spatial temperature distribution considering no heat loss

Case no.	Disc diameter, D (cm)	Heat flux, q (W/cm^2)	Surface temperature, T_s (°C)
1	1.0	28.4	112.2
2		75.7	117.4
3	1.5	26.4	111.7
4		74.3	117.2
5	2.0	22.9	111.2
6		76.7	117.3

from center to edge, the local heat flux q_{local} shows a small variance, i.e., 1.8 % to 7.3 % for Cases 1 to 6. Given the uniform distribution, the surface average heat flux was employed to represent the boiling heat flux q. Table 3.2 tabulates the calculated heat fluxes q and surface temperatures T_s for Cases 1 to 6.

Note that for boiling on a given surface, the boiling heat flux is a function of surface temperature. Thus, the uniform local heat flux also indicates that the boundary condition of constant temperature applied on the disc top surface was valid.

3.2.5 Heat loss effect

Heat loss was absent in the earlier computation. Its effects on the calculated heat flux q and surface temperature T_s were examined by modeling the heat dissipation through the ceramic fiber in COMSOL. Figure 3.5 shows a two-dimensional axisymmetric view of the modified computational domain with the ceramic fiber taken into account. Here, the ceramic fiber was modeled as a cylindrical shell of outer diameter 10 cm with thermal conductivity $k_f = 0.082$ W/m K. Aside from the same assumptions made to make the problem mathematically tractable,

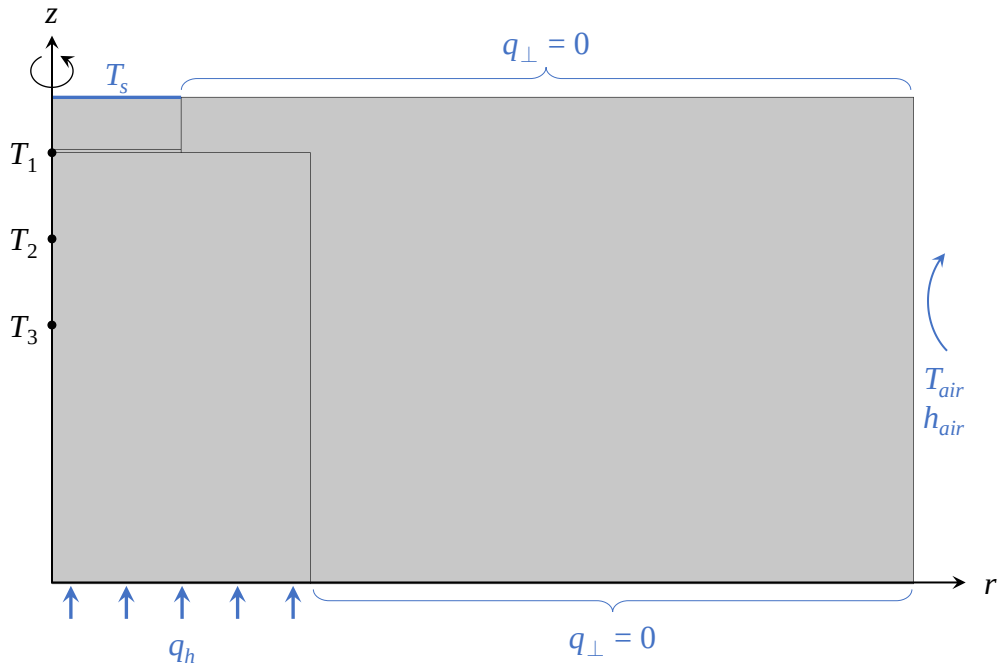

Figure 3.5: Two-dimensional axisymmetric view of the computational domain consisting of the copper cylinder, graphite adhesive, disc, and ceramic fiber with boundary conditions labeled

the governing equation and boundary conditions were modified accordingly. Equations (3.6) and (3.7) were extended to the subdomain of the ceramic fiber. Besides, the boundary Equations (3.8) to (3.11) were kept the same except for Equation (3.9), which was replaced by a boundary condition describing the heat loss from the right boundary. The heat loss was modeled as natural convective heat transfer between air and the outer surface of the ceramic fiber, i.e.,

$$-k_i \frac{\partial T_i}{\partial z}\Big|_{bottom} = 0, \quad -k_i \frac{\partial T_i}{\partial z}\Big|_{top} = 0, \quad \text{and} \quad -k_i \frac{\partial T_i}{\partial r}\Big|_{right} = h_{air}\left(T_i - T_{air}\right). \quad (3.12)$$

With the modified governing equation and boundary conditions, the heat fluxes q and surface temperatures T_s for Cases 1 to 6 were calculated using the spatial temperature distribution following the algorithm depicted in Figure 3.3. Table

Table 3.3: Heat fluxes q and surface temperatures T_s for Cases 1 to 6 calculated using the spatial temperature distribution considering heat loss

Case no.	Disc diameter, D (cm)	Heat flux, q (W/cm^2)	Surface temperature, T_s (°C)
1	1.0	27.4	112.7
2		75.5	117.6
3	1.5	26.3	111.7
4		74.1	117.4
5	2.0	23.1	111.1
6		76.6	117.4

3.3 tabulates the calculated heat fluxes q and surface temperatures T_s considering heat loss.

As shown in Tables 3.2 and 3.3, the heat fluxes q and surface temperatures T_s calculated considering no heat loss are in good agreement with those calculated considering heat loss for all the example cases. The differences are less than 3.6 % for the heat fluxes q and 0.4 % for the surface temperatures T_s, respectively. It indicates that the heat dissipation through the ceramic fiber hardly affected the dependences of the heat flux q and surface temperature T_s on the spatial temperature distribution. Therefore, heat loss was reasonably neglected when calculating the boiling heat flux q and surface temperature T_s following the spatial temperature distribution method.

3.3 Uncertainty analysis

3.3.1 Uncertainties of boiling heat flux and surface temperature

The linear dependence between the boiling heat flux q and temperature difference $(T_3 - T_1)$ was described by (see Appendix B)

$$q \propto \frac{k_c \left(T_3 - T_1\right)}{d_t}, \tag{3.13}$$

where $d_t = 10$ mm is the distance between the thermocouples T_1 and T_3. Given the independence between k_c, d_t, and $(T_3 - T_1)$, the fractional uncertainty of the heat flux q was expressed as

$$\frac{\delta q}{q} = \sqrt{\left(\frac{\delta k_c}{k_c}\right)^2 + \left(\frac{\delta d_t}{d_t}\right)^2 + \left[\frac{\delta \left(T_3 - T_1\right)}{T_3 - T_1}\right]^2}. \tag{3.14}$$

Similarly, the linear dependence between the boiling heat flux q and temperature difference $(T_1 - T_s)$ was described by (see Appendix B)

$$q \propto \left(T_1 - T_s\right)\left(\frac{d}{k_c} + \frac{d_g}{k_g}\right)^{-1}, \tag{3.15}$$

where $d_g = 0.2$ mm is the thickness of the graphite adhesive. The rightmost term can be substituted with thermal insulance R_i, i.e.,

$$R_i = \frac{d}{k_c} + \frac{d_g}{k_g}. \tag{3.16}$$

Given the independence between d, k_c, d_g, and k_g, the uncertainty of the thermal insulance R_i was expressed as

$$\delta R_i = \sqrt{\left(\frac{d}{{k_c}^2}\delta k_c\right)^2 + \left(\frac{1}{k_c}\delta d\right)^2 + \left(\frac{d_g}{{k_g}^2}\delta k_g\right)^2 + \left(\frac{1}{k_g}\delta d_g\right)^2}. \tag{3.17}$$

Subsequently, the linear correlation between the heat flux q and temperature difference $(T_1 - T_s)$ was simplified as

$$q \propto \frac{\left(T_1 - T_s\right)}{R_i}, \tag{3.18}$$

Table 3.4: Values and uncertainties of the physical quantities involved in uncertainty analysis

Physical quantity	Value	Uncertainty
Thermal conductivity of 110 Cu, k_c (W/m K)	386	5
Thermal conductivity of graphite adhesive, k_g (W/m K)	5.77	0.01
Thickness of disc, d (mm)	3	0.01
Thickness of graphite adhesive, d_g (mm)	0.2	0.01
Distance between thermocouples T_1 and T_3, d_t (mm)	10	0.5
Temperatures, T_1, T_2, and T_3 (°C)	-	0.2
Temperature difference, $(T_3 - T_1)$ (°C)	-	$0.2\sqrt{2}$
Thermal insulance, $R_i \times 10^5$ (m^2 K/W)	4.2	0.2

and the fractional uncertainty of the temperature difference $(T_1 - T_s)$ was expressed as

$$\frac{\delta\left(T_1 - T_s\right)}{T_1 - T_s} = \sqrt{\left(\frac{\delta q}{q}\right)^2 + \left(\frac{\delta R_i}{R_i}\right)^2}. \tag{3.19}$$

As the surface temperature T_s can be written as

$$T_s = T_1 - \left(T_1 - T_s\right), \tag{3.20}$$

the uncertainty of the surface temperature T_s was then expressed as

$$\delta T_s = \sqrt{\left(\delta T_1\right)^2 + \left[\delta\left(T_1 - T_s\right)\right]^2}. \tag{3.21}$$

It is worth noting that any two of the temperatures T_1, T_2, and T_3 can be used to calculate the boiling heat flux q and surface temperature T_s following the spatial temperature distribution method. In this study, the temperatures T_1 and T_3 were chosen. It resulted in the smallest uncertainties of the heat flux q and surface temperature T_s because of the largest distance between the corresponding

Table 3.5: Heat flux uncertainties δq and surface temperature uncertainties δT_s for Cases 1 to 6

Case no.	Disc diameter, D (cm)	Heat flux uncertainty, δq (W/cm^2)	Surface temperature uncertainty, δT_s (°C)
1	1.0	3.1	1.4
2		4.8	2.3
3	1.5	2.4	1.1
4		4.3	2.1
5	2.0	2.0	0.9
6		4.3	2.1

thermocouples, as described in Equation (3.14). Table 3.4 tabulates the values and uncertainties of the physical quantities involved in uncertainty analysis.

3.3.2 Uncertainties for example cases

With all the required values and uncertainties summarized in Tables 3.1, 3.2, and 3.4, the uncertainties of the boiling heat flux q and surface temperature T_s can be calculated using Equations (3.14), (3.17), (3.19), and (3.21). Table 3.5 tabulates the heat flux uncertainties δq and surface temperature uncertainties δT_s for Cases 1 to 6.

3.4 Verification

Comparing the heat fluxes estimated following the energy balance method and those calculated following the spatial temperature distribution method can help verify the heat flux calculation. Table 3.6 tabulates the calculated heat fluxes q for Cases 1 to 6 for comparison. The heat fluxes q obtained following these two methods agree well for all the example cases. Moreover, it indicates that the heat flux q calculated following the spatial temperature distribution method features

Table 3.6: Heat fluxes q for Cases 1 to 6 estimated following the energy balance method and those calculated following the spatial temperature distribution method

Case no.	Disc diameter, D (cm)	Heat flux[1], q (W/cm^2)	Heat flux[2], q (W/cm^2)
1	1.0	29 ± 5	28 ± 3
2		79 ± 6	76 ± 5
3	1.5	28 ± 3	26 ± 2
4		77 ± 3	74 ± 4
5	2.0	24 ± 2	23 ± 2
6		79 ± 2	77 ± 4

[1] Heat flux estimated following the energy balance method,

[2] Heat flux calculated following the spatial temperature distribution method.

smaller uncertainty and falls within the range estimated by the energy balance method for most of the cases. Table 3.6 confirms the validity of the heat flux calculation using either of these two methods and shows the advantage of the spatial temperature distribution method.

3.5 Summary

Methods of calculating the boiling heat flux q and corresponding surface temperature T_s were developed, exemplified, and verified. Besides, the uncertainties in the calculated heat flux q and surface temperature T_s were also analyzed. Following the spatial temperature distribution method, the heat flux q and surface temperature T_s were calculated using the measured temperatures T_1, T_2, and T_3 at each steady state. The boiling heat transfer data under each experimental configuration are tabulated along with their uncertainties in Appendix C.

CHAPTER 4

Nucleate boiling heat flux

This chapter presents the boiling heat transfer data obtained on plain surfaces under different experimental configurations and discusses the effects of heater size, contact angle, and surrounding vessel size on nucleate boiling heat flux for small horizontal surfaces. Prior to that, the background of nucleate boiling and the parametric effects are introduced.

4.1 Background

4.1.1 Nucleate boiling

The ONB is marked by a sudden increase in the slope of a boiling curve, as shown in Figure 1.1. With increasing surface superheat, the vaporization becomes more rapid due to more active nucleation sites and higher bubble generation rate at each site, which contributes to the enhancement in heat flux along with the associated violent disturbance of the thermal layer and mixing of the liquid [24]. The heat transfer process varies spatially and temporally, and the evaluation is further complicated by the interference and coalescence of bubbles in lateral and vertical directions. Owing to the complexity of the nucleate boiling process, only a few mechanistic models have been developed to predict the heat flux as a function of surface superheat and still rely on several empirical correlations [21]. Instead of capturing the real process, the most widely used correlation for predicting the

heat flux q at a given surface superheat ΔT_s was developed by Rohsenow [80] based on dimensional analysis and expressed as

$$q = \mu_l h_{fg} \left[\frac{g\left(\rho_l - \rho_v\right)}{\sigma} \right]^{1/2} \left(\frac{c_{p,l} \Delta T_s}{C_{sf} h_{fg} \mathrm{Pr}_l{}^n} \right)^3. \tag{4.1}$$

Here, μ_l, ρ_l, $c_{p,l}$, and Pr_l are the dynamic viscosity, density, specific heat capacity, and Prandtl number of liquid, respectively, g is the gravitational acceleration, and all properties are evaluated at the saturation temperature. The correlating constant C_{sf} depends on the surface-liquid combination, and the exponent n has a value of 1 for water and 1.7 for other liquids. For water boiled on polished and scored copper surfaces, the value of C_{sf} approximates 0.0128 and 0.0068, respectively. Though without considering bubble interaction, Rohsenow's correlation has been recognized to work for both partial and fully developed nucleate boiling. Parametric effects on nucleate boiling can be reflected on the boiling curve graphically and on the value of C_{sf} quantitatively.

4.1.2 Parametric effects

The first study of heater size effect on nucleate boiling was carried out on horizontal wires and dates back to half a century ago. When the heater size becomes close to the bubble departure diameter, its impact on nucleate boiling manifests [81,82]. The bubble departure diameters measured experimentally or calculated from the correlations proposed by different researchers differ due to the complex situation of dynamic measurement as well as its dependence on surface characteristics [83–85], whereas it is generally scaled with respect to the capillary length l, i.e.,

$$l = \sqrt{\frac{\sigma}{g\left(\rho_l - \rho_v\right)}}. \tag{4.2}$$

For saturated water at one-atmosphere pressure, $l = 0.25$ cm. It roughly captures the force balance on a bubble about to depart by relating surface tension and buoyancy. Usually, the "heater size" means the characteristic length L_c that is

the width of a square heater or the diameter of a circular heater. Therefore, the dimensionless length L_c/l, namely, the ratio of heater size L_c to capillary length l, has been widely adopted in studies to represent the relative scale of boiling.

Bakhru and Lienhard [81] found that nucleate boiling regime vanished when boiling various saturated liquids using horizontal platinum wires of dimensionless radii R' ($R' = R/l$) from 0.0076 to 0.0806. In their study, the primary bubbles wrapped around the thin wires before growing large enough to depart, and vapor patches associated with boiling curves of monotonic increases were observed as a result. Conventional boiling curve began to reestablish when the dimensionless radius R' increased to 0.1. Right after that, Baker [86] reported the boiling characteristics of R-113 on vertical flat TaN surfaces of areas from 0.0106 to 2.00 cm^2, and both the saturated and subcooled boiling curves exhibited pronounced continuous left shift with decreasing heater size. He attributed the enhanced nucleate boiling and increase in CHF to the leading edge and side flow effects, which was later challenged by Park and Bergles [87] who boiled saturated R-113 on vertical flat surfaces of different materials in 5- to 60-mm width and 5- or 10-mm height. In their study, the boiling curve was insensitive to the heater size, while the CHF increased as the heater width or height decreased. By boiling subcooled FC-72 on horizontal quartz wafers in square areas 0.65, 2.62, and 7.29 mm^2 in low and high gravities ($0.01g$ and $1.7g$), respectively, Henry and Kim [88] also reported boiling curves without nucleate boiling regime with the 0.65-mm^2 heating area in low gravity. In high gravity, the 0.65-mm^2 heating area featured lower heat flux in nucleate boiling regime. The threshold value of L_c/l above which nucleate boiling is conventional (buoyancy dominated) was later determined by Raj and Kim [82] to be 2.1 by boiling subcooled FC-72 and pentane on horizontal quartz wafers.

The direct dependence of nucleate boiling on surface wettability was first explored by Harrison and Levine [89] who boiled saturated stearic acid on horizon-

tal flat 100 and 110 copper crystal planes at about 2.3 kPa. At a given surface superheat, the more wetted surface (110) featured higher heat flux in natural convection regime but lower heat flux in nucleate boiling regime. They qualitatively attributed the outcomes to a smaller thermal resistance of the more wetted interface in natural convection regime and the more difficult ebullition on the more wetted surface when nucleation occurred, respectively. Liaw and Dhir [90] systematically investigated the contact angle effect by boiling saturated water on a vertical flat copper surface of width 6.3 cm and height 10.3 cm. They found that the boiling curve shifted to the right with decreasing contact angle, while the trend of heat flux against surface superheat remained the same, which Girard *et al.* [91] also found by boiling saturated water on horizontal flat 1 cm $\times$ 1 cm copper surfaces. Besides, both studies showed that the CHF increased as the contact angle was decreased. However, in contrast to the boiling curves reported by Harrison and Levine, the natural convection regimes for different contact angles showed no apparent difference in the studies by Liaw and Dhir and Girard.

Much more previous works focused on the role of contact angle in nucleation and bubble dynamics during boiling, as discussed in Chapter 1. An augmented version of Mikic and Rohsenow's model [36] developed by Judd and Hwang [92] incorporated the mechanisms of natural convection, nucleate boiling, and microlayer evaporation at bubble bases. With the help of several empirical correlations and assumptions, they correlated the nucleate boiling heat flux to the number density of active nucleation sites, bubble departure diameter, and bubble release frequency, which are all governed by the contact angle. The nucleate boiling heat flux at a given surface superheat is thus different for different contact angles, and so is the heat transfer coefficient. With increasing surface superheat, nucleate boiling becomes fully developed as the primary bubbles merge into larger mushroom bubbles before leaving the surface. The heat transfer is then dominated by the

vaporization of micro/macrolayers surrounding the vapor stems and thus depends on the surface void fraction and stem geometry, both of which are also affected by the contact angle, as experimentally revealed and numerically interpreted by Dhir and Liaw [93].

It should be stressed that boiling experiments performed on small horizontal surfaces recently were usually not enclosed by vertical sidewalls but in large liquid-holding vessels. Unlike the negligible container effect on large heaters, the container effect becomes noticeable with decreasing heater size [94]. However, the effect of surrounding vessel size on nucleate boiling did not receive enough attention even though it has been experimentally proved to affect CHF. Costello *et al.* [94], Lienhard and Keeling [95], Elkassabgi and Lienhard [96], and Bockwoldt *et al.* [97] found that enlarging surrounding vessel induced side flow during boiling. The enhancement in CHF was attributed to the induced convention in their studies, while the effect on nucleate boiling or heat transfer coefficient was not discussed.

4.2 Results and discussion

Boiling curves for discs of diameters $D = 1.0$, 1.5, and 2.0 cm were obtained for different contact angles θ and surrounding vessel diameters D_T. A systematic study investigating the effects of heater size, contact angle, and surrounding vessel size on nucleate boiling heat flux was carried out by comparing the measured boiling curves in terms of each parameter. Besides, Rohsenow's correlation, i.e., Equation (4.1), was applied to fit the nucleate boiling heat transfer data to assess the parametric effects on the correlating constant C_{sf}.

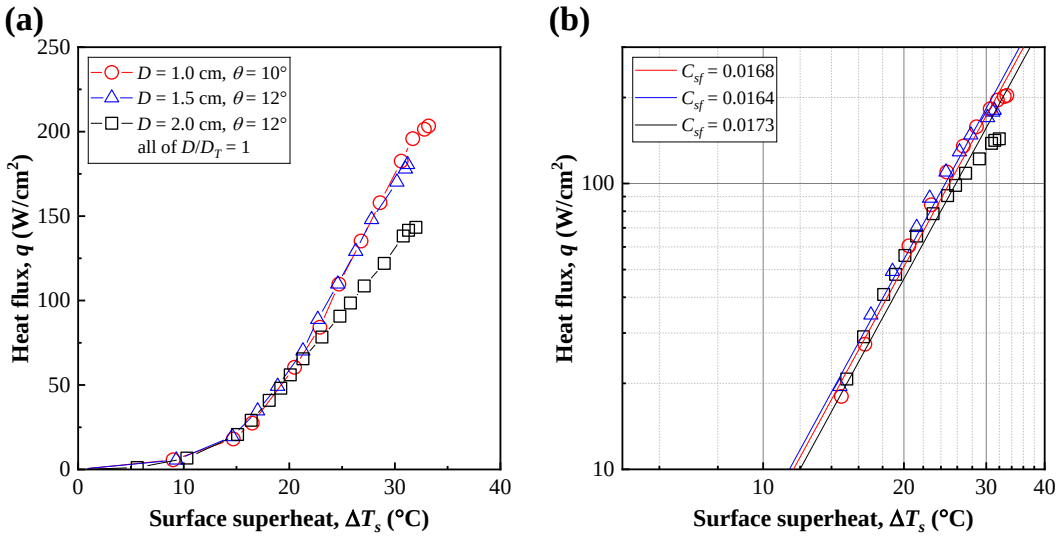

Figure 4.1: Boiling curves for the discs of diameters $D = 1.0$, 1.5, and 2.0 cm with contact angle $\theta \approx 10°$

4.2.1 Heater size effect

Figure 4.1 shows the boiling curves measured for the discs of diameters $D = 1.0$, 1.5, and 2.0 cm with contact angle $\theta \approx 10°$ when the surrounding vessel diameter D_T was equal to the disc diameter D, i.e., $D/D_T = 1$. As the surface superheat increases, the heat flux first increases slowly as in natural convection regime, then rises sharply as into nucleate boiling regime, and finally develops gently until CHF is reached. As shown in Figure 4.1 (a), the boiling curves for different disc diameters show no prominent difference in natural convection regime and a large part of nucleate boiling regime. However, in approach to CHF, the 1.0- and 1.5-cm-diameter discs feature heat fluxes higher than that on the 2.0-cm-diameter disc, and the CHF increases from 143 to 181 and to 203 W/cm^2 as the disc diameter D decreases from 2.0 to 1.5 and to 1.0 cm. Figure 4.1 (b) shows the boiling curves on a logarithmic scale, and Rhosenow's correlation is plotted to fit each boiling curve to assess the heater size effect. As shown in Figure 4.1 (b),

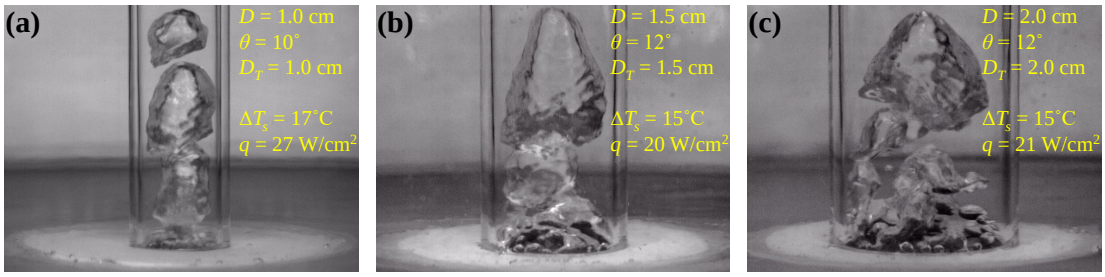

Figure 4.2: Photographs of nucleate boiling near $q = 20$ W/cm^2 on the discs of diameters (a) $D = 1.0$ cm, (b) $D = 1.5$ cm, and (c) $D = 2.0$ cm with contact angle $\theta \approx 10°$

a common linear trend is formed by the boiling heat transfer data for different disc diameters, and the corresponding fit lines are close. The values of C_{sf} are 0.0168, 0.0164, and 0.0173 for the discs of diameters $D = 1.0$, 1.5, and 2.0 cm, respectively, and feature differences less than 5 %, which is within the uncertainty of data.

Figure 4.2 shows the photographs of nucleate boiling near $q = 20$ W/cm^2 on the discs of diameters (a) $D = 1.0$ cm, (b) $D = 1.5$ cm, and (c) $D = 2.0$ cm with contact angle $\theta \approx 10°$. As shown in Figure 4.2, at similar surface superheats ΔT_s, the discs feature similar heat fluxes q, and the generated vapor departs in similar patterns from the surface despite the different heater sizes.

Figure 4.1 establishes that heater size hardly affects boiling curve but CHF. As a result, the boiling heat transfer coefficient (HTC) is also independent of heater size, as shown in Figure 4.3. It also agrees with the result by Kwark *et al.* [98]. They also found that the boiling curve was insensitive to heater size by boiling saturated water on horizontal square plain and Al_2O_3-nanoparticles copper surfaces of side lengths 0.75, 1, 1.5, and 2 cm that were not surrounded by enclosing sidewalls. These outcomes are as expected since, under a given condition, nucleate boiling heat transfer is governed by the number density of

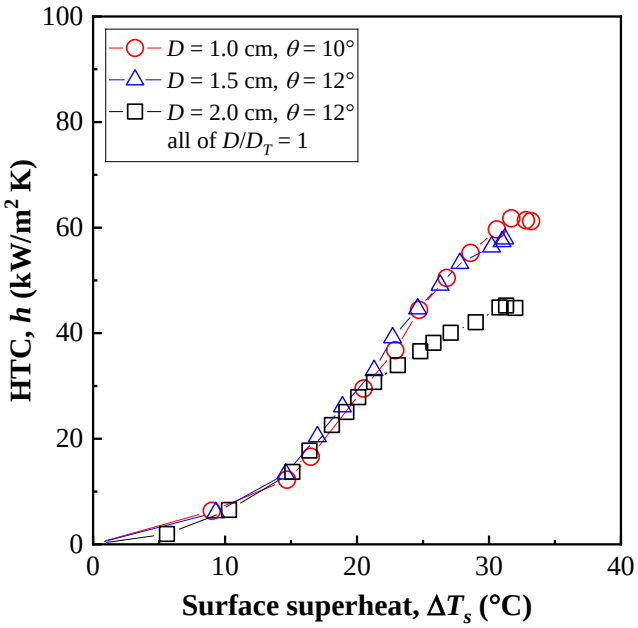

Figure 4.3: HTC as a function of surface superheat ΔT_s for the discs of diameters $D = 1.0$, 1.5, and 2.0 cm with contact angle $\theta \approx 10°$

active nucleation sites, bubble departure diameter, and bubble release frequency [36, 92]. These parameters are determined by heater surface characteristics, e.g., temperature, finish, wettability, geometry, and orientation, but not heater size when the heater size is much greater than the primary bubble size, as discussed in Chapter 1. When approaching CHF, however, the vapor removal pattern is then governed by hydrodynamics in addition to the surface characteristics. The CHF differs for different heater sizes as a result.

4.2.2 Contact angle effect

Figure 4.4 shows the boiling curves measured for the discs of diameters (a-b) $D =$ 1.0 cm, (c-d) $D = 1.5$ cm, and (e-f) $D = 2.0$ cm with contact angles θ from about 10 to 80°. For all the cases, the surrounding vessel diameter D_T was equal to the disc

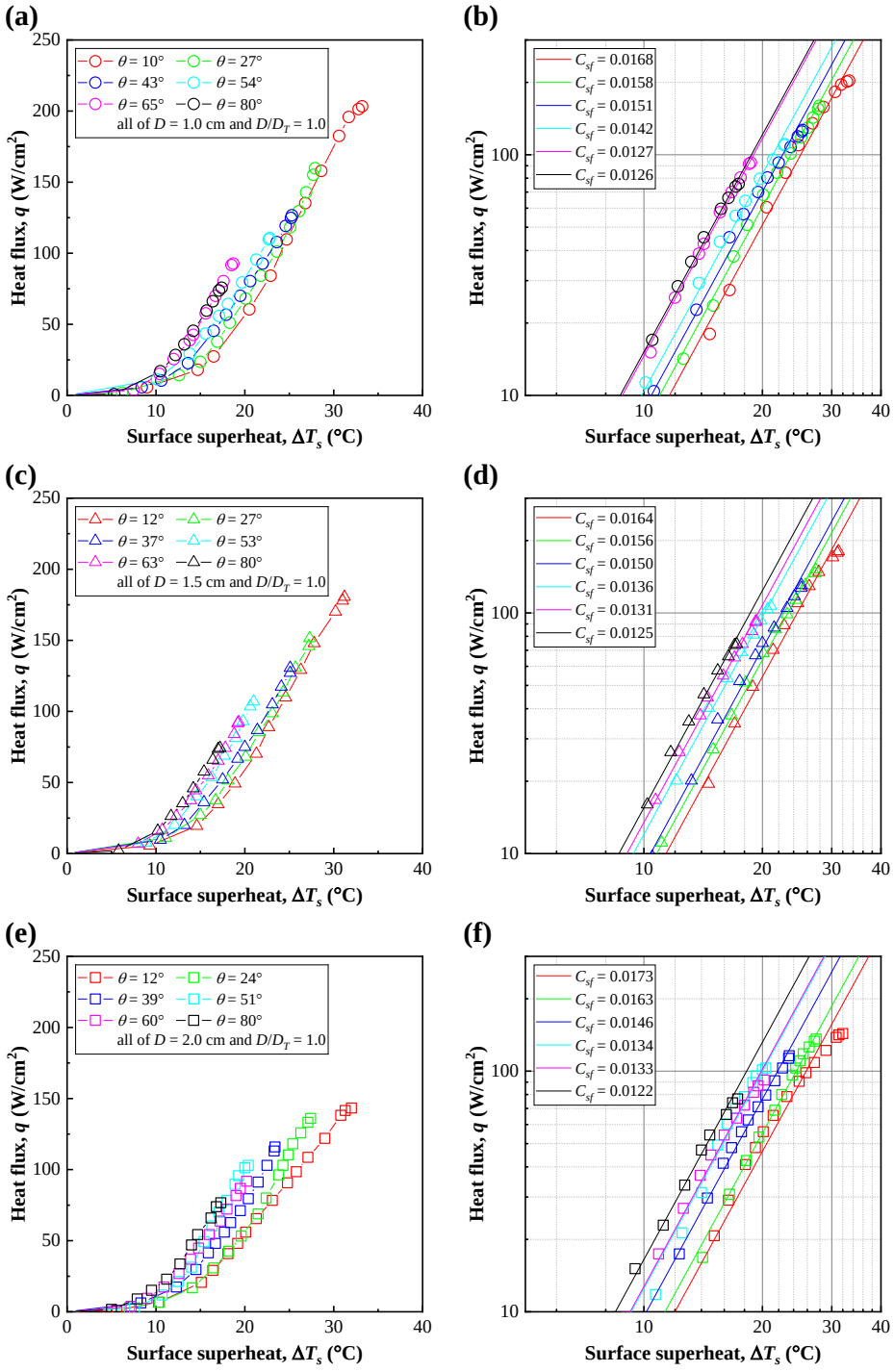

Figure 4.4: Boiling curves for the discs of diameters (a-b) $D = 1.0$ cm, (c-d) $D = 1.5$ cm, and (e-f) $D = 2.0$ cm with different contact angles θ. For all the cases, the ratio of heater size to surrounding vessel size D/D_T is 1.

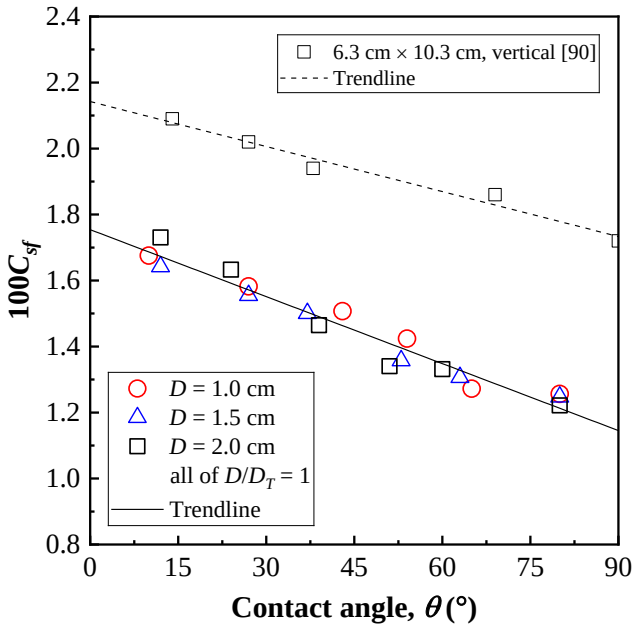

Figure 4.5: Correlating constant of Rohsenow's correlation C_{sf} as a function of contact angle θ

diameter D, i.e., $D/D_T = 1$. In each figure, the boiling curve monotonically shifts to the left with decreasing CHF as the contact angle increases. For instance, as shown in Figure 4.4 (c), at surface superheat $\Delta T_s = 17°\text{C}$, the heat flux q is about 35 W/cm^2 on the 1.5-cm-diameter disc of contact angle $\theta = 12°$ and increases to about 74 W/cm^2 as the contact angle θ increases to 80° where CHF is reached. The former disc of contact angle $\theta = 12°$ reaches CHF of 181 W/cm^2 at surface superheat $\Delta T_s = 31°\text{C}$.

Figures 4.4 (b), (d), and (f) show the boiling curves on logarithmic scales, and Rhosenow's correlation is plotted to fit each boiling curve. In each figure, the linear trends formed by the boiling heat transfer data are consistent among the discs of different contact angles, and the corresponding fit lines are thus parallel to each other only with different values of C_{sf}. C_{sf} decreases monotonically with

increasing contact angle, as shown in Figure 4.5 which shows the value of C_{sf} as a function of contact angle. For instance, it decreases by about 24 % from 0.0164 to 0.0125 as the contact angle increases from 12 to 80° for the 1.5-cm-diameter disc. Figure 4.5 also indicates that C_{sf} is hardly dependent on heater size for a given contact angle. Values of C_{sf} reported by Liaw and Dhir [90] are also added in Figure 4.5 for comparison. Even though their values of C_{sf} are greater than those obtained in this study, both studies indicate that C_{sf} decreases as the contact angle increases. The difference in values of C_{sf} at a given contact angle might result from different surface orientations as Liaw and Dhir boiled water on a vertical flat copper surface.

Figures 4.6 to 4.8 in order show the photographs of nucleate boiling near q = 20 W/cm^2 on the discs of diameters D = 1.0, 1.5, and 2.0 cm with different contact angles θ, respectively. In each figure, as the contact angle increases, the trend shows as either increasing heat flux q or decreasing surface superheat ΔT_s with another nearly unchanged.

Figure 4.4 establishes that a less wetted surface features (i) earlier ONB, (ii) higher heat flux in nucleate boiling regime, but (iii) lower CHF. As one of the results, the HTC is also greater on the less wetted surface at a given surface superheat, as shown in Figure 4.9. Besides, the consistent trends in Figure 4.4 indicate that the dependence of heat flux on surface superheat in nucleate boiling regime remains the same for different contact angles, which agrees with the experimental findings by Liaw and Dhir [90] and Girard *et al.* [91]. The earlier ONB can be mathematically explained with Equation (1.13) developed by Hsu [32]. As shown in Figure 1.2, graphically, the curve representing Equation (1.11) will move downward if the contact angle increases, thus reducing the minimum surface superheat required for nucleation. In addition, it also broadens the size range of cavities that can nucleate. Thus, more nucleation sites will be activated at a given

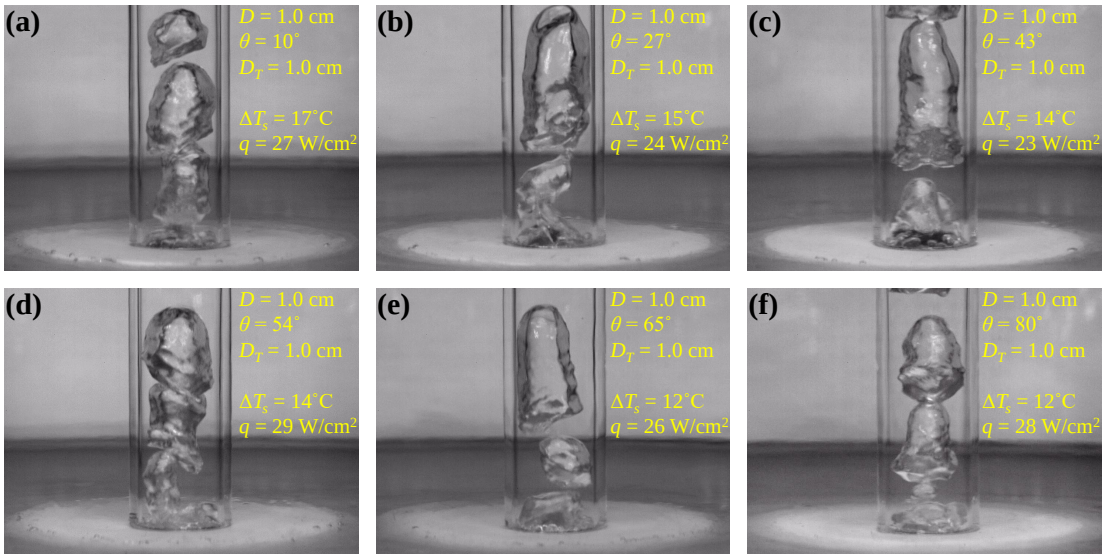

Figure 4.6: Photographs of nucleate boiling near $q = 20$ W/cm^2 on the 1.0-cm-diameter disc of contact angles (a) $\theta = 10°$, (b) $\theta = 27°$, (c) $\theta = 43°$, (d) $\theta = 54°$, (e) $\theta = 65°$, and (f) $\theta = 80°$

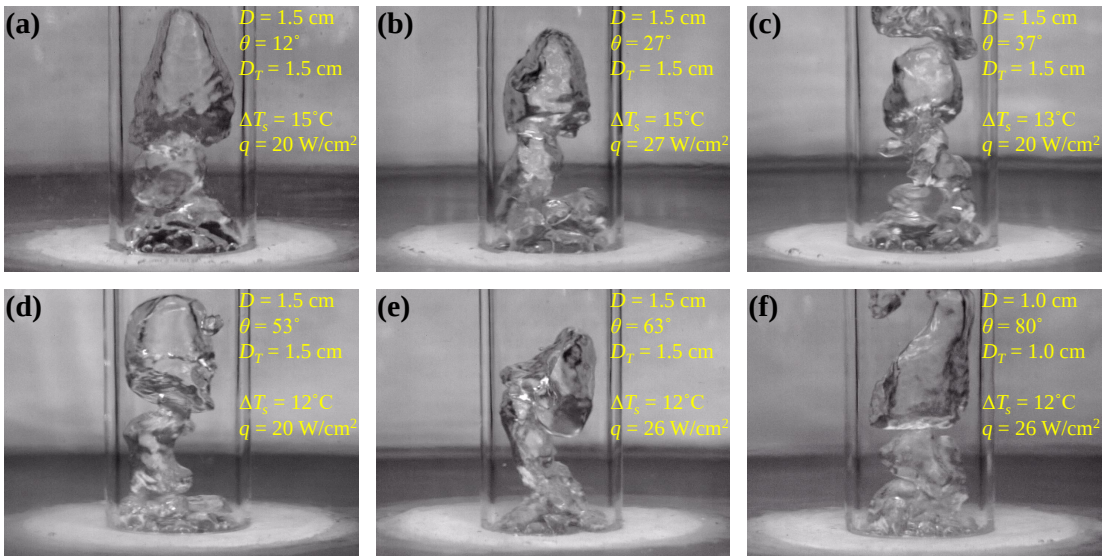

Figure 4.7: Photographs of nucleate boiling near $q = 20$ W/cm^2 on the 1.5-cm-diameter disc of contact angles (a) $\theta = 12°$, (b) $\theta = 27°$, (c) $\theta = 37°$, (d) $\theta = 53°$, (e) $\theta = 63°$, and (f) $\theta = 80°$

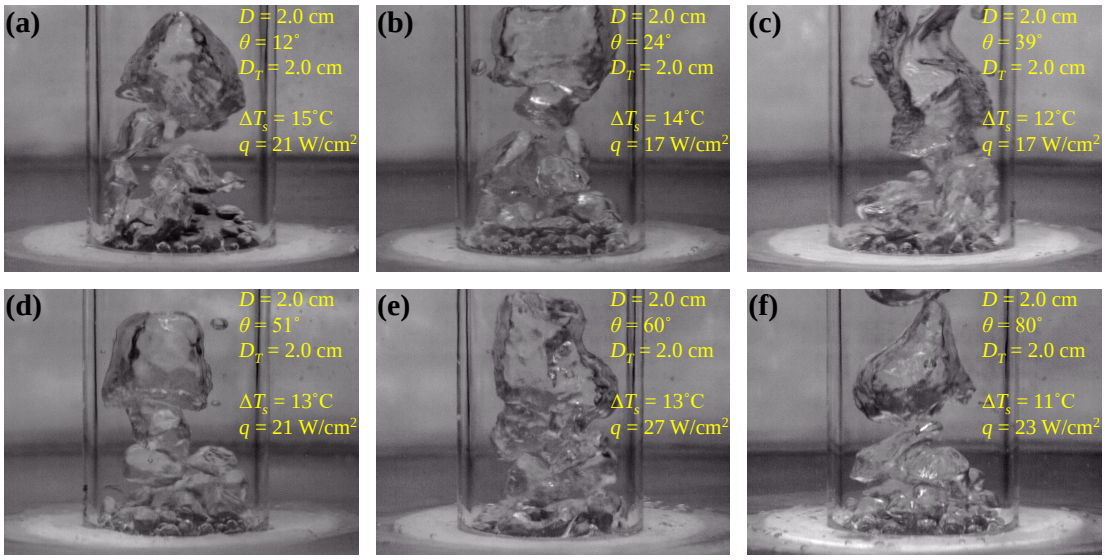

Figure 4.8: Photographs of nucleate boiling near $q = 20$ W/cm^2 on the 2.0-cm-diameter disc of contact angles (a) $\theta = 12°$, (b) $\theta = 24°$, (c) $\theta = 39°$, (d) $\theta = 51°$, (e) $\theta = 60°$, and (f) $\theta = 80°$

surface superheat, which is also mathematically captured in Equation (1.24) by Wang and Dhir [41] and Equation (1.25) by Basu *et al.* [45], respectively. The increasing number density of nucleation sites contributes to a higher vapor generation rate, thus making the less wetted surface feature higher heat flux at a given surface superheat.

As approaching CHF, the nucleate boiling becomes fully developed. The heat transfer then relies on the vaporization of micro/macrolayers surrounding the vapor stems standing on the surface as the thermal layer becomes quite thin ($\sim 10^{-5}$ m) compared to the stem diameter and height [93]. Dhir and Liaw [93] argued that at the same surface void fraction, the heat flux and HTC on more wetted surfaces are higher due to the smaller thermal resistance of less liquid between the surface and stems. Therefore, when a less wetted surface reaches CHF, the corresponding void fraction on a more wetted surface is still small,

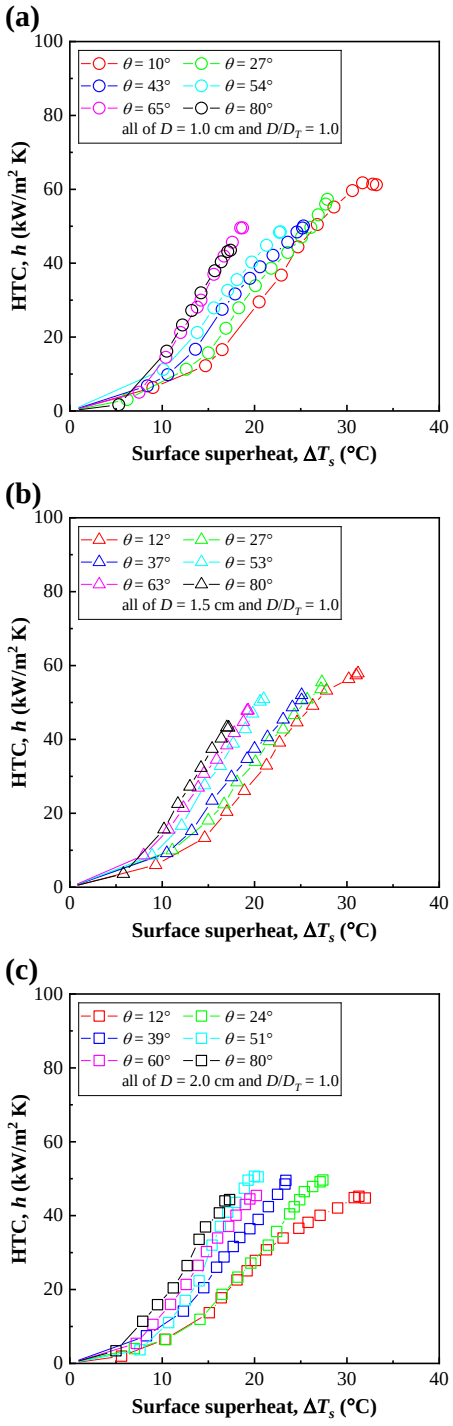

Figure 4.9: HTC as a function of surface superheat ΔT_s for the discs of diameters (a) $D = 1.0$ cm, (b) $D = 1.5$ cm, and (c) $D = 2.0$ cm with different contact angles θ

thus allowing further development of nucleate boiling and delaying CHF. For well wetted surfaces, CHF is determined by the vapor removal limit rather than the vapor production limit that sets CHF for partially wetted surfaces.

4.2.3 Surrounding vessel size effect

Figure 4.10 shows the boiling curves measured for the discs of diameters (a-b) $D = 1.0$ cm, (c-d) $D = 1.5$ cm, and (e-f) $D = 2.0$ cm surrounded by vessels of different diameters D_T. For all the cases, the disc was well wetted, i.e., $\theta \approx 10^\circ$. In each figure, the boiling curves for different vessel diameters show no prominent difference at low heat fluxes but slightly diverge at high heat fluxes. The divergence seems to be independent of the vessel diameter as the larger vessel does not always guarantee a higher or lower heat flux at a given surface superheat, as shown in Figures 4.10 (a), (c), and (e). Thus, it is considered to be a result of the increasing uncertainty in surface superheat at higher heat fluxes. However, the CHF monotonically increases when the surrounding vessel is enlarged. For instance, as shown in Figure 4.10 (c), the CHF increases from 181 to 218 W/cm^2 for the well wetted 1.5-cm-diameter disc when the vessel diameter D_T increases from 1.5 to 20.0 cm. Figures 4.10 (b), (d), and (f) show the boiling curves on logarithmic scales, and Rhosenow's correlation is plotted to fit each boiling curve. In each figure, a common linear trend is formed by the boiling heat transfer data for different vessel diameters, and the corresponding fit lines are close. For instance, the values of C_{sf} are 0.0164, 0.0161, 0.0163, and 0.0173 for the 1.5-cm-diameter disc surrounded by vessels of diameters $D_T = 1.5$, 3.0, 7.5, and 20.0 cm, respectively, and feature differences less than 7 %.

Figures 4.11 to 4.13 in order show the photographs of nucleate boiling near $q = 20$ W/cm^2 on the discs of diameters $D = 1.0$, 1.5, and 2.0 cm surrounded by vessels of different diameters D_T, respectively. In each figure, even though

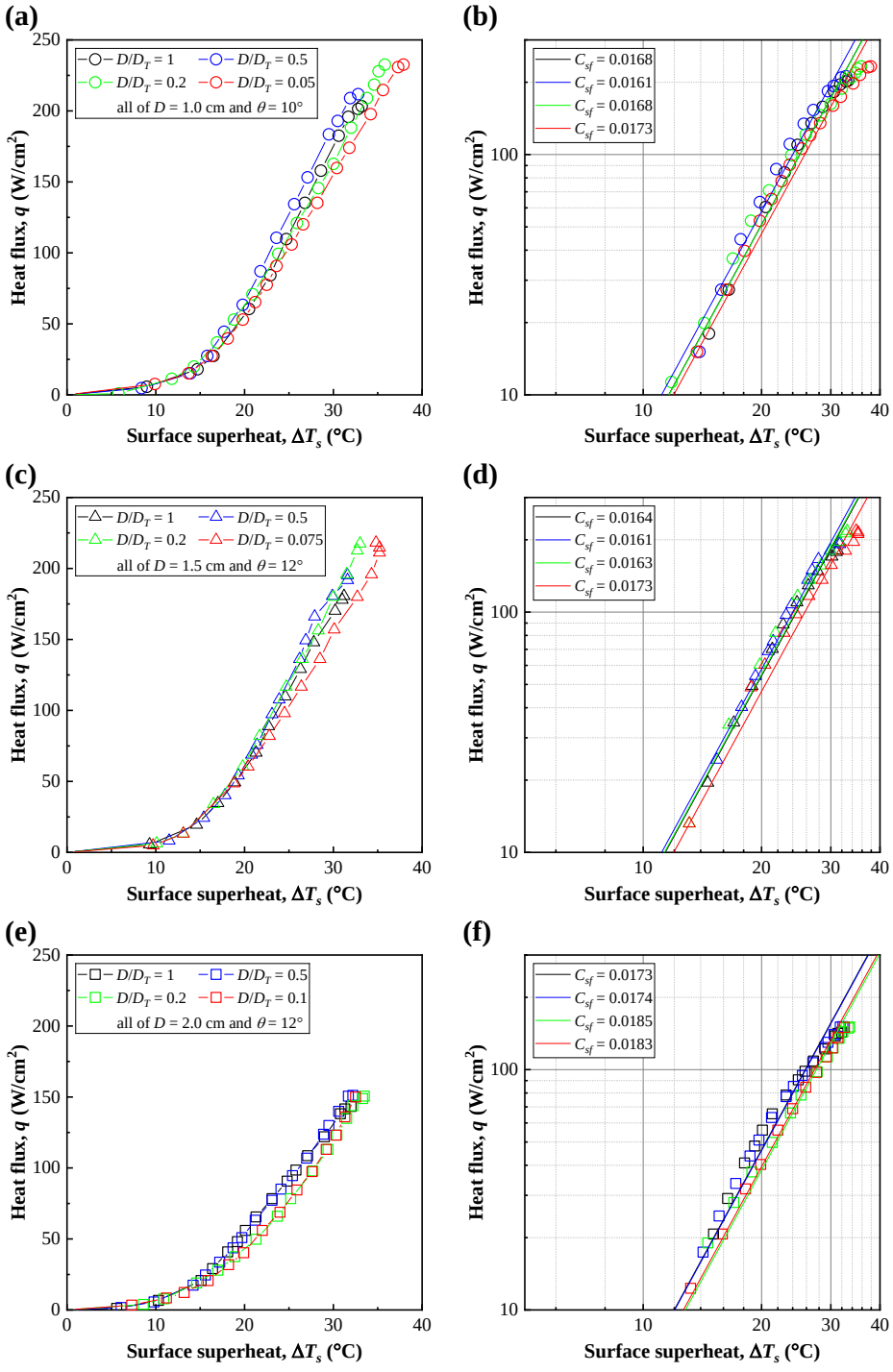

Figure 4.10: Boiling curves for the discs of diameters (a-b) D = 1.0 cm, (c-d) D = 1.5 cm, and (e-f) D = 2.0 cm surrounded by vessels of different diameters D_T. For all the cases, the contact angle θ is about 10°.

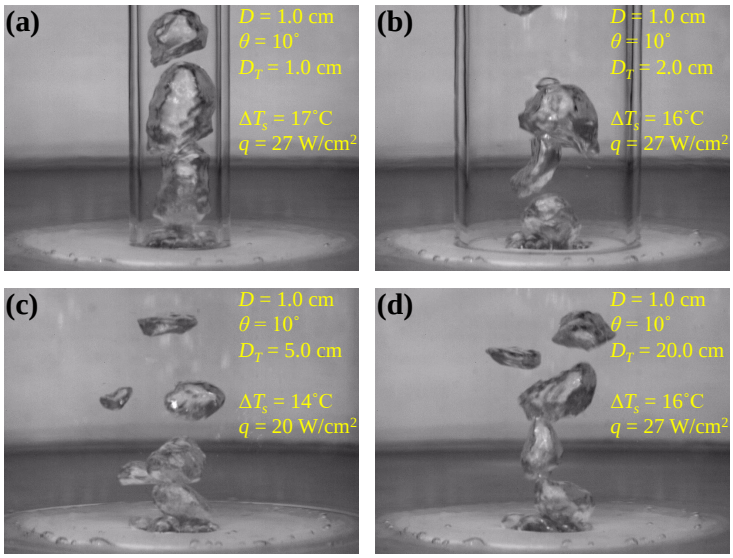

Figure 4.11: Photographs of nucleate boiling near $q = 20$ W/cm^2 on the 1.0-cm-diameter disc surrounded by vessels of diameters (a) $D_T = 1.0$ cm, (b) $D_T = 2.0$ cm, (c) $D_T = 5.0$ cm, and (d) $D_T = 20.0$ cm

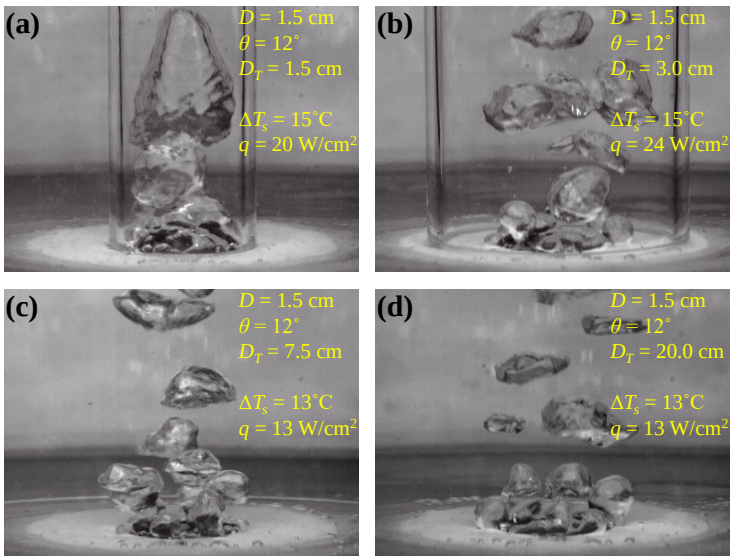

Figure 4.12: Photographs of nucleate boiling near $q = 20$ W/cm^2 on the 1.5-cm-diameter disc surrounded by vessels of diameters (a) $D_T = 1.5$ cm, (b) $D_T = 3.0$ cm, (c) $D_T = 7.5$ cm, and (d) $D_T = 20.0$ cm

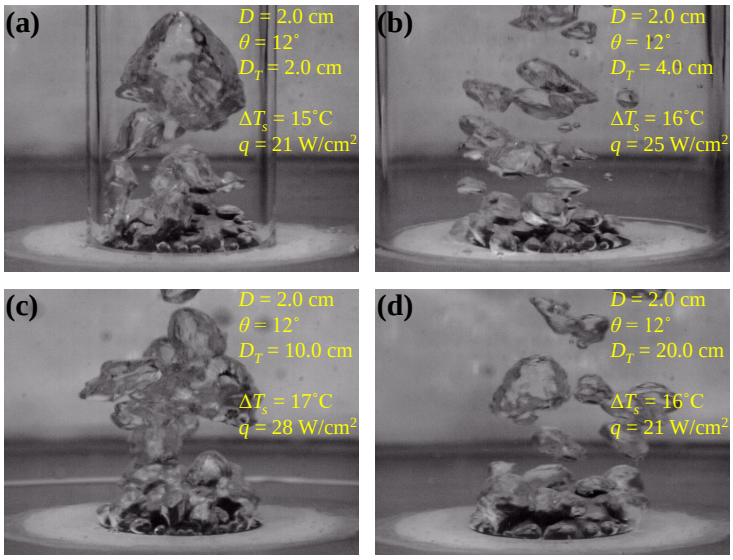

Figure 4.13: Photographs of nucleate boiling near $q = 20$ W/cm^2 on the 2.0-cm-diameter disc surrounded by vessels of diameters (a) $D_T = 2.0$ cm, (b) $D_T = 4.0$ cm, (c) $D_T = 10.0$ cm, and (d) $D_T = 20.0$ cm

the generated vapor in the form of bubbles departs more dispersedly with the surrounding vessel enlarged, the disc still features similar heat fluxes q when the surface superheats ΔT_s are similar.

Figure 4.10 establishes that surrounding vessel size hardly affects boiling curve at low heat fluxes but at high heat fluxes up to CHF. As a result, the HTC is also independent of surrounding vessel size in the regime of low heat flux, as shown in Figure 4.14. It can be attributed to the fact that the nucleate boiling heat transfer far from critical condition relies much greater on the vapor generation rate that is determined by heater surface characteristics than the convective effect near the path boundary of vapor departure. In the regime of high heat flux, even though the boiling curves in Figure 4.10 show no monotonic change due to the uncertainty in surface superheat. However, the heat flux is expected to be higher when the surrounding vessel is enlarged as the induced convection resulting from

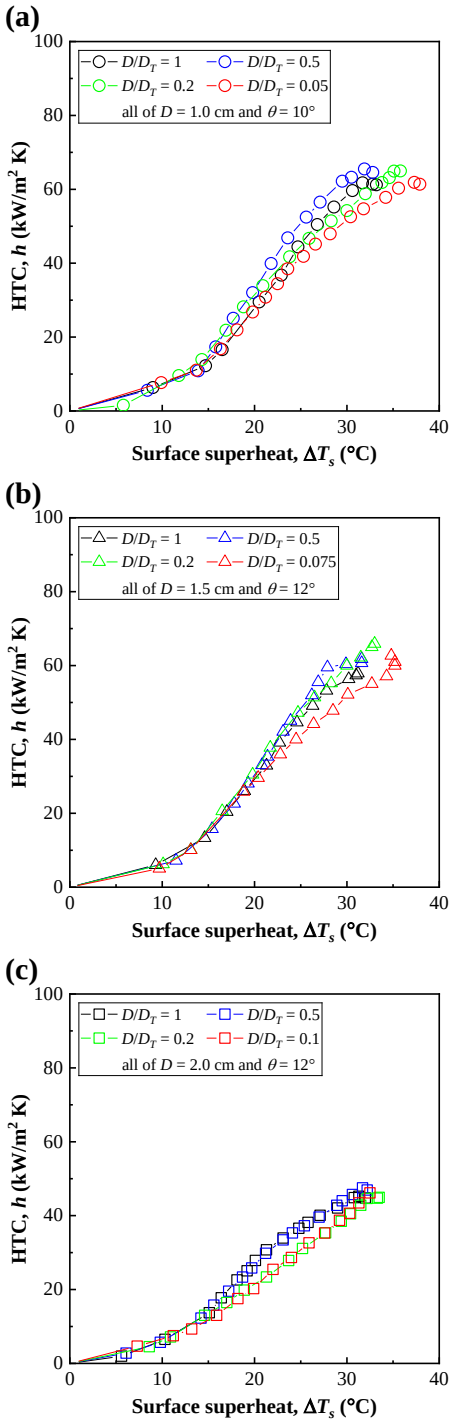

Figure 4.14: HTC as a function of surface superheat ΔT_s for the discs of diameters (a) $D = 1.0$ cm, (b) $D = 1.5$ cm, and (c) $D = 2.0$ cm surrounded by vessels of different diameters D_T

the violent vapor removal is stronger. The surrounding vessel size, as expected, plays a role near critical condition where the maximum vapor removal rate allowed from the surface is affected by the path boundary, thus changing the CHF. The HTC is different as well.

4.3 Summary

The findings of this chapter are summarized as that (i) heater size does not affect boiling curve when the heater size is much greater than the primary bubble size/capillary length, (ii) boiling curve shifts to the left with increasing contact angle, but the trend of heat flux against surface superheat remains the same, and (iii) surrounding vessel size does not affect boiling curve at low heat fluxes. The parametric effects of heater size, contact angle, and surrounding vessel size on critical heat flux are detailed in the next chapter.

CHAPTER 5

Critical heat flux

This chapter presents the CHF data obtained on plain surfaces under different experimental configurations and discusses the effects of heater size, contact angle, and surrounding vessel size on CHF for small horizontal surfaces. Prior to that, the hydrodynamic theory of CHF and the parametric effects are introduced.

5.1 Background

5.1.1 Hydrodynamic theory

As shown in Figure 5.1, the pool boiling heat transfer occurring near critical condition on horizontal flat heaters that are well wetted can be classified into three categories depending on the vapor removal pattern. Figure 5.1 (a) illustrates the vapor removal pattern at CHF for pool boiling on infinite horizontal flat plates as proposed by Zuber [99]. In Zuber's model, near critical condition, the vapor generated on horizontal flat heaters escapes in the form of jets. These vapor jets were assumed to locate on a square grid with spacings of two-dimensional Taylor unstable wavelength. Zuber could not provide a basis for selecting either the critical Taylor wavelength

$$\lambda_c = 2\pi \sqrt{\frac{\sigma}{(\rho_l - \rho_v)\, g}} \tag{5.1}$$

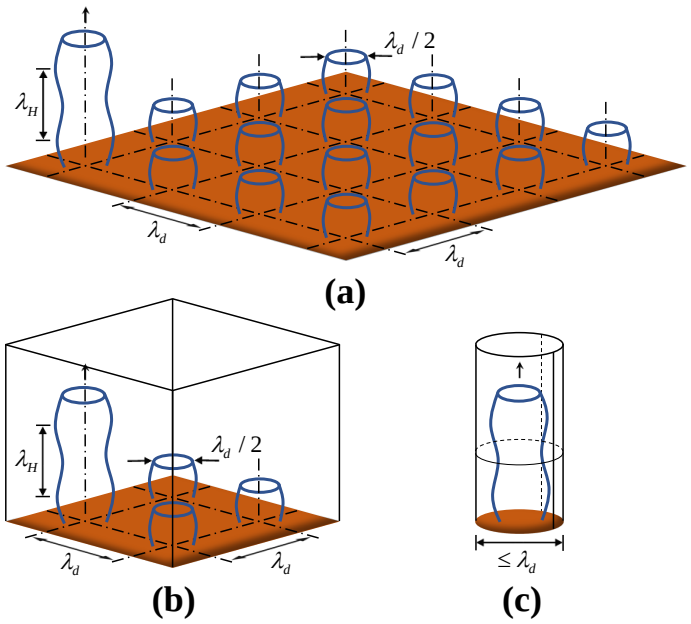

Figure 5.1: Vapor removal pattern at CHF for pool boiling on (a) infinite horizontal flat plates, (b) small horizontal flat plate heaters of sizes between λ_d and $3\lambda_d$, and (c) those of diameters less than λ_d surrounded by enclosing sidewalls

or the "most dangerous" Taylor wavelength

$$\lambda_d = 2\pi\sqrt{3}\sqrt{\frac{\sigma}{(\rho_l - \rho_v)\, g}}. \tag{5.2}$$

For saturated water at one-atmosphere pressure, $\lambda_c = 1.57$ cm and $\lambda_d = 2.72$ cm. The diameters of the vapor jets were assumed to be equal to half of their spacings. It was proposed that at CHF, the liquid-vapor interface becomes unstable when the relative vapor velocity reaches a critical value determined by the Helmholtz unstable wavelength λ_H. Thus, the instability of the vapor jets represents the maximum possible rate at which vapor can be removed under surface tension and buoyancy. Taking the Helmholtz unstable wavelength λ_H to be equal to the circumference of the vapor jet and using a Taylor unstable wavelength between

λ_c and λ_d, Zuber [99, 100] obtained the corresponding CHF expression as

$$q_{CHF,Z} = \frac{\pi}{24}\rho_v h_{fg}\left[\frac{\sigma\left(\rho_l - \rho_v\right)g}{{\rho_v}^2}\right]^{1/4}. \tag{5.3}$$

For saturated water at one-atmosphere pressure, Equation (5.3) gives $q_{CHF,Z} =$ 110 W/cm^2. Equation (5.3) applies as long as the system pressure is much less than the critical pressure. Zuber's formulation benefited from earlier works of Kutateladze [101–103]. Later, Lienhard and Dhir [104, 105] proposed that the leading constant should be 0.149 instead of $\pi/24$ for large horizontal flat plate heaters by arguing that the liquid-vapor interface would become unstable at a shorter available Taylor wavelength, λ_d, where the spacings of the vapor jets were equal to λ_d as well. With the modified constant, the ratio $q_{CHF}/q_{CHF,Z}$ is 1.14. They also showed that a heater could not be called an infinite flat plate when its size was less than $3\lambda_d$ [106]. Figures 5.1 (b) and (c) show the postulated vapor removal pattern at CHF for pool boiling on small horizontal flat plate heaters of sizes between λ_d and $3\lambda_d$ and those of diameters less than λ_d surrounded by enclosing sidewalls, respectively.

5.1.2 Parametric effects

Lienhard *et al.* [106] investigated the heater size effect on CHF as most heaters in earlier experimental studies could not be called infinite flat plates. Gogonin and Kutateladze [107] boiled ethanol on horizontal flat ribbons of length 150 mm and widths varying from 5 to 50 mm under different pressures. In their study, no size effect was observed on the CHF for the upward-facing pool boiling in a large chamber. In the first-of-its-kind study performed by Lienhard *et al.* [106], a series of experiments were conducted by boiling various liquids on horizontal square and circular flat plate heaters of different sizes. In their study, all the heater surfaces were fully wetted and surrounded by enclosing sidewalls. No prominent heater

size effect was found until the characteristic lengths L_c of the heaters became less than $3\lambda_d$. CHFs approximately 2.0 to 2.5 times Zuber's CHF prediction were obtained from the heaters when their characteristic lengths L_c decreased to $0.5\lambda_d$. They attributed this outcome to the change in the fraction of heater surface area occupied by vapor jet. They argued that the fraction depended on the number of vapor jets that could be accommodated on a heater when its characteristic length L_c was less than $3\lambda_d$. The vapor jet diameter was still assumed to be $0.5\lambda_d$. As such, CHF should then be determined by the actual number of vapor jets N_j that could be accommodated on the heater of surface area A [106], i.e.,

$$\frac{q_{CHF,small}}{q_{CHF,Z}} = \frac{1.14N_j}{A/{\lambda_d}^2}. \tag{5.4}$$

Similar dependences of CHF on heater size have also been found by Saylor [108] and Rainey and You [109] who boiled FC-72 on horizontal flat heaters of different sizes. Equation (5.4) could effectively explain the heater size effect on CHF within the range $\lambda_d \leq L_c \leq 3\lambda_d$, while it could not describe the trend of CHF against heater size when the heater size becomes less than λ_d.

Many experimental studies have been performed to investigate the surface wettability effect on CHF. Generally, the contact angle is employed as an indicator of surface wettability. Berenson [110, 111] investigated the contact angle effect on CHF by boiling n-pentane on a horizontal flat 5.1-cm-diameter copper surface surrounded by a brass tube of inner diameter 5.8 cm. By adding a slight amount of oleic acid into the liquid, the contact angle decreased from 10 to 0°. No obvious contact angle effect was found on the CHF within this narrow contact angle range. Several other studies had shown reductions in CHF with increasing contact angle. Roy Chowdhury and Winterton [77] performed a transient boiling experiment to study the contact angle effect by quenching vertical cylindrical heaters of diameter 18 mm and length 40 mm in water and methanol, respectively. Aluminum and copper specimens with various surface treatments were used. They found that

increasing the contact angle led to decrease in the CHF. The contact angle varied from 102 to 0° in their study, and the variations in contact angle were achieved by etching or anodizing the specimens and aging the surfaces via quenching repeatedly. Later, Liaw and Dhir [90, 112] thoroughly studied the contact angle effect by boiling water on a vertical flat copper surface of width 6.3 cm and height 10.3 cm. The CHF was found to decrease with increasing contact angle based on their steady-state and transient cooling and heating measurements. In their study, the contact angle was decreased by thermally oxidizing the copper surface. A contact angle above 90° was obtained by depositing a thin coating of fluorosilicone sealant on the surface. The measured CHF at a contact angle of 107° was about half of that measured at a contact angle of 14°. Meanwhile, by performing transient boiling of water on a horizontal flat 26.6-mm-diameter copper surface confined by a glass tube, Maracy and Winterton [78] found that the CHF increased with decreasing contact angle for both the heating and cooling runs. In their study, the contact angle was decreased from 75 to 0° through surface aging by increasing the number of experimental runs. Dhir and Liaw [93] argued that while the hydrodynamic theory is based on the maximum vapor removal rate possible from well wetted surfaces under available buoyancy, CHF for partially wetted surfaces is limited by the maximum vapor generation rate that can be achieved on the surface. With increasing contact angle, there is less area available for vaporization of micro/macrolayers surrounding the vapor stems. Thus, the maximum rate at which vapor can be generated before the surface is substantially covered with vapor sets the upper limit of nucleate boiling heat flux on partially wetted surfaces. In contrast, for well wetted surfaces, the wall void fraction is much smaller, and a large fraction of the surface is covered with liquid. In such cases, the upper limit of nucleate boiling heat flux is set by the maximum rate at which vapor generated on the surface can be removed. The vapor removal limit is larger than the

vapor production limit on partially wetted surfaces. Kandlikar [113] postulated that CHF is reached when the force due to the change of evaporation momentum equals the sum of the forces due to surface tension and hydrostatic pressure at the contact line of a bubble on the surface. Based on that hypothesis, he developed a CHF correlation with dynamic receding contact angle θ_{rec} and surface inclination angle from horizontal ϕ taken into account, i.e.,

$$q_{CHF} = \left(\frac{1+\cos\theta_{rec}}{16}\right)\left[\frac{2}{\pi} + \frac{\pi}{4}\left(1+\cos\theta_{rec}\right)\cos\phi\right]^{1/2}\rho_v h_{fg}\left[\frac{\sigma(\rho_l-\rho_v)g}{{\rho_v}^2}\right]^{1/4}. \quad (5.5)$$

It also shows that CHF decreases as the contact angle increases with fixed surface orientation. Similar dependences of CHF on contact angle have also been shown in experimental studies by Chen *et al.* [1], Kwark *et al.* [2], Ahn *et al.* [114], O'Hanley *et al.* [115], and Girard *et al.* [91]. Even though some of these studies mainly focused on pool boiling on structured surfaces, it can still be concluded that CHF decreases with increasing contact angle by comparing the reported CHFs solely for the plain surfaces of different contact angles.

Much less attention has been given to the surrounding sidewall effect on CHF. Costello *et al.* [94] found that a flat ribbon heater, mounted on a slightly wider block, induced strong side flow in their pool boiling experiment. When the side flow was blocked by the sidewall, the CHF was found to be much lower than it was when the side flow was allowed. Moreover, they observed that the CHF increased when the ribbon width was reduced and the side flow was permitted. Lienhard and Keeling [95] boiled various liquids on horizontal nichrome ribbons of length 10.2 cm and widths ranging from 0.1 to 2.5 cm in a chamber of length 17.8 cm, width 9.5 cm, and height 7.6 cm. The CHF was found to increase with decreasing ribbon width. They attributed this enhancement to the stronger induced convection when the heater size was reduced with fixed surrounding sidewall. The surrounding sidewall effect on CHF was further studied by Elkassabgi and Lienhard [96]. They boiled methanol on a horizontal nichrome wire of diameter 0.813 mm and revealed

that enlarging the spacing of the parallel sidewalls from 2 to 12 mm produced an enhancement up to 50 % in the CHF. Later, Bockwoldt *et al.* [97] used a horizontal flat nickel-plated copper surface of diameter 1.5 cm to boil water. The CHF was enhanced by 25 % and reached 227 W/cm^2 by increasing the inner diameter of the surrounding tube from 1.6 to 14.4 cm. Taken together, it is believed that surrounding sidewall spacing can influence CHF for finite heaters. However, it is worth pointing out that the surrounding sidewall effect has been ignored in several earlier and some recent experimental studies [116–120]. Failing to keep the surrounding sidewall spacing or ratio of heater size to surrounding sidewall spacing unchanged among the experiments makes the comparison of results improper.

5.2 Results and discussion

CHF for the discs of diameters D = 1.0, 1.5, and 2.0 cm ($0.37\lambda_d$, $0.55\lambda_d$, and $0.74\lambda_d$) was measured for different contact angles θ and surrounding vessel diameters D_T. A systematic study investigating the effects of heater size, contact angle, and surrounding vessel size on CHF was carried out by comparing the measured CHFs in terms of each parameter. Besides, Zuber's hydrodynamic theory was modified to theoretically calculate the CHF for the well wetted surfaces with the measured vapor jet diameter and dominant wavelength at water-steam interface.

5.2.1 Heater size effect

Figure 5.2 shows the dimensionless CHF measured for the discs of contact angle $\theta \approx 10^\circ$ as a function of heater size nondimensionalized with the two-dimensional "most dangerous" Taylor wavelength L_c/λ_d when the surrounding vessel diameter D_T was equal to the disc diameter D, i.e., $D/D_T = 1$. As the disc diameter D decreases from 2.0 to 1.5 and to 1.0 cm, the CHF increases from 143 to 181 and

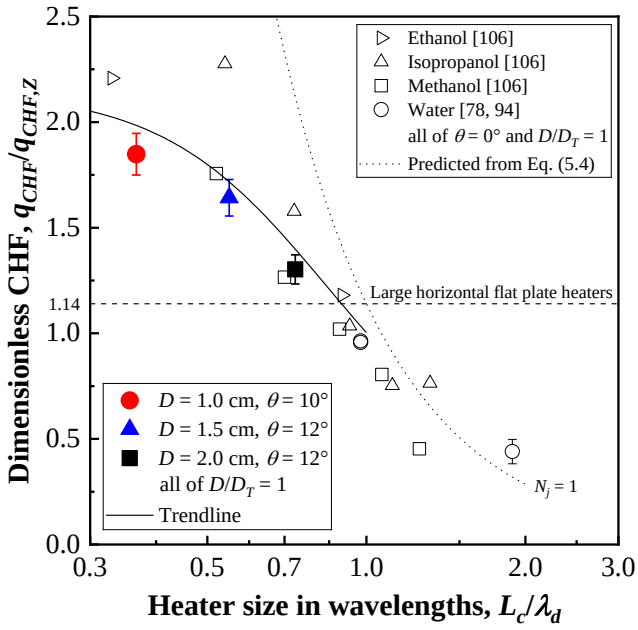

Figure 5.2: Dimensionless CHF as a function of heater size in wavelengths L_c/λ_d for the well wetted discs

to 203 W/cm^2, and the dimensionless CHF, accordingly, increases from 1.30 to 1.64 and to 1.85. For comparison, dimensionless CHFs of various liquids reported by Costello *et al.* [94], Lienhard *et al.* [106], and Maracy and Winterton [78] for fully wetted ($\theta = 0°$) horizontal heaters of different sizes are also given in Figure 5.2. As shown in Figure 5.2, the dependence of dimensionless CHF on heater size in wavelengths L_c/λ_d in this study is comparable to that of cited CHF data. The consistent trend formed by the CHF data collectively confirms that CHF increases with decreasing heater size and is higher than that for an infinite flat plate when the heater size is less than λ_d, i.e., $L_c/\lambda_d < 1$. Prediction from Equation (5.4) proposed by Lienhard *et al.* [106] is also shown as a dotted line in Figure 5.2 with $N_j = 1$. The enhancement in CHF resulting from decreasing heater size when $L_c/\lambda_d \geq 1$ is captured by Equation (5.4). However, when $L_c/\lambda_d < 1$, the observed

CHFs are much less than the prediction with the one-jet model. As the heater size continues to decrease, the fraction of heater surface area occupied by vapor jet increases, allowing a higher fractional vapor removal rate, thereby enhancing the CHF.

Figure 5.3 shows the sequential photographs of boiling near CHF for the discs of diameters (a) $D = 1.0$ cm, (b) $D = 1.5$ cm, and (c) $D = 2.0$ cm with contact angle $\theta \approx 10^{\circ}$ to visualize the corresponding vapor removal pattern. In the past, some had argued about the validity of the assumption of the existence of vapor jets in Zuber's model. Here, a single vapor jet is clearly seen on the disc surface near CHF. Each row of the sequential photographs depicts a complete cycle of one vapor jet forming on the disc surface. From 0 to 100 ms, with a time interval of 20 ms, six photographs in order show the development of the vapor jet. The sequential photographs in Figure 5.3 visually validate the argument by Lienhard *et al.* [106], that is, unlike the vapor removal pattern at CHF for large horizontal flat plate heaters depicted in Zuber's hydrodynamic theory, only one vapor jet exists on heaters of sizes less than the two-dimensional "most dangerous" Taylor wavelength λ_d. Furthermore, it is also observed that the vapor jet size, confined by the surrounding vessel, decreases with decreasing heater size.

The dimensionless CHF for each disc can be calculated based on the hydrodynamic theory using the actual vapor jet diameter that was directly measured from the photographs taken when the vapor jet was fully developed. For the discs of diameters $D = 1.0$, 1.5, and 2.0 cm, the measured jet diameters ranged from 0.65 to 0.87 cm, 0.87 to 1.37 cm, and 1.05 to 1.55 cm, respectively, the corresponding average jet diameters D_v were 0.76, 1.12, and 1.30 cm. It is worth noting that the vapor jet diameter $D_v = 1.30$ cm observed on the 2.0-cm-diameter disc of $D/\lambda_d = 0.74$ is still about half of the two-dimensional "most dangerous" Taylor wavelength $\lambda_d = 2.72$ cm. The critical relative velocity for a plane interface

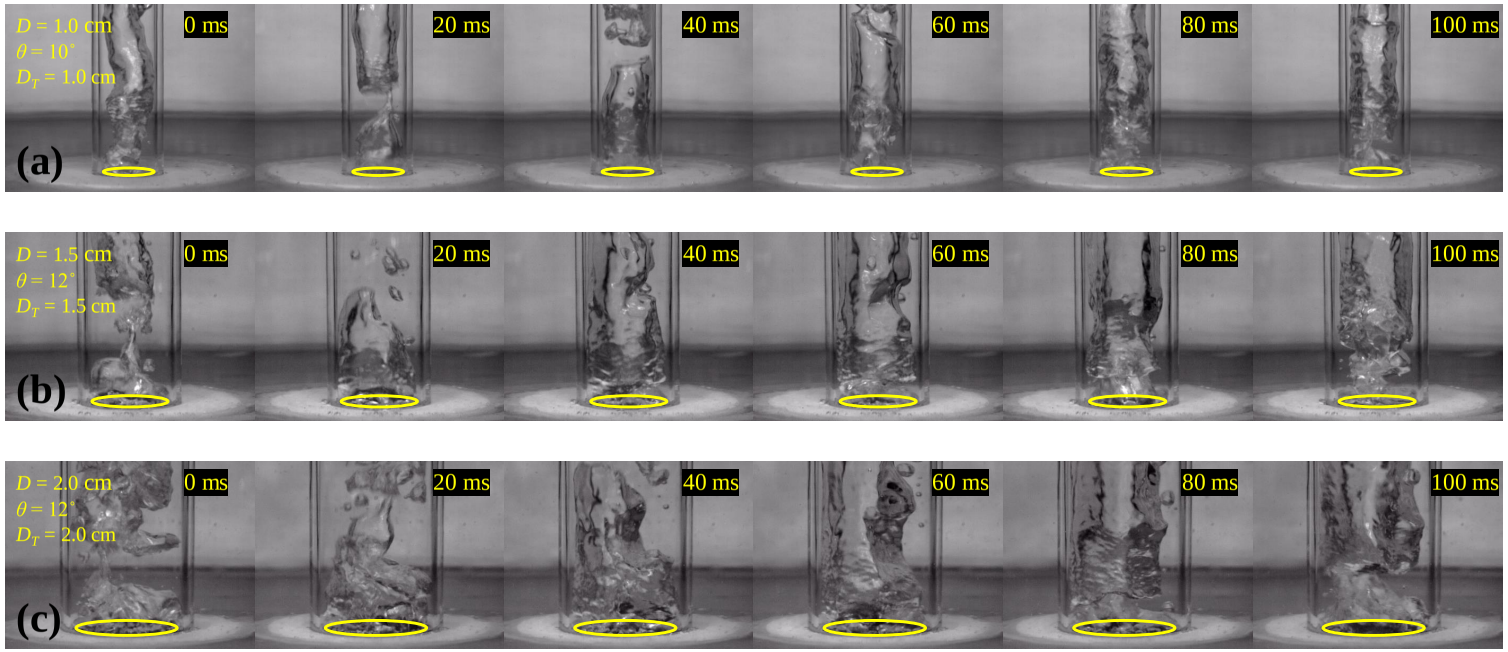

Figure 5.3: Sequential photographs of vapor removal pattern near CHF for the well wetted discs of diameters (a) $D =$ 1.0 cm, (b) $D = 1.5$ cm, and (c) $D = 2.0$ cm. For all the cases, the ratio of heater size to surrounding vessel size D/D_T is 1.

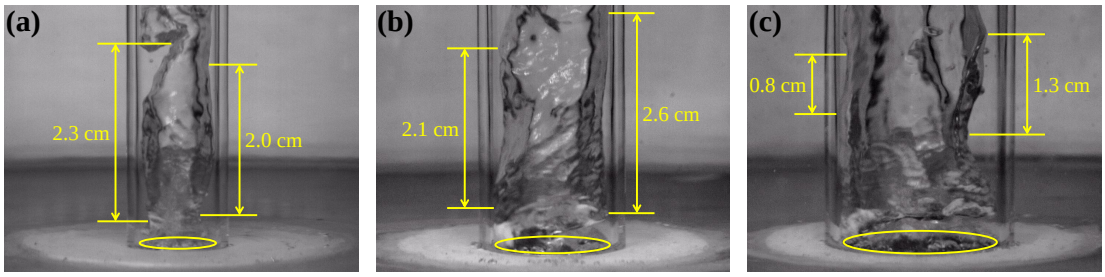

Figure 5.4: Wavelengths at water-steam interface for the well wetted discs of diameters (a) $D = 1.0$ cm and (b) $D = 1.5$ cm. (c) Half wavelengths at water-steam interface for the well wetted 2.0-cm-diameter disc.

of inviscid liquid and vapor streams flowing parallel to each other is given by Kelvin-Helmholtz instability, i.e.,

$$(V_v - V_l)_{crit} = \sqrt{\frac{2\pi\sigma\,(\rho_l + \rho_v)}{\lambda_H \rho_l \rho_v}}, \tag{5.6}$$

where V_l and V_v are the velocities of the liquid and vapor, respectively, in the direction of the vapor stream. An effort was also made to measure the Helmholtz unstable wavelength at water-steam interface from the photographs taken, as shown in Figure 5.4. There is significant uncertainty in the measurement because of the challenges of distinguishing the peak and valley of a wave and differentiating the wave from breakups of the jet. For the discs of diameters $D = 1.0$, 1.5, and 2.0 cm, the measured wavelengths ranged from 1.5 to 2.3 cm, 1.6 to 2.6 cm, and 1.3 to 2.6 cm, respectively, the corresponding average wavelengths λ_H were 1.9, 2.1, and 2.0 cm. Figure 5.4 shows one of the clearest photographs of wavelengths measured at water-steam interface for the discs of diameters (a) $D = 1.0$ cm and (b) $D = 1.5$ cm, and (c) half wavelengths measured for the 2.0-cm-diameter disc. It is of great interest to note that the measured Helmholtz wavelengths λ_H, varying from 1.3 to 2.6 cm, are comparable to the two-dimensional critical and "most dangerous" Taylor wavelengths of 1.57 and 2.72 cm, respectively. The velocities of the liquid

V_l and vapor V_v are also governed by an equation of mass balance performed at a horizontal cross section of the vapor stream, i.e.,

$$\rho_v A_v V_v + \rho_l \left(A - A_v\right) V_l = 0, \tag{5.7}$$

where A_v is the cross-sectional area of the vapor jet, and A is the area of a unit "cell" on which the vapor jet is located. As there is only one vapor jet existing on the disc surface in this study, A is the top surface area of the disc. The critical vapor velocity $V_{v,crit}$ can be obtained by solving Equations (5.6) and (5.7) and expressed as

$$V_{v,crit} = \sqrt{\frac{2\pi\sigma\left(\rho_l + \rho_v\right)}{\lambda_H \rho_l \rho_v}} \left[1 + \frac{\rho_v A_v}{\rho_l \left(A - A_v\right)}\right]^{-1}. \tag{5.8}$$

The CHF can be expressed in the form of energy balance as

$$q_{CHF} = \frac{\rho_v h_{fg} V_{v,crit} A_v}{A}. \tag{5.9}$$

By substituting the critical vapor velocity $V_{v,crit}$ with Equation (5.8) and recognizing $(\rho_l + \rho_v)/\rho_l \approx 1$ as long as the system pressure is enough less than the critical pressure, the CHF expression can be written as

$$q_{CHF} = \rho_v h_{fg} \sqrt{\frac{2\pi\sigma}{\lambda_H \rho_v}} \left[1 + \frac{\rho_v A_v}{\rho_l \left(A - A_v\right)}\right]^{-1} \frac{A_v}{A}. \tag{5.10}$$

Replacing A_v/A by f_v and dividing Equation (5.10) by Equation (5.3) give the dimensionless CHF expression

$$\frac{q_{CHF}}{q_{CHF,Z}} = \frac{19.15}{\sqrt{\lambda_H}} \left(\frac{1}{f_v} + \frac{\rho_v/\rho_l}{1 - f_v}\right)^{-1} \left[\frac{\sigma}{\left(\rho_l - \rho_v\right) g}\right]^{1/4}. \tag{5.11}$$

According to Equation (5.11), the dimensionless CHF should be a function of the Helmholtz unstable wavelength λ_H and fraction of heater surface area occupied by vapor jet f_v for a given liquid under a certain condition. When f_v is relatively small, the term $(\rho_v/\rho_l)/(1-f_v)$ at low pressures is much less than the term $1/f_v$ in Equation (5.11) and so can be reasonably omitted. For large horizontal flat plate

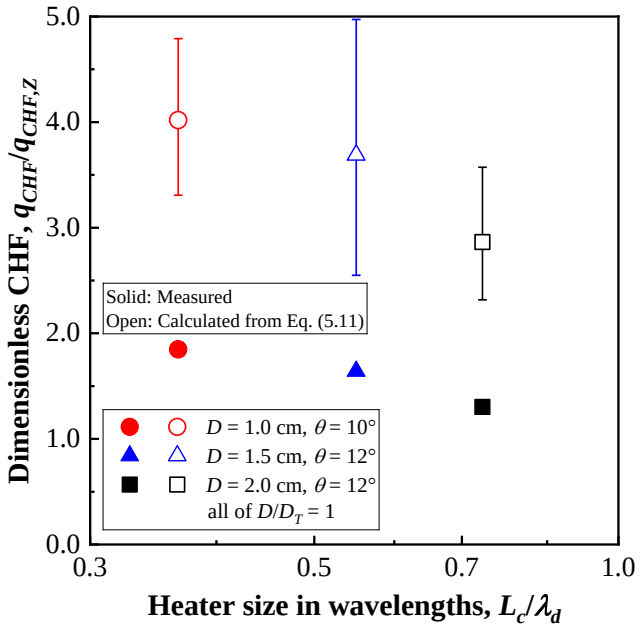

Figure 5.5: Comparison of the measured dimensionless CHF and that calculated from Equation (5.11) for the well wetted discs of diameters $D = 1.0$, 1.5, and 2.0 cm

heaters, $\lambda_H = \lambda_d = 2.72$ cm, $f_v = \pi/16$, and the dimensionless CHF is calculated to be 1.14 [104, 105]. In this study, however, the value of f_v might be large for the small discs. Thus, the term $(\rho_v/\rho_l)/(1 - f_v)$ in Equation (5.11) was included in the following calculations.

By substituting the properties of saturated water and steam at one-atmosphere pressure, i.e., $\sigma = 0.0589$ N/m, $\rho_l = 957.9$ kg/m^3, and $\rho_v = 0.596$ kg/m^3, normal earth gravitational acceleration $g = 9.8$ m/s^2, as well as the average measured vapor jet diameter D_v ($f_v = (D_v/D)^2$) and the average measured Helmholtz unstable wavelength λ_H for each disc into Equation (5.11), the corresponding dimensionless CHF was calculated to be 4.02, 3.69, and 2.86 for the discs of diameters $D = 1.0$, 1.5, and 2.0 cm, respectively. Figure 5.5 shows the comparison of the measured

dimensionless CHFs and those calculated from Equation (5.11). The bounds on the calculated average values correspond to the cases when maximum and minimum values of D_v were combined with maximum and minimum values of λ_H, respectively. It is not a surprise that the predicted CHFs are higher than the measured CHFs. The two-phase flow is speculated to be more complicated than just parallel flows of vapor and liquid traveling in opposite directions. The vapor can drag part of the liquid nearby to move upward. This effect will not be significant until the vapor jet is confined by the surrounding vessel. Besides, the route of the liquid flowing back is squeezed into a thin film where the viscosity dominates. These mechanisms not considered in the hydrodynamic theory dictate CHF when the heater size becomes less than the two-dimensional "most dangerous" Taylor wavelength λ_d.

5.2.2 Contact angle effect

Figure 5.6 shows the dimensionless CHF measured for the discs as a function of contact angle θ when the surrounding vessel diameter D_T was equal to the disc diameter D, i.e., $D/D_T = 1$. For the discs of diameters $D = 1.0$, 1.5, and 2.0 cm, as the contact angle increases from about 10 to 80°, the CHF decreases from 203 to 76 W/cm^2, 181 to 74 W/cm^2, and 143 to 77 W/cm^2, respectively, and the dimensionless CHF decreases from 1.85 to 0.69, 1.64 to 0.68, and 1.30 to 0.70, accordingly. CHFs reported by Maracy and Winterton [78] for a 2.66-cm-diameter surface and Girard *et al.* [91] for a 1 cm × 1 cm surface of different contact angles are also added for comparison. It should be pointed out that Maracy and Winterton conducted transient boiling and the surface used by them was confined by a glass tube of inner diameter that was equal to the surface diameter, namely, $D/D_T = 1$. Girard *et al.* performed steady-state boiling with a large surrounding vessel, and the corresponding D/D_T was close to 0. As shown

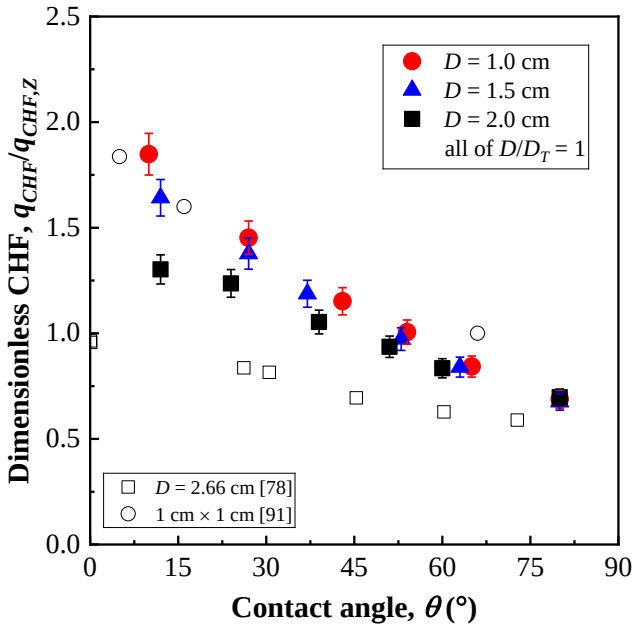

Figure 5.6: Dimensionless CHF as a function of contact angle θ for the discs of diameters D = 1.0, 1.5, and 2.0 cm

in Figure 5.6, the trend of CHF against contact angle θ for the 1.0-cm-diameter disc from this study is in good agreement with that for the 1 cm × 1 cm surface reported by Girard *et al.* [91]. The CHF data in Figure 5.6 collectively show that CHF decreases with increasing contact angle regardless of the heater size. In addition, Figure 5.6 shows that CHF increases with decreasing heater size only for low contact angles (or well wetted surfaces), which is attributed to the increase of vapor removal limit, as discussed in the earlier sections. However, for high contact angles (or partially wetted surfaces), it appears that it is not the vapor removal limit that determines the maximum heat flux. Even the cited CHF data show some variances at high contact angles, the heater size effect clearly diminishes as the contact angle increases by observing the CHFs from this study. It is in good agreement with the argument by Dhir and Liaw [93] that CHF for partially

wetted surfaces is set by the vapor production limit, which is independent of the heater size as long as there are many active nucleation sites on the surface. The difference in CHFs for high contact angles reported in References [78,90,91] might be attributed to experimental uncertainties, different types of boiling (steady-state or transient), different methods or criteria of determining contact angle, different surface orientations (horizontal or vertical), and other uncontrolled parameters, such as surrounding vessel size and liquid height.

Figure 5.7 shows the sequential photographs of boiling near CHF for the 1.5-cm-diameter disc to visualize the corresponding vapor removal pattern when the disc featured contact angles (a) $\theta = 12°$, (b) $\theta = 37°$, and (c) $\theta = 63°$. When the disc features different contact angles θ, the vapor generated always tends to fill the surrounding vessel and shows no obvious difference in the vapor jet size. Even so, as the contact angle θ increases from 12 to 63°, the vapor jet appears to take less space and leave more space for liquid flowing back toward the disc surface, as shown in the photographs taken at 60 ms in Figure 5.7, which is possibly attributed to the reduced vapor generation rate with increasing contact angle θ.

Both Dhir and Liaw's vapor generation model [93] and Kandlikar's force balance model [113] can explain the decrease in CHF with worsening surface wettability. Meanwhile, the former can also capture the interacting effect of heater size and contact angle on CHF. Figure 5.6 shows no apparent heater size effect for the partially wetted discs as the CHF is set by the maximum vapor generation rate, which is independent of the heater size. However, for the well wetted discs, the CHF is set by the maximum vapor removal rate as assumed in the hydrodynamic theory.

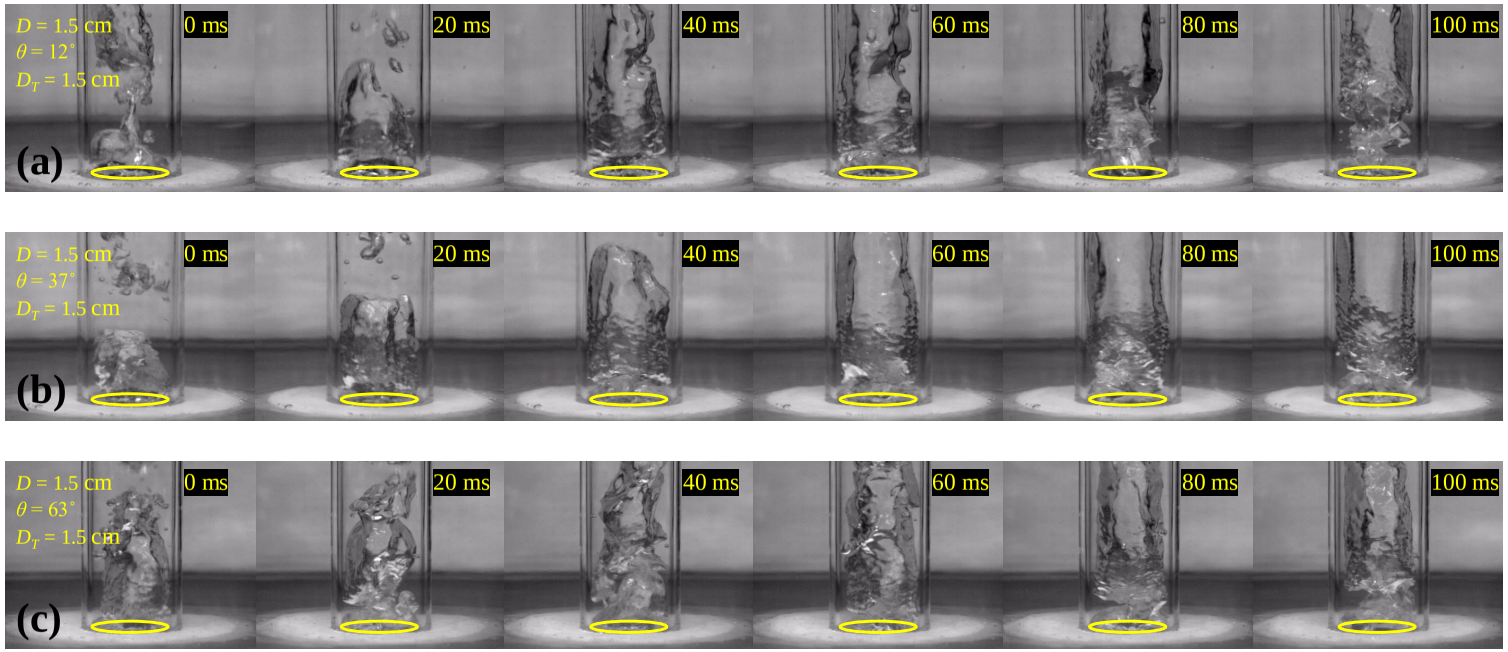

Figure 5.7: Sequential photographs of vapor removal pattern near CHF for the 1.5-cm-diameter disc when it featured contact angles (a) $\theta = 12°$, (b) $\theta = 37°$, and (c) $\theta = 63°$. For all the cases, the ratio of heater size to surrounding vessel size D/D_T is 1.

5.2.3 Surrounding vessel size effect

Figure 5.8 shows the dimensionless CHF measured for the discs of contact angle $\theta \approx 10^{\circ}$ as a function of the ratio of heater size to surrounding vessel size D/D_T. For the discs of diameters $D = 1.0$, 1.5, and 2.0 cm, as the vessel diameter increases from the disc diameter to 20.0 cm, the CHF increases from 203 to 233 W/cm^2, 181 to 218 W/cm^2, and 143 to 150 W/cm^2, respectively, and the dimensionless CHF increases from 1.85 to 2.11, 1.64 to 1.98, and 1.30 to 1.36, accordingly. CHFs reported by Bockwoldt *et al.* [97] for a horizontal 1.5-cm-diameter surface are also added for comparison. They did not report contact angle but stated that CHF was measured for the nickel-plated copper surface that was aged until the CHF became stable. Thus, it is assumed that the surface used by them was well wetted. Besides, as they investigated the effects of surrounding vessel size and liquid height, only the CHFs measured for liquid heights of about 20 cm are plotted in Figure 5.8 to eliminate any effect of changed liquid height. It can be seen from Figure 5.8 that the trend of CHF against the ratio of heater size to surrounding vessel size D/D_T for the 1.5-cm-diameter disc from this study agrees well with that for the 1.5-cm-diameter surface reported by Bockwoldt *et al.* [97]. Figure 5.8 establishes that CHF increases as the surrounding vessel size increases. Besides, the CHF data also point out that the magnitude of enhancement in CHF decreases as the heater size increases. For the 2.0-cm-diameter disc, the effect of surrounding vessel size is within the uncertainty of the CHF data.

Figure 5.9 shows the sequential photographs of boiling near CHF for the 1.5-cm-diameter disc of contact angle $\theta = 12^{\circ}$ to visualize the corresponding vapor removal pattern when the disc was surrounded by vessels of diameters (a) $D_T = 1.5$ cm, (b) $D_T = 3.0$ cm, (c) $D_T = 7.5$ cm, and (d) $D_T = 20.0$ cm. As seen in Figure 5.9 (a), when the vessel diameter D_T is 1.5 cm, the generated vapor develops vertically into a continuous vapor jet. However, when the vessel diameter D_T

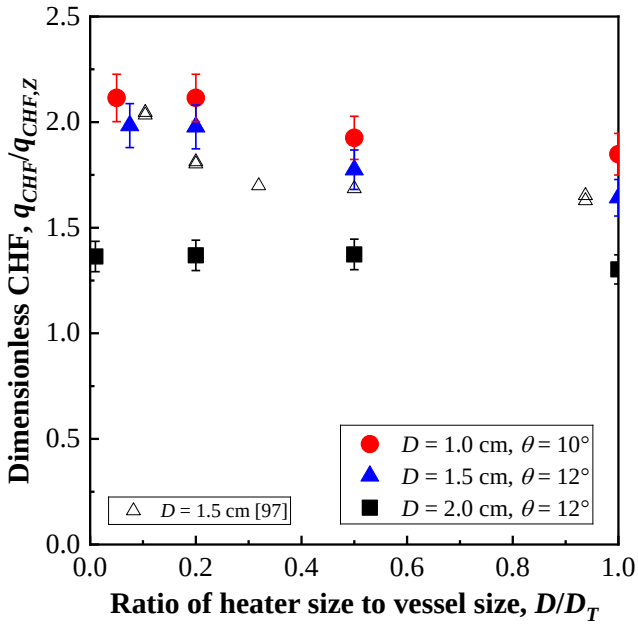

Figure 5.8: Dimensionless CHF as a function of the ratio of heater size to surrounding vessel size D/D_T for the well wetted discs of diameters D = 1.0, 1.5, and 2.0 cm

increases to 3.0, to 7.5, and to 20.0 cm, as shown in Figures 5.9 (b) to (d), the removal of generated vapor in a continuous columnar structure appears to break down, and large vapor slugs, which appear to be discontinuous, now leave the disc surface.

The enhancement in CHF by enlarging the surrounding vessel can be attributed to induced convection flow as well as improved stability of vapor columns. As the surrounding vessel size increases, the induced convection flow increases convective heat transfer contribution and affects the formation and stability of vapor jets. As can be deduced from Equation (5.6), the upward flow of liquid adjacent to the vapor jet will increase the critical vapor velocity for instability to occur, thus increasing the CHF. However, for larger heaters, when the vapor jet diameter

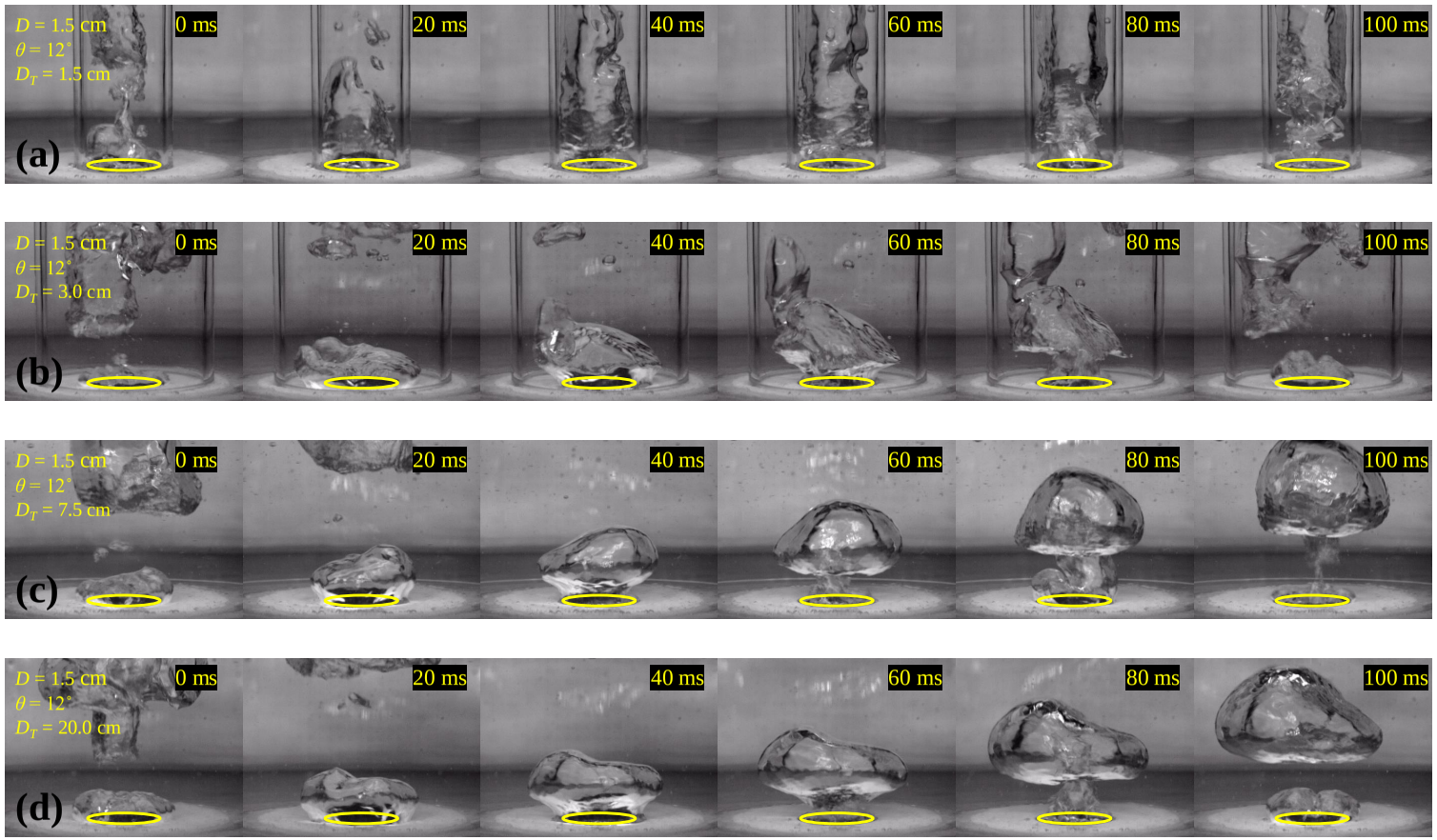

Figure 5.9: Sequential photographs of vapor removal pattern near CHF for the 1.5-cm-diameter disc of contact angle θ = 12° when it was surrounded by vessels of diameters (a) D_T = 1.5 cm, (b) D_T = 3.0 cm, (c) D_T = 7.5 cm, and (d) D_T = 20.0 cm

is much smaller than the heater size, the convective contribution will increase. In the absence of measurement of the flow field in the vicinity of the vapor jets, it is difficult to separate the contribution of each.

5.3 Summary

The findings of this chapter are summarized as that (i) for well wetted surfaces, critical heat flux increases with decreasing heater size when the heater size L_c is less than the two-dimensional "most dangerous" Taylor wavelength λ_d and appears to reach an asymptotic value at $L_c/\lambda_d \approx 0.3$, (ii) critical heat flux decreases with increasing contact angle regardless of the heater size, (iii) the heater size effect on critical heat flux is not pronounced for partially wetted surfaces where the critical heat flux is limited by the maximum vapor generation rate, which is independent of the heater size when many active nucleation sites are present, and (iv) critical heat flux increases with increasing surrounding vessel size. However, this enhancement degrades with increasing heater size.

CHAPTER 6

Surface structure effect

This chapter presents the boiling heat transfer data obtained on structured and plain surfaces and discusses the surface structure effect on nucleate boiling heat flux for small horizontal surfaces. Comparisons of boiling curves and CHFs for structured and plain surfaces are also performed. Prior to that, the background of the surface structure effect is introduced.

6.1 Background

By analyzing a dataset collecting CHFs of various surface-liquid combinations reported by Berenson [110], Lienhard and Dhir [104], Ramilison and Lienhard [121], Rajab and Winterton [122], and Reguillot [123], Ramilison *et al.* [124] found that surface wettability greatly affects CHF while surface roughness influences it weakly. All the data were selected from horizontal flat plate heaters of sizes greater than 2.0 times the two-dimensional "most dangerous" Taylor wavelength λ_d to eliminate the influence of heater size. They postulated that the surface roughness effect mainly manifests in early nucleate boiling regime where little interaction occurs between neighboring nucleation sites.

However, with the development and application of micro/nanofabrication techniques, a large number of boiling experiments have been carried out on micro/nanostructured surfaces and showed enhancement in nucleate boiling heat flux and CHF to various degrees. In References [2, 125–129], nanoparticles were either

directly added in test liquids to create nanofluids or deposited on heater surfaces to form micro/nanostructures. In References [1, 3, 130–133], carbon nanotubes formed by chemical vapor deposition or nanowires fabricated by either electrochemical etching or deposition were applied. Besides, in References [4, 134–138], microstructures in the form of micropillar or microcavity arrays were fabricated and in several works were coupled with nanoparticles or nanowires to form hierarchical structures on heater surfaces.

The majority of these studies attribute the enhancement in nucleate boiling heat flux to a larger heating area and increased number of nucleation sites and ascribe the increase in CHF to improved surface wettability and "wicking effect" resulting from the micro/nanostructure added on the heater surface [1, 3, 91, 114, 119]. However, it is crucial to isolate the contribution of added structure from that of improved wettability as the structure can change the apparent contact angle of a surface, as introduced in Chapter 1. Besides, it is also noted that the effects of heater size and surrounding vessel size were ignored in many studies. The enhancements in CHF were concluded based on improper comparisons of the CHFs obtained on small surfaces in large vessels with Zuber's CHF prediction for infinite horizontal flat plates. Therefore, it is worth investigating the individual effects of surface structure on nucleate boiling heat flux and CHF by well controlling the remaining experimental parameters during the study.

6.2 Results and discussion

Figure 6.1 shows the SEM images of (a) Si-nanowires and (b) Cu-nanowires surfaces investigated by Chen *et al.* [1], (c) and (d) Al_2O_3-nanoparticles surfaces investigated by Kwark *et al.* [2], (e) and (f) Si-nanowires surfaces investigated by Lu *et al.* [3], and (g) and (h) Cu-nanowires and (i) Cu-micropillars & nanowires

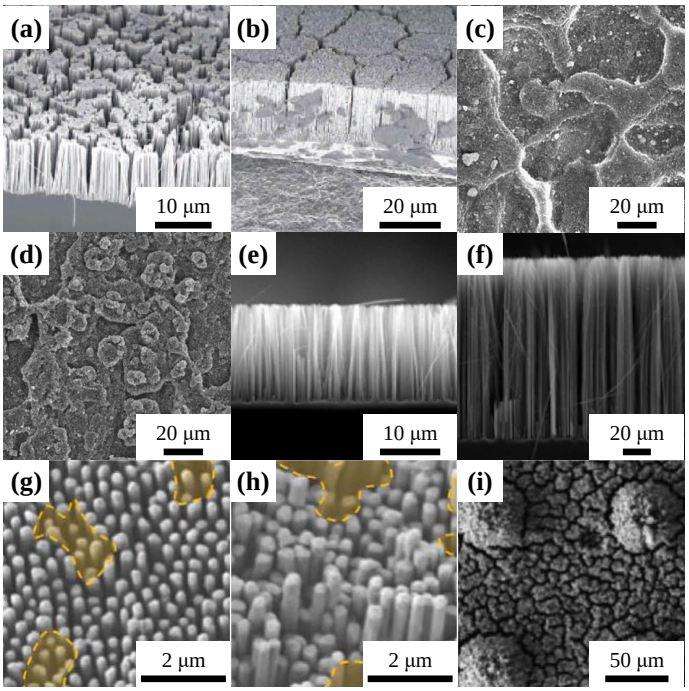

Figure 6.1: SEM images of (a) Si-nanowires and (b) Cu-nanowires surfaces in side view [1], (c) and (d) Al_2O_3-nanoparticles surfaces in top view [2], (e) and (f) Si-nanowires surfaces in side view [3], and (g) and (h) Cu-nanowires surfaces in side view and (i) Cu-micropillars & nanowires surface in top view [4]

surfaces investigated by Wen *et al.* [4]. The corresponding boiling curves of saturated water are shown in Figure 6.2, and the boiling curve measured in this study for the 1.0-cm-diameter plain disc of contact angle $\theta = 10°$ is added for comparison. For all the cases, the characteristic length of surface L_c is 1.0 cm except $L_c = 0.8$ cm in the work of Wen *et al.*, and the surrounding vessel is much larger than the surface, i.e., $D/D_T \approx 0$. As shown in Figure 6.2, the structured surface shows earlier ONB and higher heat flux at a given surface superheat in nucleate boiling regime for most of the cases. For instance, at surface superheat $\Delta T_s = 20°C$, the structured surfaces show heat fluxes q up to 2.5 times that for the plain surface.

To investigate the surface structure effect on nucleate boiling heat flux and

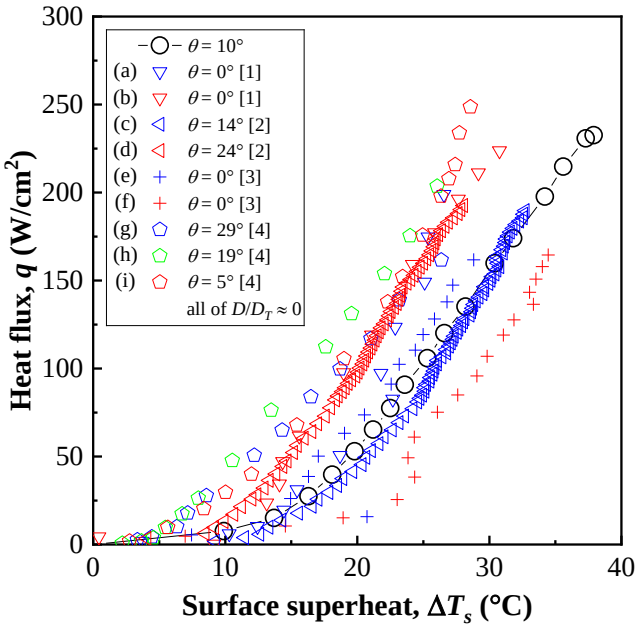

Figure 6.2: Boiling curves for the structured surfaces shown in Figure 6.1. For all the cases, the ratio of heater size to surrounding vessel size D/D_T is about 0.

CHF more rigorously and thoroughly, boiling curves for structured discs of diameters D = 1.0, 1.5, and 2.0 cm were obtained for different contact angles θ and surrounding vessel diameters D_T. The structured discs were fabricated following the methods developed in Chapter 2, in which the SEM image of the structured surface is also shown. The boiling curves measured for the structured and plain discs were compared by keeping other parameters nearly the same. Rohsenow's correlation, i.e., Equation (4.1), was applied to fit the nucleate boiling heat transfer data to assess the surface structure effect on the correlating constant C_{sf}. In addition, the CHFs measured for the well wetted structured and plain discs were compared with those reported in other studies.

6.2.1 On nucleate boiling heat flux

For well wetted surfaces

Figure 6.3 shows the boiling curves measured for the well wetted structured discs of diameters (a-b) D = 1.0 cm, (c-d) D = 1.5 cm, and (e-f) D = 2.0 cm with contact angle $\theta = 0°$. In addition, the boiling curves measured for the well wetted plain discs of contact angle $\theta \approx 10°$ are added for comparison. For all the cases, the surrounding vessel diameter D_T was equal to the disc diameter D, i.e., D/D_T = 1. In each figure, the boiling curve steepens and develops into nucleate boiling regime earlier with structure added on the surface, while the CHF hardly changes. For instance, as shown in Figure 6.3 (c), at surface superheat ΔT_s = 19°C, the heat flux q is about 49 W/cm^2 on the 1.5-cm-diameter plain disc and increases to about 112 W/cm^2 as the surface becomes structured. The corresponding CHFs are 181 and 190 W/cm^2, respectively, which are nearly the same.

Figures 6.3 (b), (d), and (f) show the boiling curves on logarithmic scales, and Rhosenow's correlation is plotted to fit each boiling curve. In each figure, the linear trends formed by the boiling heat transfer data are consistent between the structured and plain discs. Therefore, the exponent 3 on surface superheat ΔT_s in Rohsenow's correlation was kept the same as that chosen for the plain discs. The corresponding fit lines are thus parallel to each other only with different values of C_{sf}. C_{sf} decreases greatly with structure added on the surface. For instance, it decreases by about 24 % from 0.0164 to 0.0125 with structure added on the 1.5-cm-diameter plain disc.

For partially wetted surfaces

It is also of great interest to look at the surface structure effect on nucleate boiling heat flux for partially wetted surfaces. Figure 6.4 shows the boiling curves

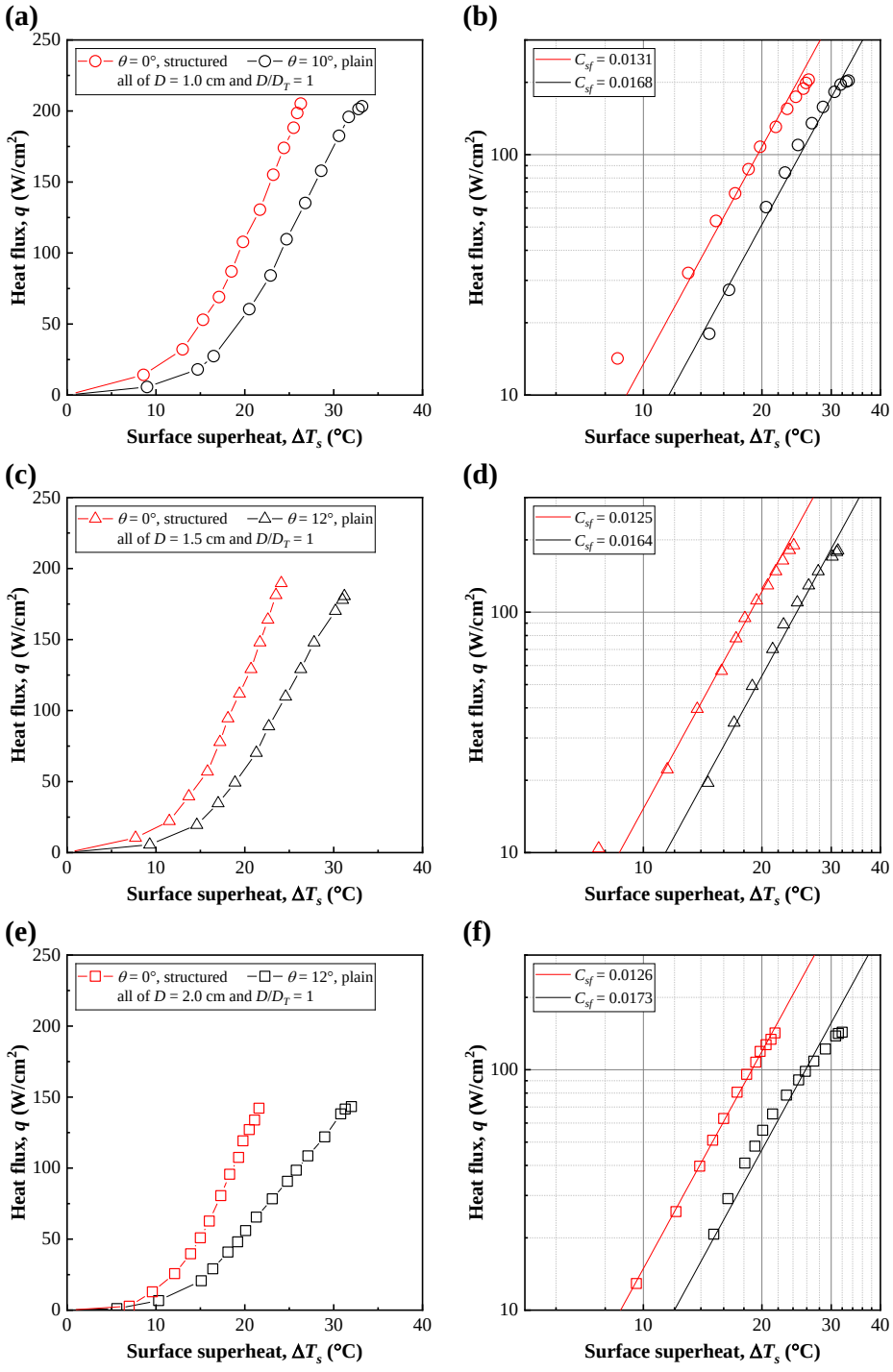

Figure 6.3: Boiling curves for the well wetted structured and plain discs of diameters (a-b) $D = 1.0$ cm, (c-d) $D = 1.5$ cm, and (e-f) $D = 2.0$ cm with similar contact angles θ. For all the cases, the ratio of heater size to surrounding vessel size D/D_T is 1.

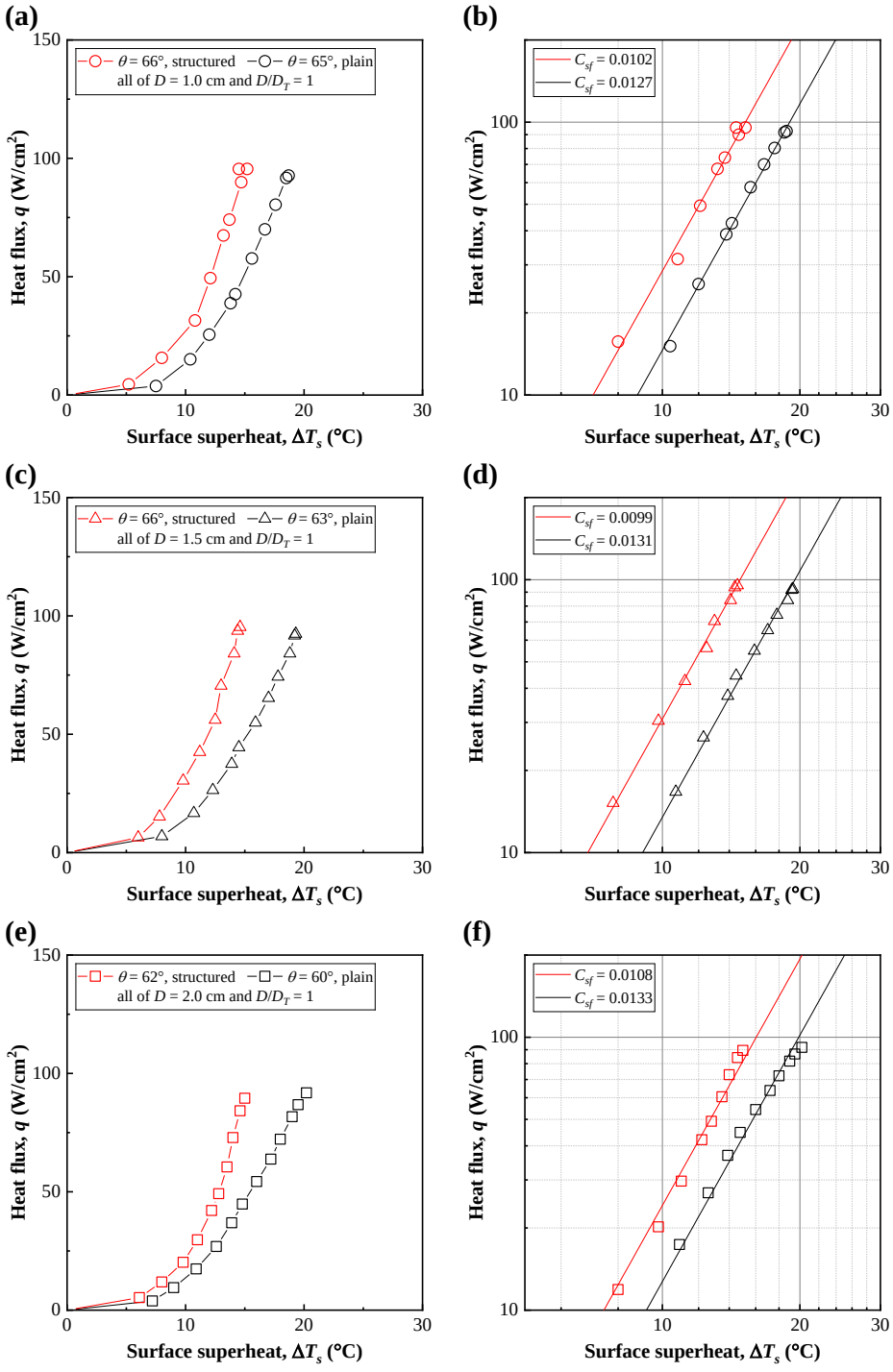

Figure 6.4: Boiling curves for the partially wetted structured and plain discs of diameters (a-b) $D = 1.0$ cm, (c-d) $D = 1.5$ cm, and (e-f) $D = 2.0$ cm with similar contact angles θ. For all the cases, the ratio of heater size to surrounding vessel size D/D_T is 1.

measured for the partially wetted structured discs of diameters (a-b) $D = 1.0$ cm, (c-d) $D = 1.5$ cm, and (e-f) $D = 2.0$ cm with contact angle $\theta \approx 60°$. For comparison, the boiling curves measured for the partially wetted plain discs of contact angle $\theta \approx 60°$ are added. For all the cases, the surrounding vessel diameter D_T was equal to the disc diameter D, i.e., $D/D_T = 1$. In each figure, the structured surface features higher heat flux at a given surface superheat in nucleate boiling regime but shows similar CHF, which is consistent with the outcome for the well wetted discs. For instance, as shown in Figure 6.4 (c), at surface superheat $\Delta T_s = 14°$C, the heat flux q is about 38 W/cm^2 on the 1.5-cm-diameter plain disc and increases to about 84 W/cm^2 with structure added on the surface. The corresponding CHFs are 92 and 95 W/cm^2, respectively, which are nearly the same. Figures 6.4 (b), (d), and (f) show the boiling curves on logarithmic scales, and Rhosenow's correlation is plotted to fit each boiling curve. In each figure, the linear trends formed by the boiling heat transfer data are consistent between the structured and plain discs only with decreasing C_{sf} as the surface becomes structured. For instance, it decreases by about 24 % from 0.0131 to 0.0099 with structure added on the 1.5-cm-diameter plain disc.

Figure 6.5 shows the value of C_{sf} as a function of contact angle for the structured and plain discs. It indicates that for structured surfaces, C_{sf} still decreases with increasing contact angle as long as the surface topography remains unchanged, which agrees with that for plain surfaces, as discussed in Chapter 4. Thus, C_{sf} is not just a function of contact angle but also of surface topography.

Figure 6.6 shows the photographs of nucleate boiling near $q = 20$ W/cm^2 on the well wetted structured and plain discs of diameters $D = 1.0$, 1.5, and 2.0 cm with similar contact angles θ. The structured discs feature higher heat fluxes q at lower surface superheats ΔT_s. A similar outcome is also found in Figure 6.7 which shows the photographs of nucleate boiling near $q = 20$ W/cm^2 on the partially

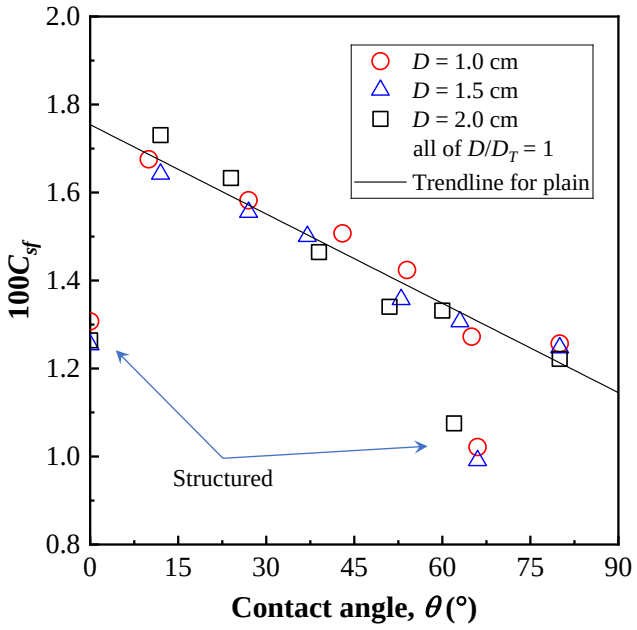

Figure 6.5: Correlating constant of Rohsenow's correlation C_{sf} as a function of contact angle θ for the structured and plain discs

wetted structured and plain discs of similar contact angles θ.

Figures 6.3 and 6.4 establish that adding structure on a heater surface contributes to earlier ONB and higher heat flux in nucleate boiling regime. As one of the results, the structured surface also features higher HTC at a given surface superheat, as shown in Figures 6.8 and 6.9. Moreover, the consistent trends in Figures 6.3 and 6.4 indicate that the dependence of heat flux on surface superheat in nucleate boiling regime remains the same among structured and plain surfaces.

The enhancement in nucleate boiling heat flux can be attributed to the increase of nucleation sites resulting from the microgrooves created on the surface. These microgrooves, as shown in Figure 2.6, about 10 μm in both width and depth, might not work as nucleation sites directly as the dimensions are greater than the sizes of unflooded cavities ($\sim$ 0.1 to 1 μm). However, the tiny scratches and pits

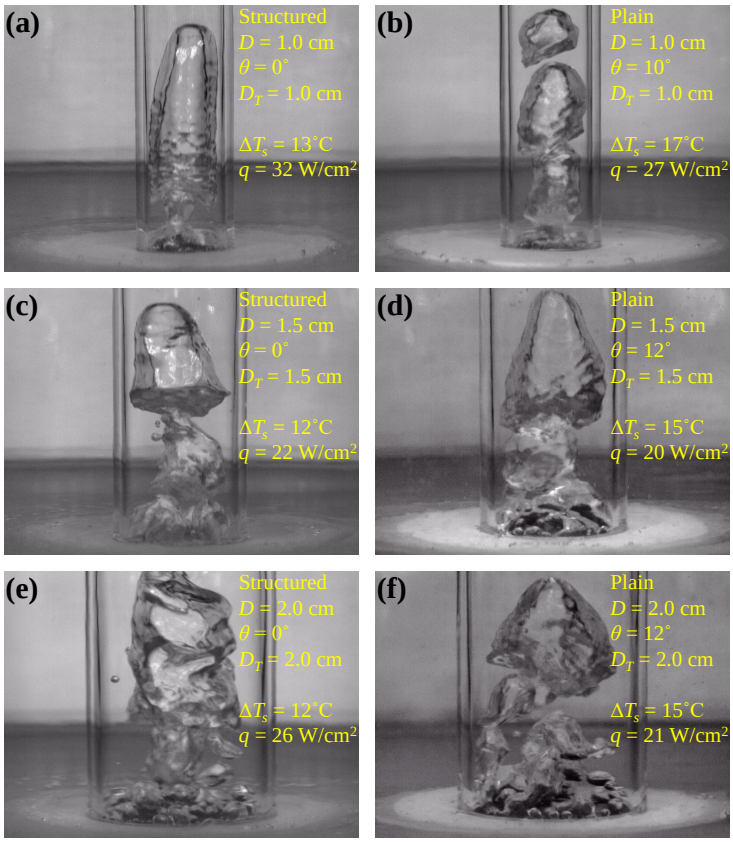

Figure 6.6: Photographs of nucleate boiling near $q = 20$ W/cm^2 on the well wetted 1.0-cm-diameter (a) structured and (b) plain discs of similar contact angles θ, 1.5-cm-diameter (c) structured and (d) plain discs of similar contact angles θ, and 2.0-cm-diameter (e) structured and (f) plain discs of similar contact angles θ

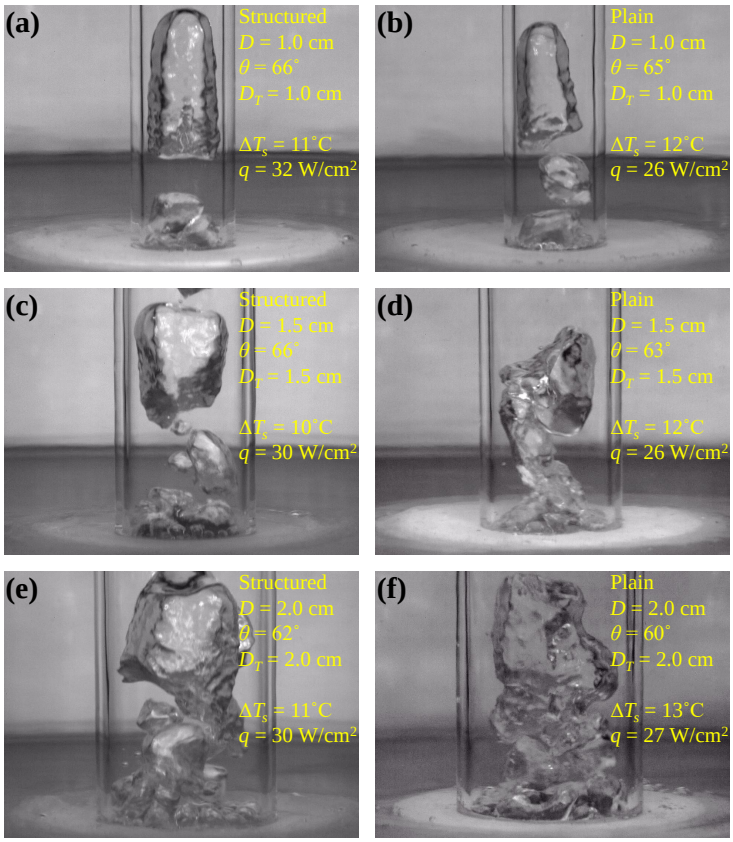

Figure 6.7: Photographs of nucleate boiling near $q = 20$ W/cm^2 on the partially wetted 1.0-cm-diameter (a) structured and (b) plain discs of similar contact angles θ, 1.5-cm-diameter (c) structured and (d) plain discs of similar contact angles θ, and 2.0-cm-diameter (e) structured and (f) plain discs of similar contact angles θ

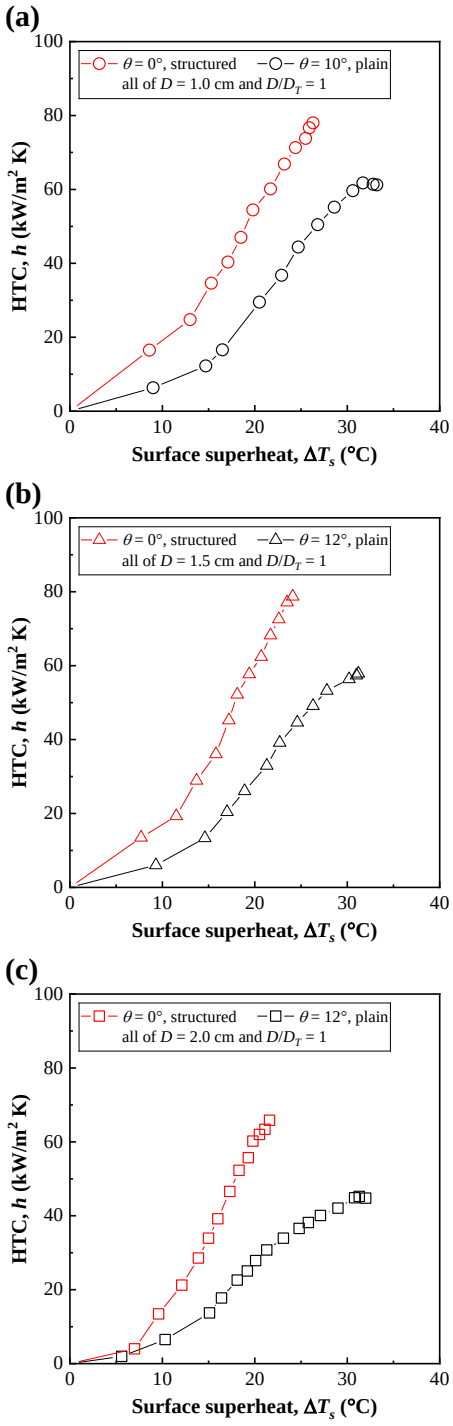

Figure 6.8: HTC as a function of surface superheat ΔT_s for the well wetted structured and plain discs of diameters (a) $D = 1.0$ cm, (b) $D = 1.5$ cm, and (c) $D = 2.0$ cm with similar contact angles θ

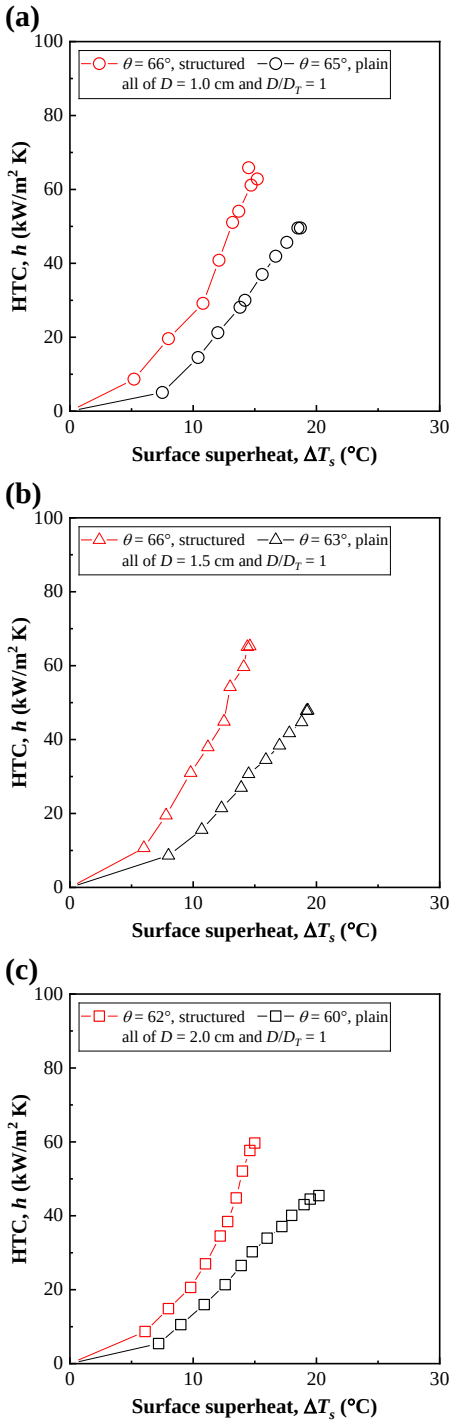

Figure 6.9: HTC as a function of surface superheat ΔT_s for the partially wetted structured and plain discs of diameters (a) $D = 1.0$ cm, (b) $D = 1.5$ cm, and (c) $D = 2.0$ cm with similar contact angles θ

introduced along with the sanding process are smaller than the microgrooves and can potentially serve as additional nucleation sites. Thus, the increased number density of nucleation sites contributes to a higher vapor generation rate, which makes the structured surface feature higher heat flux at a given surface superheat. It should be stressed that the above outcomes are based on the structured surfaces fabricated in this study. Structures fabricated in other studies might be in favorable dimensions and can introduce more nucleation sites on the surface. Besides, when the structure dimensions become comparable to the vapor stem size ($\sim 10^{-3}$ m) in fully developed nucleate boiling regime, the structure can also reduce the thermal resistance by penetrating the liquid between the surface and stems.

6.2.2 On critical heat flux

In the earlier section, Figures 6.3 and 6.4 also indicate that the CHF is independent of the surface topography as long as the heater size and contact angle are fixed. As discussed in Chapters 4 and 5, CHF for a plain surface mainly relies on the heater size and surface wettability. Therefore, CHF for a partially wetted plain surface will increase with structure added if the structure improves the surface wettability. When a plain surface is well wetted, the CHF should correspond to the maximum vapor removal rate described in the hydrodynamic theory and thus remains unchanged even with structure added on the surface. In this study, for plain surfaces, the highest measured CHF of 233 W/cm^2 was obtained on the 1.0-cm-diameter disc of contact angle $\theta = 10^\circ$ surrounded by a 20.0-cm-diameter vessel. Making the disc structured reduced the contact angle θ to 0°, while the measured CHF is 229 W/cm^2 and hardly changed. Similar CHFs were also reported by Bockwoldt *et al.* ($L_c = 1.5$ cm and $q_{CHF} = 227$ W/cm^2) [97], Girard *et al.* ($L_c = 1.0$ cm and $q_{CHF} = 202$ W/cm^2) [91], and Das *et al.* (L_c

= 0.9 cm and q_{CHF} = 236 W/cm^2) [139] who boiled saturated water on small plain surfaces that were well wetted. It is worth noting that enhanced CHFs, recently reported in some experimental studies and claimed to be the results of adding micro/nanostructures, also reached about 2.0 to 2.5 times Zuber's CHF prediction [1–4, 98, 114, 137, 139].

Table 6.1 summarizes the experimental parameters and surface characteristics of several representative studies and this study. In these studies, CHF was measured for either plain or structured surfaces or both. Several essentials need to be pointed out before comparing the CHFs. (i) Different methods and criteria of determining contact angle were employed in these studies, e.g., Chu *et al.* [137] adopted receding contact angles, while the rest used apparent static contact angles. Besides, measuring contact angles before and after boiling can also give different values due to surface aging and potential fouling, e.g., in this study, the pre- and post-boiling contact angles can show a difference up to 23°, as shown in Table 2.1. Other factors like droplet size, time of measurement after placing droplet, and liquid and surface temperatures can also affect measured contact angle. (ii) The ratios of heater size to surrounding vessel size were different in these studies. As shown in Table 6.1, Lienhard *et al.* [106], Maracy and Winterton [78], and Bockwoldt *et al.* [97] performed boiling near $D/D_T = 1$, while the remaining conducted boiling near $D/D_T = 0$ or did not report any information about liquid-holding vessel. (iii) Liquid heights might be different in these studies as well. Elkassabgi and Lienhard [96] and Bockwoldt *et al.* [97] studied the effect of liquid height on CHF and found that CHF increased and asymptotically reached its maximum with increasing liquid height. Overall, these existing and potential differences should be aware when comparing the CHFs from these studies.

Figure 6.10 shows the dimensionless CHF as a function of heater size nondimensionalized with the two-dimensional "most dangerous" Taylor wavelength

Table 6.1: Experimental parameters and surface characteristics of representative studies and this study

Author(s)	No. of CHFs	Liquid(s)	L_c/λ_d	Contact angle, θ (°)	L_c/D_T	Surface characteristics
Lienhard *et al.* [106]	13	Ethanol Isopropanol Methanol Water [94]	0.33 – 1.89	0 [3]	1	Square, plain, Cu
Liaw and Dhir [90] [1]	6	Water	3.79	14 – 107	-	Rectangular, plain, Cu/fluorosilicone/oxidized Cu
Maracy and Winterton [78] [2]	7	Water	0.98	0 – 73	1	Circular, plain, Cu/aged Cu
Bockwoldt *et al.* [97]	54	Water	0.55	0 [3]	0.10 – 0.94	Circular, plain, aged Ni
Chen *et al.* [1]	3	Water	0.37	15, 40	-	Square, plain, Si/SiO_2
	5			0		Square, Si/Cu-nanowires
Kwark *et al.* [2]	3	Water	0.37	83 – 90	0.06	Square, plain, Cu
	41			13 – 61		Square, Al_2O_3-nanoparticles
Kwark *et al.* [98]	8	Water	0.28 – 0.73	88	0.04 – 0.12	Square, plain, Cu
	8			24		Square, Al_2O_3-nanoparticles
Ahn *et al.* [114]	4	Water	0.37	23 – 49	-	Square, plain, Zr-4/oxidized Zr-4
	4			0 – 10		Square, oxidized Zr-4-micro/nanostructures
Lu *et al.* [3]	4	Water	0.18 – 0.73	40	-	Square, plain, Si
	4			0		Square, Si-nanowires
Chu *et al.* [137]	2	Water	0.73	32	-	Square, plain, SiO_2
	7			0		Square, Si/Cu-micropillars & SiO_2/CuO-nanostructures
Girard *et al.* [91]	3	Water	0.37	5 – 66	0.08	Square, plain, $Cu/Cu_2O/CuO$
Das *et al.* [139]	2	Water	0.33	0	-	Circular, plain, Cu
	4			0		Circular, TiO_2-micro/nanostructures
Wen *et al.* [4]	1	Water	0.29	90	0.05	Square, plain, Cu
	3			5 – 29		Square, Cu-nanowires/Cu-micropillars & nanowires
Present study	72	Water	0.37 – 0.73	10 – 80	0.05 – 1	Circular, plain, Cu/oxidized Cu
	24			0 – 66		Circular, Cu/oxidized Cu-microgrooves

[1] Vertical surface, [2] Transient boiling, [3] Estimated value. Ninety-three CHFs of contact angles $\theta < 20°$ in total are plotted in Figure 6.10.

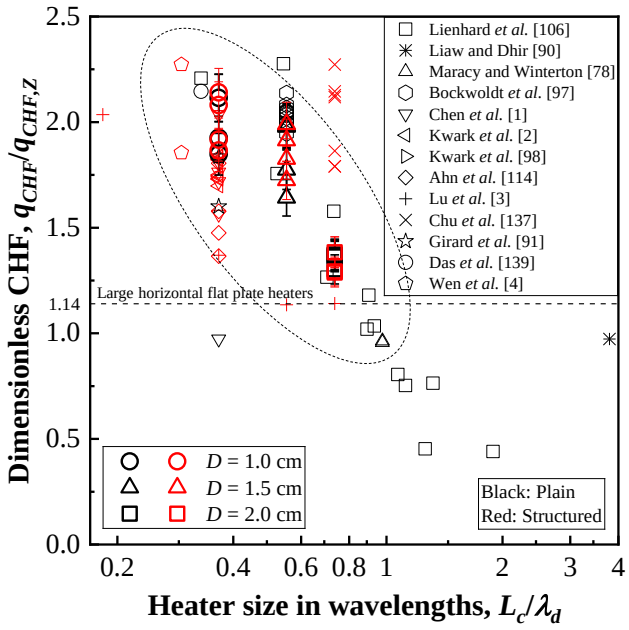

Figure 6.10: Dimensionless CHF as a function of heater size in wavelengths L_c/λ_d for the well wetted plain and structured surfaces

L_c/λ_d for the well wetted plain and structured surfaces of contact angles $\theta < 20°$ from the studies summarized in Table 6.1. It indicates that CHF above that for large horizontal flat plate heaters only occurs when the heater size is less than λ_d, i.e., $L_c/\lambda_d < 1$, regardless of the surface topography. The variances among the CHFs at a given heater size in Figure 6.10 can be attributed to the experimental uncertainties and different experimental parameters as discussed above. However, at $L_c/\lambda_d = 0.73$, relatively large variances exist between the CHFs reported by Chu *et al.* [137] and Lu *et al.* [3] for their structured surfaces of contact angle $\theta = 0°$. Compared to the CHFs from this study, as shown in Figure 6.10, the CHFs reported by Chu *et al.* are higher, and that reported by Lu *et al.* is lower. It cannot be interpreted by the contribution of surface roughness that was proposed by Chu *et al.* as the Si-nanowires surface used by Lu *et al.* also featured

great roughness. Besides, a CHF reported by Chen *et al.* [1] at $L_c/\lambda_d = 0.37$ appears to be lower than the remaining, which cannot be explained as the plain surface was also well wetted. Despite several CHFs not following the trend of CHF against heater size, the upper envelope of the CHF data clearly indicates that for well wetted surfaces, CHF increases with decreasing heater size and asymptotically reaches about 2.0 to 2.5 times Zuber's CHF prediction whether the surfaces are plain or structured.

According to the above comparison, it is rational to infer that the enhancement in CHF by adding structures is attributed to the surface wettability improved by the structures rather than the structures themselves. CHFs above that for large horizontal flat plate heaters result from decreasing the sizes of well wetted surfaces to less than the two-dimensional "most dangerous" Taylor wavelength λ_d, as discussed in Chapter 5. For well wetted surfaces, CHF is governed by the hydrodynamic limit rather than the surface characteristics.

6.3 Summary

The findings of this chapter are summarized as that (i) adding structure on a heater surface can lift up the boiling curve and enhance the nucleate boiling heat flux by introducing more nucleation sites, (ii) adding structure can also increase the critical heat flux by improving the surface wettability, and however, (iii) critical heat flux depends on heater size and contact angle and is independent of surface topography.

CHAPTER 7

Conclusion

By boiling saturated water at one-atmosphere pressure on horizontal flat heaters of sizes less than the two-dimensional "most dangerous" Taylor wavelength but much greater than the capillary length, with different contact angles, surrounded by vessels of different sizes, and of plain and structured surfaces, the following conclusions are arrived at.

1. For well wetted surfaces, boiling curve is insensitive to heater size, but critical heat flux increases with decreasing heater size when the heater size L_c is less than the two-dimensional "most dangerous" Taylor wavelength λ_d and appears to reach an asymptotic value at $L_c/\lambda_d \approx 0.3$.

2. Hydrodynamic theory with modification overpredicts critical heat flux when the heater size L_c is less than the two-dimensional "most dangerous" Taylor wavelength λ_d. It indicates that the liquid viscosity should be considered when the vapor jet is confined.

3. Boiling curve shifts to the left with decreasing critical heat flux when the contact angle increases regardless of the heater size.

4. The heater size effect on critical heat flux is not pronounced for partially wetted surfaces where the critical heat flux is limited by the maximum vapor generation rate, which is independent of the heater size when many active nucleation sites are present.

5. Enlarging the surrounding vessel does not affect boiling curve at low heat

fluxes but increases critical heat flux. However, this enhancement degrades with increasing heater size.

6. Surface roughness/structure promotes nucleate boiling, while critical heat flux is still governed by heater size and contact angle.

7. For plain surfaces, the highest measured critical heat flux of 233 W/cm^2 or 2.11 times Zuber's critical heat flux prediction for infinite horizontal flat plates was obtained on a 1.0-cm-diameter disc of contact angle 10° surrounded by a large vessel. Adding structure on the surface reduced the contact angle to 0° and enhanced the nucleate boiling but not the critical heat flux.

Appendix A

Characterization of cartridge heaters

The four cartridge heaters used in this study are identical in dimensions and feature the same electrical behavior. Figure A.1 shows the voltage-current characteristic for one of the cartridge heaters with a zero-intercept linear fit line added. The slope, namely, the electrical resistance of the cartridge heater, is 29.17 ± 0.08 Ω, and the corresponding coefficient of determination is 1. The average electrical resistance is determined to be $R_h = 29.0 \pm 0.2$ Ω based on the characterization of all the four cartridge heaters.

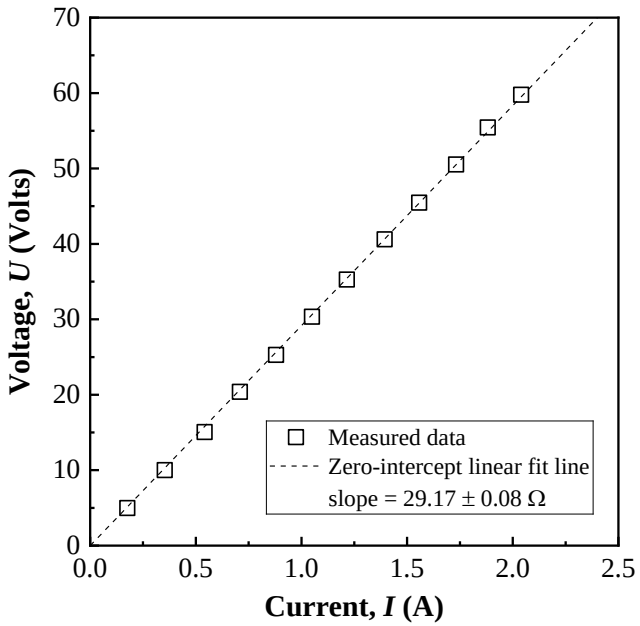

Figure A.1: Voltage-current characteristic for one of the cartridge heaters

Appendix B

Verification of linear dependences

The linear correlation between the boiling heat flux q and temperature difference (T_3–T_1), and that between the boiling heat flux q and temperature difference (T_1–T_s) declared in Chapter 3 were verified by linear regression. For demonstration, the measured temperatures and calculated boiling heat transfer data for the discs of diameters $D = 1.0$, 1.5, and 2.0 cm with contact angle $\theta = 80°$ and the ratio of heater size to surrounding vessel size $D/D_T = 1$ were used. The surface temperatures T_s and corresponding heat fluxes q for each case are tabulated in Tables C.6, C.12, and C.18 in Appendix C for reference.

Figure B.1 shows the heat flux q as a function of $k_c(T_3–T_1)/d_t$ for the discs of diameters (a) $D = 1.0$ cm, (c) $D = 1.5$ cm, and (e) $D = 2.0$ cm, and the heat flux q as a function of $(T_1–T_s)/(d/k_c + d_g/k_g)$ in (b), (d), and (f), correspondingly. A zero-intercept linear fit line is added in each figure to assess the linear correlation declared in Equation (3.13) or (3.15) and calculate the corresponding proportionality constant. As shown in Figure B.1, all the coefficients of determination are about 1, which proves the linearity. Moreover, all the proportionality constants feature fractional uncertainties less than 0.3 %, which results from the limited precision of the numerical simulation. The fractional uncertainties of the proportionality constants are much smaller compared with those of the variables in Equations (3.13) and (3.15), thus being reasonably neglected in the uncertainty analysis.

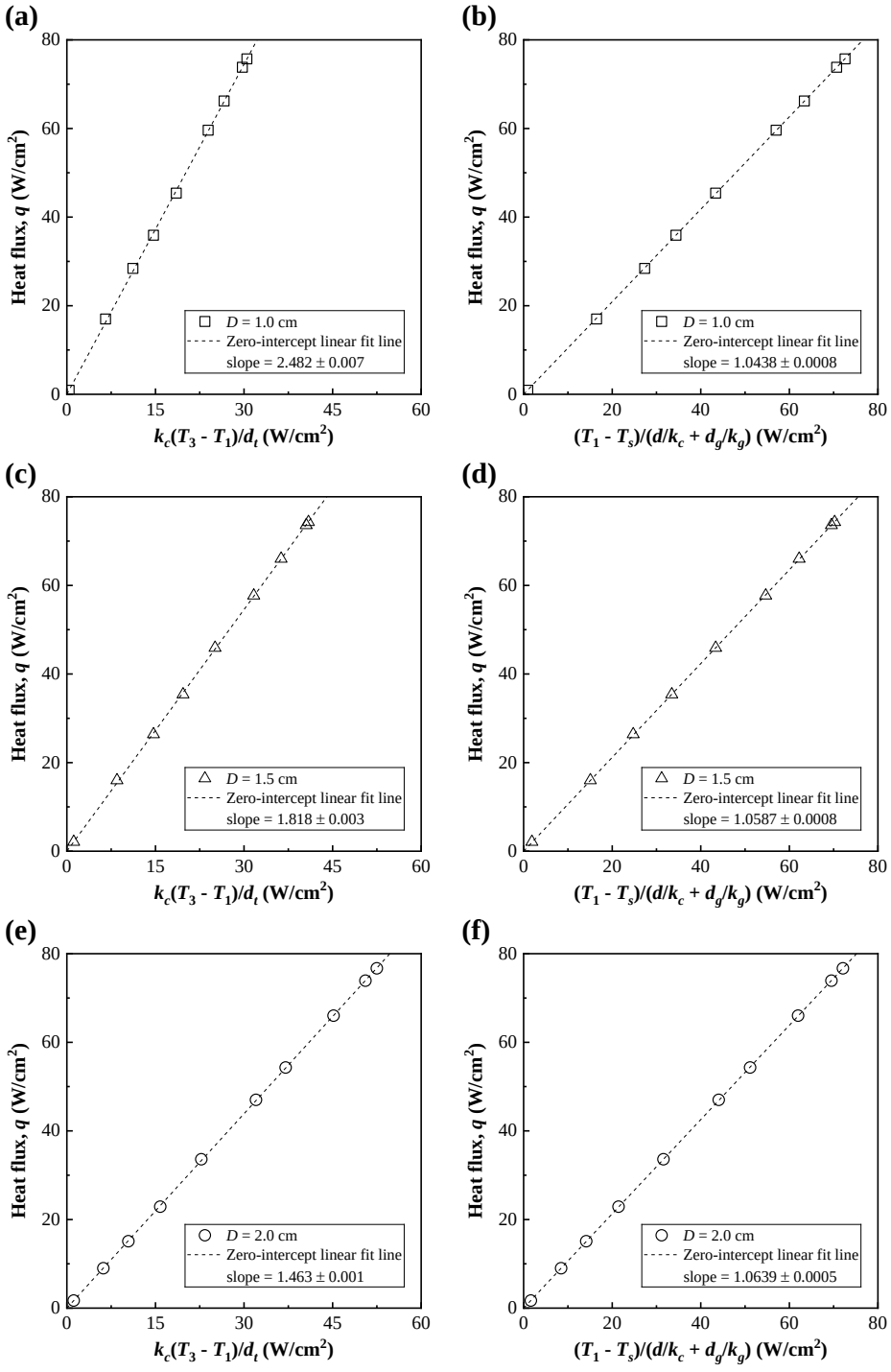

Figure B.1: Heat flux q as a function of $k_c(T_3–T_1)/d_t$ for the discs of diameters (a) $D = 1.0$ cm, (c) $D = 1.5$ cm, and (e) $D = 2.0$ cm. Heat flux q as a function of $(T_1–T_s)/(d/k_c + d_g/k_g)$ for the discs of diameters (b) $D = 1.0$ cm, (d) $D = 1.5$ cm, and (f) $D = 2.0$ cm.

Appendix C

Boiling heat transfer data

The surface temperature T_s and corresponding boiling heat flux q were calculated following the spatial temperature distribution method developed in Chapter 3 using the measured temperatures T_1, T_2, and T_3 at each steady state. The surface temperature T_s and its uncertainty δT_s were rounded to the tenths place for a higher resolution of the boiling curve, while the heat flux q and its uncertainty δq were rounded to the nearest integer in consideration of the latter magnitude. Tables C.1 to C.6, C.7 to C.12, and C.13 to C.18 summarize the boiling heat transfer data and uncertainties for the plain discs of diameters $D = 1.0$, 1.5, and 2.0 cm, respectively. Tables C.19 and C.20, C.21 and C.22, and C.23 and C.24 summarize the boiling heat transfer data and uncertainties for the structured discs of diameters $D = 1.0$, 1.5, and 2.0 cm, respectively.

Table C.1: Surface temperatures T_s and corresponding heat fluxes q for the 1.0-cm-diameter plain disc of contact angle $\theta = 10°$ surrounded by vessels of different diameters D_T

T_s (°C)	δT_s (°C)	q (W/cm^2)	δq (W/cm^2)
$D_T = 1.0$ cm			
109.0	1.1	6	3
114.7	1.3	18	3
116.5	1.4	27	3
120.5	2.0	61	4
122.9	2.5	84	5
124.7	3.1	110	6
126.8	3.8	135	7
128.6	4.4	158	9
130.6	5.0	183	10
131.7	5.4	196	10
132.8	5.5	201	11
133.2	5.6	203	11
$D_T = 2.0$ cm			
108.4	1.1	5	3
113.9	1.2	15	3
115.8	1.4	27	3
117.7	1.6	44	4
119.8	2.0	63	4
121.8	2.6	87	5
123.6	3.2	111	6
125.6	3.8	134	7
127.1	4.3	153	8
129.5	5.0	184	10
130.5	5.3	193	10
131.9	5.7	209	11
132.8	5.8	212	11
$D_T = 5.0$ cm			
105.8	1.1	1	3
111.8	1.1	11	3
114.3	1.3	20	3
116.9	1.5	37	3
118.8	1.8	53	4
120.9	2.2	71	5
123.8	2.9	99	6
125.9	3.4	121	7
128.3	4.1	146	8
130.0	4.5	163	9
132.0	5.2	188	10
133.8	5.7	209	11
134.6	6.0	219	12
135.1	6.2	228	12
135.8	6.3	233	12
$D_T = 20.0$ cm			
109.9	1.1	8	3
113.7	1.2	15	3
116.3	1.4	27	3
118.1	1.5	40	3
119.8	1.8	53	4
121.2	2.1	65	4
122.5	2.4	78	5
123.6	2.7	91	5
125.3	3.1	106	6
126.6	3.4	120	7
128.2	3.8	135	7
130.4	4.4	160	9
131.8	4.8	174	9
134.2	5.4	198	11
135.6	5.9	215	11
137.3	6.3	231	12
137.9	6.3	233	12

Table C.2: Surface temperatures T_s and corresponding heat fluxes q for the 1.0-cm-diameter plain disc of contact angle $\theta = 27°$ surrounded by vessels of different diameters D_T

T_s (°C)	δT_s (°C)	q (W/cm^2)	δq (W/cm^2)
D_T = 1.0 cm			
106.2	1.2	2	3
112.6	1.2	14	3
115.0	1.3	24	3
116.9	1.5	38	3
118.3	1.8	51	4
120.1	2.1	68	4
121.8	2.5	84	5
123.6	2.9	101	6
125.1	3.4	118	7
126.1	3.7	130	7
126.9	4.0	143	8
127.7	4.3	155	8
127.9	4.4	160	9
D_T = 2.0 cm			
107.7	1.1	4	3
113.6	1.3	18	3
116.4	1.4	35	3
117.9	1.8	51	4
119.3	2.1	64	4
120.6	2.4	78	5
121.8	2.7	90	5
123.7	3.2	111	6
125.0	3.6	128	7
125.7	3.9	139	8
127.0	4.3	154	8
128.1	4.6	166	9
128.5	4.6	168	9
D_T = 5.0 cm			
108.0	1.1	5	3
113.7	1.3	22	3
117.2	1.7	49	4
119.2	2.1	68	4
120.7	2.5	83	5
122.2	2.8	97	6
123.7	3.3	115	7
124.9	3.7	132	7
125.9	4.0	145	8
126.6	4.3	154	8
128.0	4.7	169	9
128.5	4.8	176	9
129.1	5.1	184	10
129.8	5.2	190	10
D_T = 20.0 cm			
109.0	1.1	8	3
113.5	1.3	23	3
115.7	1.5	39	3
117.1	1.7	50	4
119.0	2.1	65	4
121.0	2.5	83	5
123.1	3.0	105	6
124.6	3.4	120	7
126.3	3.9	138	8
127.8	4.3	154	8
129.5	4.8	173	9
130.5	5.0	184	10
130.7	5.2	188	10

Table C.3: Surface temperatures T_s and corresponding heat fluxes q for the 1.0-cm-diameter plain disc of contact angle $\theta = 43°$ surrounded by vessels of different diameters D_T

T_s (°C)	δT_s (°C)	q (W/cm^2)	δq (W/cm^2)
D_T = 1.0 cm			
108.4	1.1	6	3
110.6	1.1	10	3
113.6	1.3	23	3
116.5	1.6	45	4
117.9	1.9	57	4
119.5	2.2	70	5
120.6	2.4	80	5
122.0	2.7	93	6
123.6	3.1	108	6
124.6	3.4	119	7
125.2	3.5	125	7
125.3	3.6	127	7
D_T = 2.0 cm			
107.9	1.1	5	3
112.0	1.3	17	3
115.1	1.5	39	3
116.7	1.8	51	4
118.7	2.0	63	4
120.1	2.3	77	5
121.3	2.6	89	5
122.5	2.9	100	6
123.8	3.2	114	6
124.9	3.6	126	7
125.6	3.8	133	7
126.3	3.9	139	8
D_T = 5.0 cm			
110.0	1.2	10	3
112.6	1.3	21	3
115.8	1.5	41	3
117.4	1.8	54	4
119.1	2.2	72	5
120.5	2.6	86	5
121.8	2.9	101	6
122.8	3.2	114	6
123.5	3.6	126	7
125.1	4.0	144	8
125.2	4.0	145	8
D_T = 20.0 cm			
108.4	1.1	7	3
111.6	1.3	19	3
114.7	1.6	42	3
116.6	1.9	55	4
118.5	2.2	69	4
120.1	2.5	84	5
121.4	2.9	99	6
122.9	3.3	115	7
124.9	3.9	138	8
125.9	4.2	149	8
126.2	4.2	152	8

Table C.4: Surface temperatures T_s and corresponding heat fluxes q for the 1.0-cm-diameter plain disc of contact angle $\theta = 54°$ surrounded by vessels of different diameters D_T

T_s (°C)	δT_s (°C)	q (W/cm^2)	δq (W/cm^2)
D_T = 1.0 cm			
110.1	1.1	11	3
113.8	1.4	29	3
115.6	1.6	44	3
117.1	1.9	56	4
118.1	2.1	64	4
119.7	2.4	79	5
121.3	2.8	96	6
122.7	3.1	110	6
122.8	3.2	111	6
D_T = 2.0 cm			
110.6	1.2	12	3
114.3	1.4	35	3
116.6	1.8	52	4
117.9	2.1	65	4
120.1	2.6	89	5
121.3	3.0	102	6
122.2	3.3	114	6
122.4	3.4	119	7
D_T = 5.0 cm			
106.0	1.2	3	3
111.0	1.3	17	3
114.1	1.5	37	3
115.0	1.6	45	4
117.0	2.0	62	4
118.6	2.5	84	5
120.1	2.9	101	6
121.3	3.3	114	6
122.6	3.6	127	7
123.2	3.6	129	7
D_T = 20.0 cm			
109.0	1.1	9	3
112.2	1.3	26	3
114.8	1.7	48	4
116.5	2.1	64	4
117.9	2.4	79	5
119.8	2.8	97	6
121.4	3.2	113	6
122.8	3.6	128	7
123.3	3.7	131	7

Table C.5: Surface temperatures T_s and corresponding heat fluxes q for the 1.0-cm-diameter plain disc of contact angle $\theta = 65°$ surrounded by vessels of different diameters D_T

T_s (°C)	δT_s (°C)	q (W/cm^2)	δq (W/cm^2)
D_T = 1.0 cm			
107.5	1.1	4	3
110.4	1.2	15	3
112.0	1.3	26	3
113.8	1.5	39	3
114.2	1.6	43	3
115.6	1.9	58	4
116.7	2.2	70	5
117.6	2.4	80	5
118.5	2.7	92	5
118.7	2.7	93	6
D_T = 2.0 cm			
108.3	1.1	6	3
110.0	1.2	12	3
111.3	1.3	21	3
113.7	1.5	39	3
115.3	1.8	52	4
117.1	2.1	68	4
118.3	2.4	79	5
119.3	2.7	92	5
119.7	2.9	98	6
120.0	2.9	99	6
D_T = 5.0 cm			
107.9	1.1	5	3
110.4	1.3	17	3
112.0	1.4	28	3
113.6	1.6	42	3
114.9	1.9	55	4
116.3	2.1	68	4
117.6	2.4	80	5
118.8	2.7	93	6
119.7	2.9	101	6
120.3	3.0	105	6
D_T = 20.0 cm			
108.7	1.1	7	3
110.5	1.2	16	3
112.4	1.4	29	3
113.6	1.5	41	3
114.5	1.7	50	4
115.5	2.0	62	4
116.6	2.3	76	5
117.5	2.6	87	5
118.5	2.9	99	6
119.3	3.0	103	6

Table C.6: Surface temperatures T_s and corresponding heat fluxes q for the 1.0-cm-diameter plain disc of contact angle $\theta = 80°$ surrounded by vessels of different diameters D_T

T_s (°C)	δT_s (°C)	q (W/cm^2)	δq (W/cm^2)
D_T = 1.0 cm			
105.3	1.1	1	3
110.5	1.3	17	3
112.2	1.4	28	3
113.2	1.5	36	3
114.2	1.6	45	4
115.7	2.0	60	4
116.4	2.1	66	4
117.1	2.3	74	5
117.4	2.3	76	5
D_T = 2.0 cm			
107.0	1.1	5	3
110.0	1.2	15	3
111.8	1.4	30	3
113.3	1.6	44	3
114.5	1.9	58	4
115.7	2.2	69	4
116.4	2.4	79	5
116.6	2.5	81	5
D_T = 5.0 cm			
107.6	1.1	5	3
109.8	1.2	12	3
111.9	1.4	30	3
113.1	1.6	44	4
114.4	1.9	57	4
115.7	2.2	72	5
116.7	2.5	82	5
117.2	2.6	88	5
D_T = 20.0 cm			
107.3	1.1	7	3
109.2	1.1	11	3
111.8	1.4	28	3
113.5	1.5	41	3
115.8	2.0	60	4
117.5	2.3	75	5
118.7	2.6	85	5
119.1	2.6	88	5

Table C.7: Surface temperatures T_s and corresponding heat fluxes q for the 1.5-cm-diameter plain disc of contact angle $\theta = 12°$ surrounded by vessels of different diameters D_T

T_s (°C)	δT_s (°C)	q (W/cm^2)	δq (W/cm^2)
D_T = 1.5 cm			
109.3	0.8	6	2
114.6	1.0	20	2
117.0	1.2	35	3
118.9	1.5	49	3
121.3	2.0	70	4
122.7	2.5	89	5
124.6	3.0	110	6
126.3	3.5	129	7
127.8	4.0	148	8
130.2	4.6	170	9
131.0	4.8	178	9
131.2	4.8	181	10
D_T = 3.0 cm			
111.5	0.9	8	2
115.4	1.0	24	2
117.8	1.4	40	3
119.3	1.7	54	3
120.8	2.0	69	4
121.4	2.2	76	4
123.1	2.7	97	5
123.9	3.0	108	6
126.2	3.7	136	7
126.9	4.0	149	8
127.9	4.5	166	9
129.9	4.8	181	10
131.6	5.1	192	10
131.6	5.2	195	10
D_T = 7.5 cm			
110.1	0.8	6	2
113.1	0.9	13	2
116.5	1.2	34	3
119.8	1.8	60	4
121.7	2.3	82	5
124.7	3.2	117	6
126.5	3.7	136	7
128.3	4.2	156	8
130.0	4.8	180	10
131.5	5.2	196	10
132.7	5.7	213	11
133.0	5.8	218	11
D_T = 20.0 cm			
109.7	0.8	5	2
113.1	0.9	13	2
118.8	1.5	49	3
120.4	1.8	60	4
122.8	2.3	82	5
124.5	2.7	98	5
126.4	3.2	117	6
128.5	3.7	136	7
130.1	4.2	157	8
132.7	4.8	180	10
134.3	5.2	196	10
135.2	5.6	211	11
135.2	5.7	215	11
134.8	5.8	218	11

Table C.8: Surface temperatures T_s and corresponding heat fluxes q for the 1.5-cm-diameter plain disc of contact angle $\theta = 27°$ surrounded by vessels of different diameters D_T

T_s (°C)	δT_s (°C)	q (W/cm^2)	δq (W/cm^2)
$D_T = 1.5$ cm			
111.1	0.9	11	2
115.0	1.1	27	2
116.7	1.3	38	3
118.1	1.6	51	3
120.1	2.0	68	4
121.6	2.4	86	5
123.1	2.7	99	5
124.3	3.1	113	6
125.7	3.5	131	7
127.2	3.9	146	8
127.3	4.1	152	8
$D_T = 3.0$ cm			
113.0	1.0	18	2
115.3	1.1	29	2
116.8	1.3	38	3
120.0	2.0	68	4
121.3	2.3	81	5
122.4	2.6	95	5
123.1	2.8	103	6
123.6	3.0	108	6
125.0	3.4	125	7
126.1	3.8	140	8
126.3	4.1	154	8
126.0	4.3	159	8
$D_T = 7.5$ cm			
109.8	0.8	8	2
115.3	1.1	28	2
117.5	1.4	44	3
119.1	1.8	59	4
120.8	2.2	79	5
122.1	2.6	95	5
122.9	2.9	105	6
123.9	3.3	120	7
125.4	3.8	140	7
125.8	3.9	144	8
126.2	4.1	153	8
126.9	4.4	165	9
127.3	4.5	169	9
$D_T = 20.0$ cm			
112.4	0.9	16	2
115.4	1.1	31	3
117.8	1.5	49	3
119.3	1.9	64	4
120.9	2.3	83	5
122.3	2.7	97	5
123.9	3.2	115	6
125.6	3.6	134	7
127.0	4.0	149	8
128.3	4.4	163	9
128.4	4.6	170	9

Table C.9: Surface temperatures T_s and corresponding heat fluxes q for the 1.5-cm-diameter plain disc of contact angle $\theta = 37°$ surrounded by vessels of different diameters D_T

T_s (°C)	δT_s (°C)	q (W/cm^2)	δq (W/cm^2)
D_T = 1.5 cm			
110.5	0.9	10	2
113.2	1.0	20	2
115.4	1.3	36	3
117.5	1.6	52	3
119.2	1.9	67	4
120.0	2.1	75	4
121.4	2.4	87	5
123.1	2.9	105	6
124.1	3.2	117	6
125.1	3.5	127	7
125.1	3.5	131	7
D_T = 3.0 cm			
110.2	0.8	9	2
113.3	1.0	23	2
116.4	1.4	45	3
118.2	1.8	59	4
119.5	2.1	74	4
120.8	2.5	88	5
121.9	2.8	100	6
123.3	3.1	115	6
124.2	3.4	127	7
125.4	3.7	138	7
125.6	3.8	141	8
D_T = 7.5 cm			
110.9	0.9	13	2
112.8	1.0	22	2
114.6	1.2	32	3
116.0	1.4	44	3
117.4	1.7	58	4
118.8	2.1	72	4
120.1	2.4	85	5
121.1	2.6	94	5
121.9	2.8	102	6
123.4	3.2	118	6
124.4	3.6	132	7
125.2	3.8	142	8
125.6	4.0	147	8
D_T = 20.0 cm			
107.8	0.8	4	2
112.2	1.0	20	2
114.9	1.3	36	3
117.2	1.7	55	3
118.8	2.1	72	4
120.5	2.5	91	5
122.3	3.0	108	6
123.0	3.1	115	6
124.2	3.4	126	7
125.2	3.5	131	7
125.3	3.9	145	8
125.6	4.0	149	8

Table C.10: Surface temperatures T_s and corresponding heat fluxes q for the 1.5-cm-diameter plain disc of contact angle $\theta = 53°$ surrounded by vessels of different diameters D_T

T_s (°C)	δT_s (°C)	q (W/cm^2)	δq (W/cm^2)
D_T = 1.5 cm			
108.9	0.8	8	2
112.1	1.0	20	2
114.6	1.4	40	3
116.3	1.6	54	3
117.7	2.0	69	4
119.0	2.3	81	5
119.8	2.6	93	5
120.6	2.9	104	6
121.0	2.9	107	6
D_T = 3.0 cm			
109.2	0.9	8	2
112.2	1.0	19	2
114.4	1.2	34	3
116.2	1.5	49	3
117.8	1.9	63	4
118.9	2.1	73	4
119.9	2.4	84	5
121.0	2.7	97	5
121.4	3.0	110	6
121.2	3.1	113	6
D_T = 7.5 cm			
110.9	0.9	12	2
113.7	1.0	25	2
115.1	1.3	38	3
116.9	1.7	54	3
118.1	2.0	68	4
119.2	2.2	76	4
120.1	2.5	88	5
122.0	3.0	110	6
122.5	3.3	120	7
122.8	3.3	122	7
D_T = 20.0 cm			
107.4	0.8	5	2
111.9	1.0	17	2
114.9	1.2	35	3
116.9	1.7	54	3
118.6	2.1	74	4
119.8	2.5	90	5
120.7	2.9	106	6
121.2	3.0	111	6
121.3	3.2	119	6
121.2	3.3	122	7

Table C.11: Surface temperatures T_s and corresponding heat fluxes q for the 1.5-cm-diameter plain disc of contact angle $\theta = 63°$ surrounded by vessels of different diameters D_T

T_s (°C)	δT_s (°C)	q (W/cm^2)	δq (W/cm^2)
D_T = 1.5 cm			
108.0	0.8	7	2
110.7	1.0	17	2
112.3	1.1	26	2
113.9	1.3	38	3
114.5	1.4	45	3
115.9	1.7	55	3
117.0	1.9	65	4
117.8	2.1	74	4
118.8	2.4	84	5
119.2	2.6	92	5
119.3	2.6	92	5
D_T = 3.0 cm			
105.0	0.9	1	2
107.5	0.8	6	2
109.6	0.9	13	2
111.4	1.0	22	2
113.2	1.2	33	3
115.1	1.5	47	3
116.4	1.7	58	4
117.5	2.0	70	4
119.0	2.3	83	5
120.1	2.6	95	5
120.2	2.7	97	5
120.4	2.7	97	5
D_T = 7.5 cm			
108.6	0.9	8	2
111.5	1.0	24	2
113.3	1.2	35	3
114.3	1.4	42	3
115.3	1.6	52	3
116.6	1.9	64	4
118.1	2.1	75	4
119.2	2.5	90	5
119.6	2.7	97	5
120.1	2.9	104	6
119.7	2.9	104	6
D_T = 20.0 cm			
107.5	0.8	6	2
110.9	1.0	18	2
112.6	1.1	29	2
113.9	1.3	40	3
114.8	1.5	49	3
115.9	1.8	59	4
117.2	2.1	72	4
118.2	2.3	83	5
119.2	2.6	95	5
119.9	2.8	102	6
119.5	2.9	104	6

Table C.12: Surface temperatures T_s and corresponding heat fluxes q for the 1.5-cm-diameter plain disc of contact angle $\theta = 80°$ surrounded by vessels of different diameters D_T

T_s (°C)	δT_s (°C)	q (W/cm^2)	δq (W/cm^2)
D_T = 1.5 cm			
105.8	0.8	2	2
110.2	0.9	16	2
111.7	1.1	26	2
113.0	1.2	35	3
114.2	1.5	46	3
115.4	1.7	58	4
116.4	1.9	66	4
117.0	2.1	74	4
117.2	2.1	74	4
D_T = 3.0 cm			
108.8	0.9	11	2
110.7	1.0	23	2
111.9	1.2	31	3
113.3	1.4	43	3
114.4	1.6	54	3
115.6	1.9	65	4
116.5	2.1	73	4
116.5	2.2	79	5
D_T = 7.5 cm			
107.0	0.8	5	2
109.9	0.9	16	2
111.7	1.1	30	3
113.1	1.4	40	3
114.4	1.6	51	3
115.4	1.8	61	4
116.3	2.0	71	4
117.1	2.3	81	5
116.4	2.3	83	5
D_T = 20.0 cm			
104.8	0.8	2	2
108.2	0.8	9	2
109.6	0.9	16	2
111.4	1.1	29	2
112.7	1.3	38	3
114.2	1.6	52	3
115.4	1.8	63	4
116.5	2.1	72	4
117.0	2.3	80	5
117.2	2.3	83	5

Table C.13: Surface temperatures T_s and corresponding heat fluxes q for the 2.0-cm-diameter plain disc of contact angle $\theta = 12°$ surrounded by vessels of different diameters D_T

T_s (°C)	δT_s (°C)	q (W/cm^2)	δq (W/cm^2)
D_T = 2.0 cm			
105.6	0.7	1	2
110.3	0.7	7	2
115.1	0.9	21	2
116.4	1.0	29	2
118.1	1.3	41	3
119.2	1.4	48	3
120.1	1.6	56	3
121.3	1.8	66	4
123.1	2.2	78	4
124.8	2.5	91	5
125.8	2.7	99	5
127.1	2.9	109	6
129.0	3.3	122	7
130.8	3.7	138	7
131.3	3.8	142	7
132.0	3.8	143	8
D_T = 4.0 cm			
106.1	0.7	2	2
109.8	0.7	6	2
114.2	0.8	17	2
115.6	0.9	25	2
117.2	1.1	34	2
118.7	1.3	44	3
119.7	1.5	51	3
121.2	1.8	63	4
123.1	2.1	77	4
124.1	2.3	85	5
125.4	2.6	95	5
127.0	2.9	107	6
128.9	3.3	124	7
129.5	3.5	130	7
130.6	3.7	140	7
131.7	4.0	151	8
132.2	4.0	151	8
D_T = 10.0 cm			
108.6	0.7	4	2
110.9	0.7	8	2
114.6	0.8	19	2
117.0	1.0	28	2
118.9	1.2	38	3
121.3	1.5	50	3
123.7	1.9	66	4
125.2	2.2	78	4
127.7	2.7	98	5
129.4	3.0	113	6
130.4	3.3	123	7
131.5	3.6	135	7
132.2	3.8	144	8
133.3	4.0	149	8
133.5	4.0	151	8
D_T = 20.0 cm			
107.3	0.7	3	2
111.2	0.7	8	2
113.2	0.7	12	2
115.9	0.9	21	2
118.2	1.1	32	2
119.9	1.2	40	3
122.0	1.6	56	3
124.0	1.9	69	4
125.9	2.3	85	5
127.6	2.6	97	5
129.2	3.0	113	6
130.3	3.3	123	7
131.3	3.6	136	7
132.5	4.0	150	8

Table C.14: Surface temperatures T_s and corresponding heat fluxes q for the 2.0-cm-diameter plain disc of contact angle $\theta = 24°$ surrounded by vessels of different diameters D_T

T_s (°C)	δT_s (°C)	q (W/cm^2)	δq (W/cm^2)
D_T = 2.0 cm			
107.0	0.7	3	2
110.4	0.7	7	2
114.1	0.8	17	2
116.5	1.1	31	2
118.2	1.3	43	3
119.6	1.5	53	3
121.5	1.9	69	4
122.4	2.2	80	4
123.8	2.6	96	5
124.3	2.8	103	6
124.9	3.0	110	6
125.4	3.2	118	6
126.3	3.4	126	7
127.1	3.6	133	7
127.4	3.6	136	7
D_T = 4.0 cm			
109.0	0.7	5	2
111.4	0.7	8	2
113.8	0.8	16	2
116.2	1.0	30	2
118.2	1.3	43	3
119.4	1.6	54	3
120.7	1.9	67	4
121.5	2.0	73	4
121.9	2.2	81	4
122.6	2.4	89	5
123.5	2.8	102	5
124.2	3.0	113	6
125.1	3.3	123	7
125.9	3.6	133	7
126.0	3.6	137	7
D_T = 10.0 cm			
108.0	0.7	4	2
112.0	0.8	11	2
116.3	1.1	32	2
117.9	1.3	44	3
118.5	1.5	50	3
120.2	1.9	67	4
121.1	2.1	76	4
121.8	2.3	86	5
122.6	2.6	94	5
123.3	2.8	102	5
124.3	3.0	113	6
125.2	3.2	121	6
126.6	3.5	132	7
127.1	3.6	134	7
D_T = 20.0 cm			
106.5	0.7	2	2
111.4	0.8	10	2
112.8	0.7	14	2
114.9	0.9	23	2
116.5	1.1	32	2
118.4	1.3	43	3
119.3	1.5	51	3
120.3	1.7	60	3
121.1	2.0	70	4
122.1	2.2	80	4
123.0	2.5	92	5
123.8	2.7	101	5
124.7	3.1	114	6
125.6	3.4	126	7
126.6	3.6	133	7
127.1	3.6	135	7

Table C.15: Surface temperatures T_s and corresponding heat fluxes q for the 2.0-cm-diameter plain disc of contact angle $\theta = 39°$ surrounded by vessels of different diameters D_T

T_s (°C)	δT_s (°C)	q (W/cm^2)	δq (W/cm^2)
D_T = 2.0 cm			
108.3	0.7	6	2
112.3	0.8	17	2
114.5	1.0	30	2
115.9	1.3	41	3
116.7	1.4	48	3
117.7	1.6	56	3
118.4	1.8	63	4
119.5	2.0	71	4
120.4	2.2	80	4
121.5	2.5	91	5
122.5	2.8	103	6
123.3	3.0	113	6
123.4	3.1	116	6
D_T = 4.0 cm			
110.1	0.8	10	2
112.7	0.8	19	2
114.1	0.9	24	2
115.6	1.1	36	2
116.5	1.3	44	3
117.8	1.6	55	3
118.6	1.8	62	4
119.5	2.0	70	4
119.9	2.0	73	4
121.9	2.5	91	5
122.9	2.7	100	5
123.7	3.0	110	6
124.0	3.1	115	6
D_T = 10.0 cm			
109.1	0.7	8	2
111.7	0.8	17	2
113.1	0.9	22	2
114.4	1.1	31	2
115.6	1.3	43	3
116.9	1.6	54	3
118.0	1.8	62	4
119.2	2.1	76	4
120.7	2.5	90	5
121.8	2.7	101	5
122.9	3.0	110	6
123.3	3.2	118	6
124.0	3.1	116	6
D_T = 20.0 cm			
105.6	0.7	3	2
110.8	0.7	12	2
112.6	0.8	17	2
113.5	0.9	24	2
115.0	1.1	33	2
116.5	1.3	43	3
117.4	1.5	50	3
118.7	1.6	58	3
120.1	1.9	68	4
121.1	2.1	77	4
121.8	2.3	85	5
123.0	2.5	93	5
123.6	2.7	100	5
123.9	2.9	109	6
124.3	3.1	114	6
124.5	3.2	119	6

Table C.16: Surface temperatures T_s and corresponding heat fluxes q for the 2.0-cm-diameter plain disc of contact angle $\theta = 51°$ surrounded by vessels of different diameters D_T

T_s (°C)	δT_s (°C)	q (W/cm^2)	δq (W/cm^2)
$D_T = 2.0$ cm			
107.6	0.7	3	2
110.7	0.7	12	2
112.5	0.9	21	2
114.0	1.1	31	2
115.4	1.5	49	3
116.3	1.7	60	3
117.1	2.0	70	4
118.0	2.2	78	4
118.9	2.4	90	5
119.3	2.6	96	5
120.0	2.7	101	5
120.4	2.8	103	6
$D_T = 4.0$ cm			
107.8	0.7	3	2
110.3	0.8	11	2
111.7	0.8	17	2
113.5	1.0	30	2
114.3	1.2	38	3
115.1	1.5	49	3
116.1	1.7	60	3
117.0	2.0	70	4
117.8	2.2	78	4
118.8	2.5	91	5
119.1	2.6	94	5
120.1	2.8	103	6
120.5	2.9	108	6
$D_T = 10.0$ cm			
106.3	0.7	2	2
110.0	0.7	10	2
113.0	0.9	26	2
113.6	1.1	32	2
114.4	1.3	41	3
115.9	1.6	54	3
116.7	1.7	61	4
117.5	2.0	70	4
118.7	2.2	81	4
119.4	2.4	88	5
120.4	2.6	97	5
120.8	2.7	100	5
121.1	2.8	104	6
$D_T = 20.0$ cm			
106.1	0.7	2	2
108.6	0.7	6	2
109.8	0.8	10	2
111.1	0.8	15	2
112.5	0.9	23	2
113.6	1.1	31	2
114.8	1.3	41	3
116.0	1.5	52	3
117.1	1.7	60	3
118.2	2.0	71	4
119.3	2.3	82	5
120.1	2.5	90	5
121.0	2.7	99	5
121.5	2.8	105	6

Table C.17: Surface temperatures T_s and corresponding heat fluxes q for the 2.0-cm-diameter plain disc of contact angle $\theta = 60°$ surrounded by vessels of different diameters D_T

T_s (°C)	δT_s (°C)	q (W/cm^2)	δq (W/cm^2)
D_T = 2.0 cm			
107.2	0.7	4	2
109.0	0.7	10	2
110.9	0.8	17	2
112.6	1.0	27	2
113.9	1.2	37	2
114.8	1.3	45	3
116.0	1.6	54	3
117.2	1.8	64	4
118.0	2.0	72	4
119.0	2.2	82	5
119.5	2.4	87	5
120.2	2.5	92	5
D_T = 4.0 cm			
105.8	0.7	2	2
107.5	0.7	5	2
109.4	0.8	11	2
111.4	0.9	21	2
113.0	1.0	29	2
114.9	1.3	42	3
116.0	1.5	51	3
116.9	1.8	63	4
118.7	2.1	74	4
120.3	2.4	88	5
120.4	2.6	95	5
120.4	2.6	97	5
D_T = 10.0 cm			
106.1	0.7	2	2
108.3	0.7	9	2
110.4	0.8	17	2
111.9	0.9	26	2
113.5	1.2	37	2
114.4	1.3	42	3
115.5	1.5	52	3
116.8	1.8	63	4
118.7	2.0	73	4
119.3	2.4	89	5
119.6	2.6	95	5
120.2	2.6	97	5
D_T = 20.0 cm			
107.4	0.7	5	2
109.3	0.7	10	2
111.2	0.8	19	2
112.8	1.0	27	2
114.1	1.2	36	2
114.9	1.3	43	3
116.3	1.5	53	3
117.8	1.8	64	4
118.9	2.0	73	4
119.8	2.2	82	5
120.3	2.5	92	5
120.9	2.6	97	5

Table C.18: Surface temperatures T_s and corresponding heat fluxes q for the 2.0-cm-diameter plain disc of contact angle $\theta = 80°$ surrounded by vessels of different diameters D_T

T_s (°C)	δT_s (°C)	q (W/cm^2)	δq (W/cm^2)
D_T = 2.0 cm			
105.0	0.7	2	2
107.9	0.7	9	2
109.5	0.8	15	2
111.2	0.9	23	2
112.7	1.1	34	2
114.0	1.4	47	3
114.7	1.6	54	3
116.2	1.9	66	4
116.8	2.1	74	4
117.3	2.1	77	4
D_T = 4.0 cm			
105.4	0.7	2	2
109.7	0.8	16	2
111.4	1.0	26	2
112.5	1.1	34	2
113.5	1.3	42	3
114.3	1.5	49	3
115.0	1.6	56	3
115.4	1.7	59	3
116.0	1.9	66	4
116.7	2.1	75	4
117.1	2.2	78	4
117.2	2.2	82	5
D_T = 10.0 cm			
107.1	0.7	6	2
109.7	0.8	17	2
111.8	1.0	29	2
113.1	1.2	38	3
114.0	1.4	45	3
115.1	1.6	55	3
116.2	1.8	64	4
117.0	2.0	71	4
117.9	2.2	80	4
118.1	2.3	82	5
D_T = 20.0 cm			
107.1	0.7	6	2
108.8	0.7	12	2
110.4	0.8	20	2
112.3	1.0	29	2
113.3	1.2	36	2
114.3	1.4	45	3
115.4	1.5	53	3
116.1	1.7	61	4
117.2	2.0	73	4
118.1	2.2	78	4
117.8	2.2	82	5

Table C.19: Surface temperatures T_s and corresponding heat fluxes q for the 1.0-cm-diameter structured disc of contact angle $\theta = 0°$ surrounded by vessels of different diameters D_T

T_s (°C)	δT_s (°C)	q (W/cm^2)	δq (W/cm^2)
$D_T = 1.0$ cm			
108.6	1.2	14	3
113.0	1.4	32	3
115.3	1.8	53	4
117.1	2.2	69	4
118.5	2.6	87	5
119.8	3.1	108	6
121.7	3.7	131	7
123.2	4.3	155	8
124.4	4.8	174	9
125.5	5.2	188	10
125.9	5.4	199	11
126.3	5.6	205	11
$D_T = 2.0$ cm			
109.6	1.3	16	3
112.3	1.3	28	3
114.8	1.8	53	4
116.9	2.3	75	5
118.3	2.7	93	6
119.8	3.2	114	6
120.9	3.6	129	7
122.1	4.1	146	8
123.5	4.6	167	9
124.6	5.2	188	10
125.3	5.6	206	11
126.1	5.8	211	11
$D_T = 5.0$ cm			
109.9	1.2	19	3
113.7	1.6	40	3
115.7	1.9	55	4
117.2	2.3	77	5
118.5	2.9	98	6
119.8	3.4	119	7
120.9	3.8	136	8
121.3	4.4	160	9
122.7	4.9	176	9
124.0	5.3	194	10
124.8	5.8	211	11
125.4	5.8	213	11
126.0	6.2	226	12
126.1	6.2	227	12
127.2	6.4	236	12
$D_T = 20.0$ cm			
108.5	1.2	13	3
111.0	1.2	20	3
114.1	1.6	44	4
115.8	2.0	60	4
116.7	2.3	74	5
117.9	2.8	96	6
119.4	3.4	119	7
120.5	3.9	140	8
122.4	4.5	164	9
123.6	5.1	185	10
124.7	5.5	201	11
125.6	5.9	217	12
126.3	6.2	226	12
127.0	6.2	229	12

Table C.20: Surface temperatures T_s and corresponding heat fluxes q for the 1.0-cm-diameter structured disc of contact angle $\theta = 66°$ surrounded by vessels of different diameters D_T

T_s (°C)	δT_s (°C)	q (W/cm^2)	δq (W/cm^2)
$D_T = 1.0$ cm			
105.2	1.0	5	3
108.0	1.2	16	3
110.8	1.4	32	3
112.1	1.7	49	4
113.2	2.1	67	4
113.7	2.3	74	5
114.7	2.7	90	5
114.5	2.8	96	6
115.2	2.8	96	6
$D_T = 2.0$ cm			
106.4	1.2	8	3
108.6	1.3	23	3
110.8	1.5	39	3
112.3	1.9	57	4
113.4	2.3	73	5
114.2	2.6	89	5
114.4	2.9	99	6
114.9	3.0	102	6
$D_T = 5.0$ cm			
106.2	1.2	7	3
108.4	1.2	20	3
111.1	1.6	42	3
113.0	2.0	60	4
114.0	2.3	73	5
114.6	2.7	92	5
114.9	2.9	99	6
115.3	2.9	100	6
$D_T = 20.0$ cm			
106.5	1.2	8	3
108.5	1.2	20	3
110.4	1.5	36	3
111.5	1.8	51	4
112.9	2.1	66	4
113.6	2.5	82	5
114.3	2.8	97	6
114.9	2.9	101	6

Table C.21: Surface temperatures T_s and corresponding heat fluxes q for the 1.5-cm-diameter structured disc of contact angle $\theta = 0°$ surrounded by vessels of different diameters D_T

T_s (°C)	δT_s (°C)	q (W/cm^2)	δq (W/cm^2)
$D_T = 1.5$ cm			
107.7	0.9	10	2
111.5	1.0	22	2
113.7	1.3	40	3
115.8	1.7	57	4
117.2	2.2	78	4
118.1	2.6	95	5
119.4	3.1	112	6
120.7	3.5	129	7
121.7	4.0	148	8
122.6	4.4	164	9
123.5	4.9	181	10
124.1	5.1	190	10
$D_T = 3.0$ cm			
109.5	0.9	13	2
110.4	0.9	15	2
112.8	1.2	32	3
115.2	1.5	49	3
116.7	1.9	65	4
117.1	2.1	74	4
117.9	2.4	86	5
119.4	2.9	104	6
120.7	3.4	124	7
121.7	3.9	145	8
123.0	4.4	165	9
123.9	5.0	185	10
124.7	5.4	201	11
$D_T = 7.5$ cm			
109.9	0.9	17	2
111.5	1.1	26	2
113.7	1.4	44	3
115.4	1.8	60	4
117.0	2.3	82	5
118.4	2.9	104	6
119.8	3.5	128	7
120.8	3.9	145	8
121.9	4.4	165	9
122.9	4.8	180	10
123.9	5.4	204	11
124.2	5.6	211	11
$D_T = 20.0$ cm			
110.2	1.0	18	2
112.7	1.2	33	3
115.1	1.6	54	3
116.4	2.1	72	4
117.4	2.5	90	5
118.5	3.0	108	6
119.8	3.5	130	7
121.0	4.0	148	8
121.8	4.5	169	9
122.9	5.0	188	10
124.0	5.6	210	11
124.8	5.8	219	11

Table C.22: Surface temperatures T_s and corresponding heat fluxes q for the 1.5-cm-diameter structured disc of contact angle $\theta = 66°$ surrounded by vessels of different diameters D_T

T_s (°C)	δT_s (°C)	q (W/cm^2)	δq (W/cm^2)
$D_T = 1.5$ cm			
106.0	0.9	6	2
107.8	0.9	15	2
109.8	1.2	30	3
111.2	1.4	43	3
112.5	1.7	56	4
113.0	2.0	71	4
114.1	2.4	84	5
114.4	2.6	94	5
114.6	2.6	95	5
$D_T = 3.0$ cm			
105.8	0.8	5	2
107.4	0.9	11	2
109.2	1.0	23	2
110.9	1.3	36	3
111.7	1.5	47	3
112.7	1.7	56	4
113.7	2.0	71	4
114.2	2.4	84	5
115.3	2.7	96	5
115.4	2.7	99	5
$D_T = 7.5$ cm			
106.3	0.9	6	2
108.1	0.9	14	2
109.3	1.0	20	2
110.9	1.2	32	3
112.2	1.4	43	3
112.8	1.6	53	3
113.8	1.9	64	4
114.4	2.2	77	4
114.9	2.5	91	5
115.4	2.7	99	5
$D_T = 20.0$ cm			
106.8	0.9	8	2
108.7	0.9	18	2
110.6	1.2	31	3
111.7	1.4	43	3
112.9	1.7	56	4
113.4	1.9	67	4
114.2	2.3	79	5
115.0	2.5	90	5
115.5	2.7	99	5
115.4	2.8	100	6

Table C.23: Surface temperatures T_s and corresponding heat fluxes q for the 2.0-cm-diameter structured disc of contact angle $\theta = 0°$ surrounded by vessels of different diameters D_T

T_s (°C)	δT_s (°C)	q (W/cm^2)	δq (W/cm^2)
$D_T = 2.0$ cm			
107.0	0.7	3	2
109.6	0.8	13	2
112.1	1.0	26	2
113.9	1.2	40	3
115.0	1.5	51	3
116.0	1.8	63	4
117.3	2.2	81	4
118.3	2.6	96	5
119.3	2.9	108	6
119.8	3.2	119	6
120.5	3.4	127	7
121.1	3.6	134	7
121.6	3.8	142	8
$D_T = 4.0$ cm			
106.9	0.7	3	2
110.3	0.8	15	2
112.9	1.1	33	2
114.8	1.4	49	3
116.0	1.7	60	3
117.2	2.1	74	4
118.3	2.4	87	5
119.3	2.8	104	6
120.4	3.2	119	6
121.1	3.6	134	7
121.2	3.8	141	7
122.0	3.8	142	7
$D_T = 10.0$ cm			
107.9	0.7	5	2
109.6	0.8	12	2
112.4	1.1	32	2
114.7	1.5	52	3
116.3	1.9	68	4
116.7	2.1	78	4
117.6	2.5	90	5
118.6	2.9	109	6
119.6	3.3	123	7
120.3	3.6	133	7
120.7	3.8	143	8
121.1	4.0	149	8
121.4	4.1	152	8
$D_T = 20.0$ cm			
107.4	0.7	3	2
110.0	0.8	16	2
112.8	1.2	36	2
114.5	1.5	52	3
116.0	1.8	65	4
116.9	2.2	79	4
118.2	2.7	99	5
119.0	3.1	115	6
120.1	3.5	133	7
120.4	3.8	141	7
120.9	3.9	147	8
121.5	4.1	152	8

Table C.24: Surface temperatures T_s and corresponding heat fluxes q for the 2.0-cm-diameter structured disc of contact angle $\theta = 62^\circ$ surrounded by vessels of different diameters D_T

T_s (°C)	δT_s (°C)	q (W/cm^2)	δq (W/cm^2)
D_T = 2.0 cm			
106.1	0.7	5	2
108.0	0.7	12	2
109.8	0.8	20	2
111.0	1.0	30	2
112.2	1.3	42	3
112.8	1.5	49	3
113.5	1.7	61	4
114.0	2.0	73	4
114.6	2.3	84	5
115.0	2.4	90	5
D_T = 4.0 cm			
107.2	0.7	7	2
108.6	0.8	14	2
109.8	0.9	23	2
111.3	1.1	33	2
112.4	1.3	45	3
113.5	1.6	58	3
114.4	2.0	71	4
114.7	2.2	81	4
115.1	2.4	88	5
115.4	2.5	90	5
D_T = 10.0 cm			
107.6	0.7	8	2
109.8	0.8	20	2
111.4	1.1	31	2
112.4	1.3	43	3
113.2	1.6	56	3
114.2	1.9	69	4
114.7	2.1	78	4
115.3	2.4	90	5
115.6	2.4	89	5
D_T = 20.0 cm			
106.0	0.7	5	2
107.7	0.7	13	2
109.2	0.9	20	2
110.7	1.1	31	2
112.0	1.3	45	3
112.6	1.5	53	3
113.4	1.9	66	4
114.5	2.2	81	4
114.8	2.4	90	5
115.1	2.5	93	5

REFERENCES

[1] R. Chen, M. Lu, V. Srinivasan, Z. Wang, H.H. Cho, and A. Majumdar. Nanowires for enhanced boiling heat transfer. *Nano Letters*, 9(2):548–553, 2009.

[2] S.M. Kwark, G. Moreno, R. Kumar, H. Moon, and S.M. You. Nanocoating characterization in pool boiling heat transfer of pure water. *International Journal of Heat and Mass Transfer*, 53(21-22):4579–4587, 2010.

[3] M. Lu, R. Chen, V. Srinivasan, V.P. Carey, and A. Majumdar. Critical heat flux of pool boiling on Si nanowire array-coated surfaces. *International Journal of Heat and Mass Transfer*, 54(25-26):5359–5367, 2011.

[4] R. Wen, Q. Li, W. Wang, B. Latour, C.H. Li, C. Li, Y. Lee, and R. Yang. Enhanced bubble nucleation and liquid rewetting for highly efficient boiling heat transfer on two-level hierarchical surfaces with patterned copper nanowire arrays. *Nano Energy*, 38:59–65, 2017.

[5] K. Ahmed and K. Schuegraf. Transistor wars. *IEEE Spectrum*, 48(11):50–66, 2011.

[6] R. Courtland. Transistors could stop shrinking in 2021. *IEEE Spectrum*, 53(9):9–11, 2016.

[7] Y. Li and D. Goyal. *3D microelectronic packaging: from fundamentals to applications*, volume 57. Springer, 2017.

[8] T.G. Karayiannis and M.M. Mahmoud. Flow boiling in microchannels: fundamentals and applications. *Applied Thermal Engineering*, 115:1372–1397, 2017.

[9] A. Shakouri and Y. Zhang. On-chip solid-state cooling for integrated circuits using thin-film microrefrigerators. *IEEE Transactions on Components and Packaging Technologies*, 28(1):65–69, 2005.

[10] A. Bar-Cohen and P. Wang. Thermal management of on-chip hot spot. *Journal of Heat Transfer*, 134(5):051017, 2012.

[11] P. Wang, P. McCluskey, and A. Bar-Cohen. Two-phase liquid cooling for thermal management of IGBT power electronic module. *Journal of Electronic Packaging*, 135(2):021001, 2013.

[12] Y. Oka. *Nuclear reactor design*. Springer, 2014.

[13] K.A. Estes and I. Mudawar. Comparison of two-phase electronic cooling using free jets and sprays. *Journal of Electronic Packaging*, 117(4):323–332, 1995.

[14] S.G. Kandlikar and A.V. Bapat. Evaluation of jet impingement, spray and microchannel chip cooling options for high heat flux removal. *Heat Transfer Engineering*, 28(11):911–923, 2007.

[15] I. Mudawar. Recent advances in high-flux, two-phase thermal management. *Journal of Thermal Science and Engineering Applications*, 5(2):021012, 2013.

[16] W. Cheng, W. Zhang, H. Chen, and L. Hu. Spray cooling and flash evaporation cooling: the current development and application. *Renewable and Sustainable Energy Reviews*, 55:614–628, 2016.

[17] W. Qu and I. Mudawar. Flow boiling heat transfer in two-phase microchannel heat sinks—I. Experimental investigation and assessment of correlation methods. *International Journal of Heat and Mass Transfer*, 46(15):2755–2771, 2003.

[18] W. Qu and I. Mudawar. Flow boiling heat transfer in two-phase microchannel heat sinks—II. Annular two-phase flow model. *International Journal of Heat and Mass Transfer*, 46(15):2773–2784, 2003.

[19] A. Pavlova and M. Amitay. Electronic cooling using synthetic jet impingement. *Journal of Heat Transfer*, 128(9):897–907, 2006.

[20] M. Visaria and I. Mudawar. Theoretical and experimental study of the effects of spray inclination on two-phase spray cooling and critical heat flux. *International Journal of Heat and Mass Transfer*, 51(9-10):2398–2410, 2008.

[21] S.G. Kandlikar, M. Shoji, and V.K. Dhir. *Handbook of phase change: boiling and condensation*. Taylor & Francis Group, 1999.

[22] S. Nukiyama. The maximum and minimum values of the heat Q transmitted from metal to boiling water under atmospheric pressure. *Journal of the JSME*, 37(206):367–374, 1934.

[23] T.B. Drew and A.C. Mueller. Boiling. *Transactions of the AIChE*, 33:449–454, 1937.

[24] T.L. Bergman, A.S. Lavine, F.P. Incropera, and D.P. DeWitt. *Fundamentals of heat and mass transfer*. John Wiley & Sons, 2011.

[25] V.P. Carey. *Liquid-vapor phase-change phenomena: an introduction to the thermophysics of vaporization and condensation processes in heat transfer equipment*. Taylor & Francis Group, 2008.

[26] F.A. Kulacki, S. Acharya, Y. Chudnovsky, R.M. Cotta, R. Devireddy, V.K. Dhir, M.P. Mengüç, J. Mostaghimi, and K. Vafai. *Handbook of thermal science and engineering*. Springer, 2017.

[27] S.G. Bankoff. Entrapment of gas in the spreading of a liquid over a rough surface. *AIChE Journal*, 4(1):24–26, 1958.

[28] C.A. Ward and T.W. Forest. On the relation between platelet adhesion and the roughness of a synthetic biomaterial. *Annals of Biomedical Engineering*, 4(2):184–207, 1976.

[29] C.H. Wang and V.K. Dhir. On the gas entrapment and nucleation site density during pool boiling of saturated water. *Journal of Heat Transfer*, 115(3):670–679, 1993.

[30] G. Barthau. Active nucleation site density and pool boiling heat transfer-an experimental study. *International journal of heat and mass transfer*, 35(2):271–278, 1992.

[31] P. Griffith and J.D. Wallis. The role of surface conditions in nucleate boiling. *Chemical Engineering Progress Symposium Series*, 56(30):49–63, 1960.

[32] Y.Y. Hsu. On the size range of active nucleation cavities on a heating surface. *Journal of Heat Transfer*, 84(3):207–213, 1962.

[33] K. Mizukami. Entrapment of vapor in reentrant cavities. *Letters in Heat and Mass Transfer*, 2(3):279–284, 1975.

[34] S. Nishio. Stability of preexisting vapor nucleus in uniform temperature field. *Transactions of the JSME, Series B*, 54(503):1802–1807, 1988.

[35] Y.Y. Hsu and R.W. Graham. *Transport processes in boiling and two-phase systems, including near-critical fluids*. Hemispheric Publishing, 1976.

[36] B.B. Mikic and W.M. Rohsenow. A new correlation of pool-boiling data including the effect of heating surface characteristics. *Journal of Heat Transfer*, 91(2):245–250, 1969.

[37] K. Bier, D. Gorenflo, M. Salem, and Y. Tanes. Pool boiling heat transfer and size of active nucleation centers for horizontal plates with different surface roughness. *Proceedings of the 6th International Heat Transfer Conference*, 1:151–156, 1978.

[38] K. Cornwell and R.D. Brown. Boiling surface topography. *Proceedings of the 6th International Heat Transfer Conference*, 1:157–161, 1978.

[39] G. Kocamustafaogullari and M. Ishii. Interfacial area and nucleation site density in boiling systems. *International Journal of Heat and Mass Transfer*, 26(9):1377–1387, 1983.

[40] S.R. Yang and R.H. Kim. A mathematical model of the pool boiling nucleation site density in terms of the surface characteristics. *International Journal of Heat and Mass Transfer*, 31(6):1127–1135, 1988.

[41] C.H. Wang and V.K. Dhir. Effect of surface wettability on active nucleation site density during pool boiling of water on a vertical surface. *Journal of Heat Transfer*, 115(3):659–669, 1993.

[42] R.F. Gaertner. Distribution of active sites in the nucleate boiling of liquids. *Chemical Engineering Progress Symposium Series*, 59(41):52–61, 1963.

[43] M. Sultan and R.L. Judd. Spatial distribution of active sites and bubble flux density. *Journal of Heat Transfer*, 100(1):56–62, 1978.

[44] V.H. Del Valle and D.B.R. Kenning. Subcooled flow boiling at high heat flux. *International Journal of Heat and Mass Transfer*, 28(10):1907–1920, 1985.

[45] N. Basu, G.R. Warrier, and V.K. Dhir. Onset of nucleate boiling and active nucleation site density during subcooled flow boiling. *Journal of Heat Transfer*, 124(4):717–728, 2002.

[46] C. Han and P. Griffith. The mechanism of heat transfer in nucleate pool boiling—Part I: bubble initiation, growth and departure. *International Journal of Heat and Mass Transfer*, 8(6):887–904, 1965.

[47] C. Han and P. Griffith. The mechanism of heat transfer in nucleate pool boiling—Part II: the heat flux-temperature difference relation. *International Journal of Heat and Mass Transfer*, 8(6):905–914, 1965.

[48] B.B. Mikic, W.M. Rohsenow, and P. Griffith. On bubble growth rates. *International Journal of Heat and Mass Transfer*, 13(4):657–666, 1970.

[49] M.S. Plesset and A. Prosperetti. Bubble dynamics and cavitation. *Annual Review of Fluid Mechanics*, 9(1):145–185, 1977.

[50] R.L. Judd. The role of bubble waiting time in steady nucleate boiling. *Journal of Heat Transfer*, 121(4):852–855, 1999.

[51] W. Fritz. Maximum volume of vapor bubbles. *Physikalische Zeitschrift*, 36:379–384, 1935.

[52] M.S. Plesset and S.A. Zwick. The growth of vapor bubbles in superheated liquids. *Journal of Applied Physics*, 25(4):493–500, 1954.

[53] S.A. Zwick and M.S. Plesset. On the dynamics of small vapor bubbles in liquids. *Journal of Mathematics and Physics*, 33(4):308–330, 1955.

[54] R. Siegel and E.G. Keshock. Effects of reduced gravity on nucleate boiling bubble dynamics in saturated water. *AIChE Journal*, 10(4):509–517, 1964.

[55] T. Young. An essay on the cohesion of fluids. *Philosophical Transactions of the Royal Society*, (95):65–87, 1805.

[56] H.B. Eral, D.J.C.M. 't Mannetje, and J.M. Oh. Contact angle hysteresis: a review of fundamentals and applications. *Colloid and Polymer Science*, 291(2):247–260, 2013.

[57] E. Pierce, F.J. Carmona, and A. Amirfazli. Understanding of sliding and contact angle results in tilted plate experiments. *Colloids and Surfaces A: Physicochemical and Engineering Aspects*, 323(1-3):73–82, 2008.

[58] L. Gao and T.J. McCarthy. Contact angle hysteresis explained. *Langmuir*, 22(14):6234–6237, 2006.

[59] R.N. Wenzel. Resistance of solid surfaces to wetting by water. *Industrial & Engineering Chemistry*, 28(8):988–994, 1936.

[60] A.B.D. Cassie and S. Baxter. Wettability of porous surfaces. *Transactions of the Faraday Society*, 40:546–551, 1944.

[61] C. Ishino and K. Okumura. Wetting transitions on textured hydrophilic surfaces. *The European Physical Journal E*, 25(4):415–424, 2008.

[62] D. Murakami, H. Jinnai, and A. Takahara. Wetting transition from the Cassie-Baxter state to the Wenzel state on textured polymer surfaces. *Langmuir*, 30(8):2061–2067, 2014.

[63] Q.S. Zheng, Y. Yu, and Z.H. Zhao. Effects of hydraulic pressure on the stability and transition of wetting modes of superhydrophobic surfaces. *Langmuir*, 21(26):12207–12212, 2005.

[64] T.N. Krupenkin, J.A. Taylor, E.N. Wang, P. Kolodner, M. Hodes, and T.R. Salamon. Reversible wetting—dewetting transitions on electrically tunable superhydrophobic nanostructured surfaces. *Langmuir*, 23(18):9128–9133, 2007.

[65] G. Liu, L. Fu, A.V. Rode, and V.S.J. Craig. Water droplet motion control on superhydrophobic surfaces: exploiting the Wenzel-to-Cassie transition. *Langmuir*, 27(6):2595–2600, 2011.

[66] T.P. Allred, J.A. Weibel, and S.V. Garimella. Enabling highly effective boiling from superhydrophobic surfaces. *Physical Review Letters*, 120(17):174501, 2018.

[67] N. Ramanujapu and V.K. Dhir. Dynamics of contact angle during growth and detachment of a vapor bubble at a single nucleation site. *Proceedings of the 5th ASME/JSME Thermal Engineering Joint Conference*, 1999.

[68] G. Son, V.K. Dhir, and N. Ramanujapu. Dynamics and heat transfer associated with a single bubble during nucleate boiling on a horizontal surface. *Journal of Heat Transfer*, 121(3):623–631, 1999.

[69] S.P. Liaw. *Experimental and analytical study of nucleate and transition boiling on vertical surfaces*. PhD thesis, University of California, Los Angeles, 1988.

[70] K.T. Hong, H. Imadojemu, and R.L. Webb. Effects of oxidation and surface roughness on contact angle. *Experimental Thermal and Fluid Science*, 8(4):279–285, 1994.

[71] N. Basu. *Modeling and experiments for wall heat flux partitioning during subcooled flow boiling of water at low pressures*. PhD thesis, University of California, Los Angeles, 2003.

[72] Y. Nam and Y.S. Ju. Comparative study of copper oxidation schemes and their effects on surface wettability. *International Mechanical Engineering Congress and Exposition*, 48715:1833–1838, 2008.

[73] R.F. Tylecote. The composition and reduction of oxide films on copper. *Metallurgia*, 53(319):191–197, 1956.

[74] K.R. Lawless and A.T. Gwathmey. The structure of oxide films on different faces of a single crystal of copper. *Acta Metallurgica*, 4(2):153–163, 1956.

[75] Y. Maimaiti, M. Nolan, and S.D. Elliott. Reduction mechanisms of the CuO (111) surface through surface oxygen vacancy formation and hydrogen adsorption. *Physical Chemistry Chemical Physics*, 16(7):3036–3046, 2014.

[76] A. Takemura, K. Yuki, and A. Sadayuki. Influence of warm oxide layer on wettability and contact angle for heat transport devices. *Journal of Mechanics Engineering and Automation*, 7(2):341–347, 2017.

[77] S.K. Roy Chowdhury and R.H.S. Winterton. Surface effects in pool boiling. *International Journal of Heat and Mass Transfer*, 28(10):1881–1889, 1985.

[78] M. Maracy and R.H.S. Winterton. Hysteresis and contact angle effects in transition pool boiling of water. *International Journal of Heat and Mass Transfer*, 31(7):1443–1449, 1988.

[79] T.G. Theofanous, J.P. Tu, A.T. Dinh, and T.N. Dinh. The boiling crisis phenomenon: Part I: nucleation and nucleate boiling heat transfer. *Experimental Thermal and Fluid Science*, 26(6-7):775–792, 2002.

[80] W.M. Rohsenow. A method of correlating heat transfer data for surface boiling of liquids. *Transactions of the ASME*, 74:969–976, 1952.

[81] N. Bakhru and J.H. Lienhard. Boiling from small cylinders. *International Journal of Heat and Mass Transfer*, 15(11):2011–2025, 1972.

[82] R. Raj and J. Kim. Heater size and gravity based pool boiling regime map: transition criteria between buoyancy and surface tension dominated boiling. *Journal of Heat Transfer*, 132(9):091503, 2010.

[83] B.E. Staniszewski. *Nucleate boiling bubble growth and departure*. Massachusetts Institute of Technology, 1959.

[84] R.I. Eddington and D.B.R. Kenning. The effect of contact angle on bubble nucleation. *International Journal of Heat and Mass Transfer*, 22(8):1231–1236, 1979.

[85] H.T. Phan, N. Caney, P. Marty, S. Colasson, and J. Gavillet. How does surface wettability influence nucleate boiling? *Comptes Rendus Mécanique*, 337(5):251–259, 2009.

[86] E. Baker. Liquid immersion cooling of small electronic devices. *Microelectronics Reliability*, 12(2):163–173, 1973.

[87] K.A. Park and A.E. Bergles. Effects of size of simulated microelectronic chips on boiling and critical heat flux. *Journal of Heat Transfer*, 110(3):728–734, 1988.

[88] C.D. Henry and J. Kim. A study of the effects of heater size, subcooling, and gravity level on pool boiling heat transfer. *International Journal of Heat and Fluid Flow*, 25(2):262–273, 2004.

[89] W.B. Harrison and Z. Levine. Wetting effects on boiling heat transfer: the copper-stearic acid system. *AIChE Journal*, 4(4):409–412, 1958.

[90] S.P. Liaw and V.K. Dhir. Void fraction measurements during saturated pool boiling of water on partially wetted vertical surfaces. *Journal of Heat Transfer*, 111(3):731–738, 1989.

[91] A.R. Girard, J. Kim, and S.M. You. Pool boiling heat transfer of water on hydrophilic surfaces with different wettability. *International Mechanical Engineering Congress and Exposition*, 50626:V008T10A018, 2016.

[92] R.L. Judd and K.S. Hwang. A comprehensive model for nucleate pool boiling heat transfer including microlayer evaporation. *Journal of Heat Transfer*, 98(4):623–629, 1976.

[93] V.K. Dhir and S.P. Liaw. Framework for a unified model for nucleate and transition pool boiling. *Journal of Heat Transfer*, 111(3):739–746, 1989.

[94] C.P. Costello, C.O. Bock, and C.C. Nichols. A study of induced convective effects on pool boiling burnout. *Chemical Engineering Progress Symposium Series*, 61(7):271–280, 1965.

[95] J.H. Lienhard and K.B. Keeling Jr. An induced-convection effect upon the peak-boiling heat flux. *Journal of Heat Transfer*, 92(1):1–5, 1970.

[96] Y. Elkassabgi and J.H. Lienhard. Sidewall and immersion-depth effects on pool boiling burnout for horizontal cylindrical heaters. *Journal of Heat Transfer*, 109(4):1055–1057, 1987.

[97] T.S. Bockwoldt, S.M. Jeter, S.I. Abdel-Khalik, and J.G. Hartley. Induced convective enhancement of the critical heat flux from partially heated horizontal flat plates in saturated pool boiling. *Journal of Heat Transfer*, 114(2):518–521, 1992.

[98] S.M. Kwark, M. Amaya, R. Kumar, G. Moreno, and S.M. You. Effects of pressure, orientation, and heater size on pool boiling of water with nanocoated heaters. *International Journal of Heat and Mass Transfer*, 53(23-24):5199–5208, 2010.

[99] N Zuber. On the stability of boiling heat transfer. *Transactions of the ASME*, 80(3):711–720, 1958.

[100] N. Zuber. *Hydrodynamic aspects of boiling heat transfer*. PhD thesis, University of California, Los Angeles, 1959.

[101] S.S. Kutateladze. On the transition to film boiling under natural convection. *Kotloturbostroenie*, 3:10–12, 1948.

[102] G.I. Taylor. The instability of liquid surfaces when accelerated in a direction perpendicular to their planes. I. *Proceedings of the Royal Society. Series A. Mathematical, Physical and Engineering Sciences*, 201(1065):192–196, 1950.

[103] S.S. Kutateladze. A hydrodynamic theory of changes in a boiling process under free convection. *Izvestia Akademia Nauk Otdelenie Tekhnicheski Nauk*, 4:529–536, 1951.

[104] J.H. Lienhard and V.K. Dhir. Hydrodynamic prediction of peak pool-boiling heat fluxes from finite bodies. *Journal of Heat Transfer*, 95(2):152–158, 1973.

[105] J.H. Lienhard and V.K. Dhir. *Extended hydrodynamic theory of the peak and minimum pool boiling heat fluxes*. National Aeronautics and Space Administration, 1973.

[106] J.H. Lienhard, V.K. Dhir, and D.M. Riherd. Peak pool boiling heat-flux measurements on finite horizontal flat plates. *Journal of Heat Transfer*, 95(4):477–482, 1973.

[107] I.I. Gogonin and S.S. Kutateladze. Critical heat flux as a function of heater size for a liquid boiling in a large enclosure. *Journal of Engineering Physics*, 33(5):1286–1289, 1977.

[108] J.R. Saylor. An experimental study of the size effect in pool boiling CHF on square surfaces. Master's thesis, University of Minnesota, Twin Cities, 1989.

[109] K.N. Rainey and S.M. You. Effects of heater size and orientation on pool boiling heat transfer from microporous coated surfaces. *International Journal of Heat and Mass Transfer*, 44(14):2589–2599, 2001.

[110] P.J. Berenson. *On transition boiling heat transfer from a horizontal surface*. PhD thesis, Massachusetts Institute of Technology, 1960.

[111] P.J. Berenson. Experiments on pool-boiling heat transfer. *International Journal of Heat and Mass Transfer*, 5(10):985–999, 1962.

[112] S.P. Liaw and V.K. Dhir. Effect of surface wettability on transition boiling heat transfer from a vertical surface. *Proceedings of the 8th International Heat Transfer Conference*, 4:2031–2036, 1986.

[113] S.G. Kandlikar. A theoretical model to predict pool boiling CHF incorporating effects of contact angle and orientation. *Journal of Heat transfer*, 123(6):1071–1079, 2001.

[114] H.S. Ahn, H.J. Jo, S.H. Kang, and M.H. Kim. Effect of liquid spreading due to nano/microstructures on the critical heat flux during pool boiling. *Applied Physics Letters*, 98(7):071908, 2011.

[115] H. O'Hanley, C. Coyle, J. Buongiorno, T. McKrell, L. Hu, M. Rubner, and R. Cohen. Separate effects of surface roughness, wettability, and porosity on the boiling critical heat flux. *Applied Physics Letters*, 103(2):024102, 2013.

[116] J.J. Wei and H. Honda. Effects of fin geometry on boiling heat transfer from silicon chips with micro-pin-fins immersed in FC-72. *International Journal of Heat and Mass Transfer*, 46(21):4059–4070, 2003.

[117] C.H. Li and G.P. Peterson. Experimental study of enhanced nucleate boiling heat transfer on uniform and modulated porous structures. *Frontiers in Heat and Mass Transfer*, 1(2):023007, 2010.

[118] B.S. Kim, H. Lee, S. Shin, G. Choi, and H.H. Cho. Interfacial wicking dynamics and its impact on critical heat flux of boiling heat transfer. *Applied Physics Letters*, 105(19):191601, 2014.

[119] M.M. Rahman, E. Ölçeroğlu, and M. McCarthy. Role of wickability on the critical heat flux of structured superhydrophilic surfaces. *Langmuir*, 30(37):11225–11234, 2014.

[120] D.E. Kim, D.I. Yu, D.W. Jerng, M.H. Kim, and H.S. Ahn. Review of boiling heat transfer enhancement on micro/nanostructured surfaces. *Experimental Thermal and Fluid Science*, 66:173–196, 2015.

[121] J.M. Ramilison and J.H. Lienhard. Transition boiling heat transfer and the film transition regime. *Journal of Heat Transfer*, 109(3):746–752, 1987.

[122] I. Rajab and R.H.S. Winterton. The two transition boiling curves and solid-liquid contact on a horizontal surface. *International Journal of Heat and Fluid Flow*, 11(2):149–153, 1990.

[123] F. Reguillot. Boiling on flat resistance heaters. Master's thesis, University of Houston, 1990.

[124] J.M. Ramilison, P. Sadasivan, and J.H. Lienhard. Surface factors influencing burnout on flat heaters. *Journal of Heat Transfer*, 114(1):287–290, 1992.

[125] J.Y. Chang and S.M. You. Boiling heat transfer phenomena from micro-porous and porous surfaces in saturated FC-72. *International Journal of Heat and Mass Transfer*, 40(18):4437–4447, 1997.

[126] J.Y. Chang and S.M. You. Enhanced boiling heat transfer from microporous surfaces: effects of a coating composition and method. *International Journal of Heat and Mass Transfer*, 40(18):4449–4460, 1997.

[127] S.K. Das, N. Putra, and W. Roetzel. Pool boiling characteristics of nano-fluids. *International Journal of Heat and Mass Transfer*, 46(5):851–862, 2003.

[128] S.M. You, J.H. Kim, and K.H. Kim. Effect of nanoparticles on critical heat flux of water in pool boiling heat transfer. *Applied Physics Letters*, 83(16):3374–3376, 2003.

[129] S.J. Kim, I.C. Bang, J. Buongiorno, and L.W. Hu. Surface wettability change during pool boiling of nanofluids and its effect on critical heat flux. *International Journal of Heat and Mass Transfer*, 50(19-20):4105–4116, 2007.

[130] H.S. Ahn, N. Sinha, M. Zhang, D. Banerjee, S. Fang, and R.H. Baughman. Pool boiling experiments on multiwalled carbon nanotube (MWCNT) forests. *Journal of Heat Transfer*, 128(12):1335–1342, 2006.

[131] S. Ujereh, T. Fisher, and I. Mudawar. Effects of carbon nanotube arrays on nucleate pool boiling. *International Journal of Heat and Mass Transfer*, 50(19-20):4023–4038, 2007.

[132] Y. Im, Y. Joshi, C. Dietz, and S.S. Lee. Enhanced boiling of a dielectric liquid on copper nanowire surfaces. *International Journal of Micro-Nano Scale Transport*, 1(1):79–96, 2010.

[133] Z. Yao, Y.W. Lu, and S.G. Kandlikar. Effects of nanowire height on pool boiling performance of water on silicon chips. *International Journal of Thermal Sciences*, 50(11):2084–2090, 2011.

[134] A.D. Messina and E.L. Park Jr. Effects of precise arrays of pits on nucleate boiling. *International Journal of Heat and Mass Transfer*, 24(1):141–145, 1981.

[135] T.M. Anderson and I. Mudawar. Microelectronic cooling by enhanced pool boiling of a dielectric fluorocarbon liquid. *Journal of Heat Transfer*, 111(3):752–759, 1989.

[136] I. Mudawar and T.M. Anderson. Optimization of enhanced surfaces for high flux chip cooling by pool boiling. *Journal of Electronic Packaging*, 115(1):89–100, 1993.

[137] K. Chu, Y.S. Joung, R. Enright, C.R. Buie, and E.N. Wang. Hierarchically structured surfaces for boiling critical heat flux enhancement. *Applied Physics Letters*, 102(15):151602, 2013.

[138] B. Bon, J. Klausner, and E. McKenna. An investigation of pool boiling heat transfer on single crystal surfaces and a dense array of cylindrical cavities. *Journal of Heat Transfer*, 135(12):121501, 2013.

[139] S. Das, B. Saha, and S. Bhaumik. Experimental study of nucleate pool boiling heat transfer of water by surface functionalization with crystalline TiO_2 nanostructure. *Applied Thermal Engineering*, 113:1345–1357, 2017.